LBL-37279
UC-1240

Lawrence Berkeley Laboratory
UNIVERSITY OF CALIFORNIA

EARTH SCIENCES DIVISION

Application of Seismic Tomographic Techniques in the Investigation of Geothermal Systems

A.E. Romero, Jr.
(Ph.D. Thesis)

May 1995

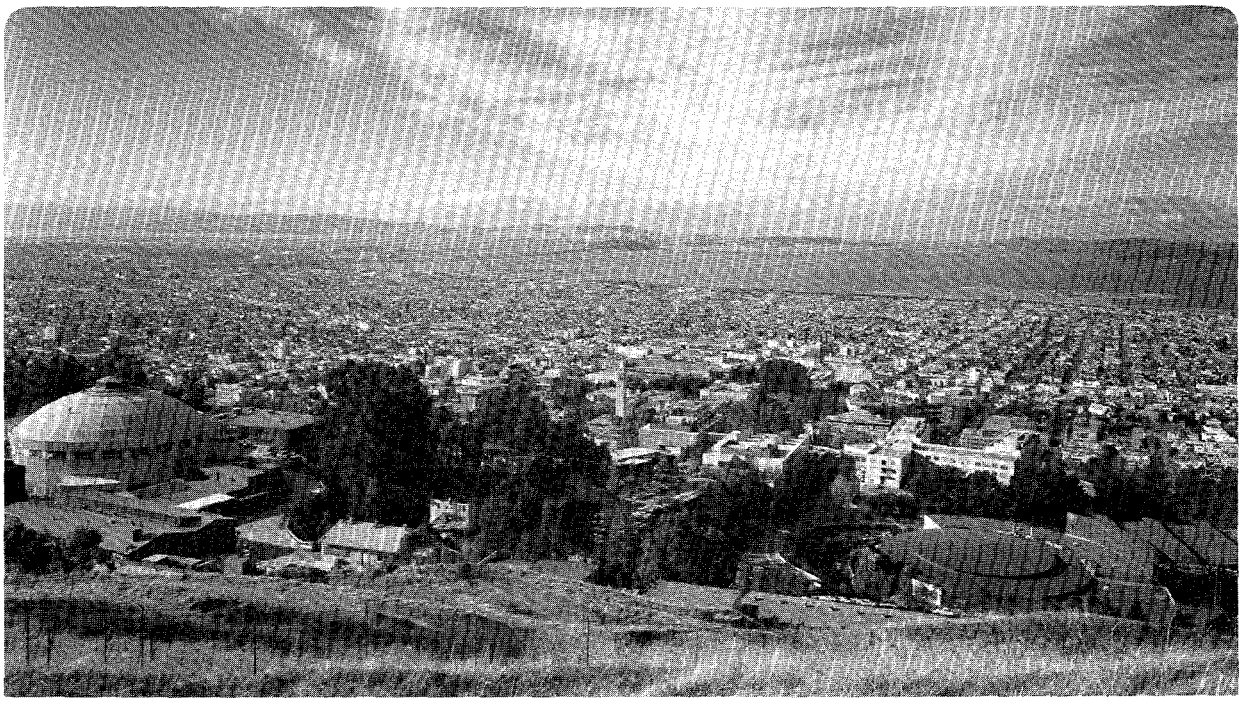

Prepared for the U.S. Department of Energy under Contract Number DE-AC03-76SF00098

LBL-37279
UC-1240

Application of Seismic Tomographic Techniques in the Investigation of Geothermal Systems

Arturo Espejo Romero, Jr.
Ph.D. Thesis

Department of Geology and Geophysics
University of California, Berkeley

and

Earth Sciences Division
Lawrence Berkeley Laboratory
University of California
Berkeley, CA 94720

May 1995

This work was supported by the Assistant Secretary for Energy Efficiency and Renewable Energy, Geothermal Division, of the U.S. Department of Energy under Contract No. DE-AC03-76SF00098.

Application of Seismic Tomographic Techniques in the Investigation of Geothermal Systems

by

Arturo Espejo Romero, Jr.

ABSTRACT

Application of Seismic Tomographic Techniques in the Investigation of Geothermal Systems

by

Arturo Espejo Romero, Jr.

Doctor of Philosophy in Geophysics

University of California at Berkeley

Professor Thomas V. McEvilly, Chair

The utility of microearthquake data for characterizing the Northwest Geysers geothermal field and the Long Valley Caldera (LVC) was investigated. Three-dimensional (3-D) P- and S-wave seismic velocity models were estimated for the Coldwater Creek Steam Field (CCSF) in the Northwest Geysers region. Hypocenters relocated using these 3-D models appear to be associated with the steam producing zone, with a deeper cluster of hypocenters beneath an active injection well. Spatial and temporal patterns of seismicity exhibit strong correlation with geothermal exploitation. A 3-D differential attenuation model was also developed for the CCSF from spectral ratios corrected for strong site effects. High-velocity anomalies and low attenuation in the near surface correspond to Franciscan metagraywacke and greenstone units. Microearthquakes recorded at seismographic stations located near the metagraywacke unit exhibit high corner frequencies. Low-velocity anomalies and higher attenuation in the near surface are associated with sections of Franciscan melange. Near-surface high attenuation and high Vp/Vs are interpreted to indicate liquid-saturated regions affected by meteoric recharge. High attenuation and low Vp/Vs marks the steam producing zone, suggesting undersaturation of the reservoir rocks. The extent of the high

attenuation and low Vp/Vs anomalies suggest that the CCSF steam reservoir may extend northwestward beyond the known producing zone.

A high-resolution tomographic study was conducted at LVC to develop 3-D P- and S-wave seismic velocity models. The experiment targeted the inferred magma chamber beneath the Resurgent Dome. The resulting velocity structure defines the low-velocity caldera fill, in contrast to the surrounding higher-velocity Sierran block and highland terrane. The Vp/Vs structure contains significant variation within and beneath the caldera, and can be related to accepted models of the active geothermal system. Low values of the Vp/Vs ratio beneath LVC argue against the presence of a distinct magma body at midcrustal depth.

This study concludes that microearthquake monitoring may be useful as an active reservoir management tool. Seismic velocity and attenuation structures as well as the distribution of microearthquake activity can be used to identify and delineate the geothermal reservoir, while temporal variations in these quantities would be useful in tracking changes during exploitation.

Para sa aking minamahal na lola, Feliza

(Dedicated to my beloved

grandmother, Feliza)

TABLE OF CONTENTS

LIST OF FIGURES

LIST OF TABLES

ACKNOWLEDGMENTS

Prof. Tom McEvilly was my advisor throughout my graduate career. I am indebted to him for his support and insight and for giving me the opportunity to go to Berkeley. Prof. Lane Johnson has always been there to answer my questions. He has given me direction at a time when I was drifting aimlessly. I am grateful to Dr. Ernie Majer for finding funding for me even in the face of major cutbacks. I owe a great deal of gratitude to Mark Walters, Marcelo Lippmann, and Emilio Antúnez for their invaluable assistance on the geothermal aspect of the study and to Dr. Norm Goldstein for injecting some sense of humor in our discussions. I thank Prof. Neville Cook for showing me the rudiments of rock mechanics. This study would not have been possible without the generosity of Dr. Alberto Michelini for sharing his programs with me. My deepest appreciation goes to John Peterson, Tom Daley and Don Vasco for their help in acquiring and processing the data. Many thanks to Drs. Dave Hill and Bill Peppin for assisting and sharing the Long Valley USGS and UNR data and to CCPA No. 1 for allowing access to the NW Geysers data.

I enjoyed stimulating discussions on MEQ clusters, model resolution and other seemingly important topics with my fellow graduate students Bob Nadeau and Roland Gritto. Bob has provided entertainment with his funny antics and juicy tidbits about departmental gossips. Roland, Paul Parker, Ken Williams, Bruno Kaelin, Patty Seifert and Ann Kirkpatrick shared with me the pitfalls of wind surfing and wild white-water rafting. Thanks guys for enriching my California experience.

I am grateful to my uncle Tony Espejo for being my closest family when I was so far from home. My father inculcated in me the importance of knowledge. I thank him for giving me the motivation to succeed. I am forever indebted to my mother for her unconditional love and guidance. To my wife, Gina, who was always there when I needed someone, thank you for your support and understanding and for keeping up with

my unusual schedule. Lastly, my beloved grandmother Feliza, who did not live long enough to see the fruition of my life-long dream, helped me grow up to be the person I am today. No person more compassionate has ever lived.

This study was supported by the Assistant Secretary for Energy Efficiency and Renewable Energy, Geothermal Division, of the U.S. Department of Energy under contract DE-AC03-76SF00098. Computation and field operations used the LBL Center for Computational Seismology and the Geophysical Measurement Facility, respectively, both supported by DOE Office of Basic Sciences, Engineering and Geosciences Division.

Chapter 1

INTRODUCTION AND OVERVIEW

Elastic P and S-waves are the most effective radiation with which to illuminate the heterogeneous subsurface in seeking to develop an image of the distribution of rock properties. Compared to other geophysical techniques such as gravity and electromagnetic methods, the seismic method utilizes these waves to provide a more detailed and better resolved picture of the subsurface geology. Earthquake seismology has been carried out since the early 20th century when seismological observatories scattered around the world began using the travel times of recorded earthquakes to derive information on the internal structure of the earth. On a smaller scale, but in much the same way, seismic reflection surveying provides a picture of the subsurface structure from the near surface to a depth of several kilometers. It uses artificial seismic sources, such as explosions and vibrator trucks, whose characteristics such as timing, location and duration are directly controllable, in contrast to earthquake sources. Active seismic surveys are very useful in characterizing simple subsurface geometries and find wide applications in the exploration of oil and gas which are usually situated in fairly uniform sedimentary layers. A variant of this method, the refraction survey, is well-suited for near surface sediment mapping such as those for finding the water table or the depth to bedrock in engineering foundation studies.

Despite its wide applicability, the active seismic reflection method has not easily yielded acceptable results in applications to complex geological structures not characterized by relatively coherent sedimentary sections. As an example, the DOE deep exploratory well at Long Valley Caldera, a geologically complex volcanic environment, provided a good opportunity to apply the VSP method to understand the shallow properties and to give high-resolution imaging than is possible with surface recordings.

The VSP study, however, yielded ambiguous results probably because of complications arising from anisotropy and scattering which perturb wave field coherency (Romero et al, 1995). Strong velocity gradients and laterally-varying structures disperse seismic waves in all directions, complicating the separation of the down-going and up going wave fields. The study failed to find reflections from below the current bottom of the drill hole in search of the supposed magma body located at mid-crustal depths.

An alternative method for imaging the subsurface that has gained a lot of attention in recent years is natural-event seismic tomography. The rapid development in tomographic inversion techniques over the last decade have made it practicable to image complex geological structures in well-instrumented areas such as The Geysers, Long Valley, and Parkfield yielding seismic velocity models with resolutions of a few kilometers. The theory is based on the minimization of the residuals to obtain hypocenters, and three-dimensional velocity and attenuation structures. Initial development of the simultaneous inversion techniques for seismic applications is attributed to Crosson (1976) and Aki and Lee (1976). Subsequent applications acquired more sophisticated model parametrization , a choice often dictated by the type and speed of the ray-tracing technique adopted for the forward problem, and by the specific geometry imposed by station distribution and the geologic setting of the area under investigation. For example, Crosson (1976) used homogeneous constant velocity layers. Aki and Lee (1976) parametrized their model by subdividing the volume into constant velocity cells. Spencer and Gubbins (1980) applied the technique to subduction-zone earthquakes by adopting an analytic velocity function with coefficients to be determined in the inversion. Pavlis and Booker (1980) solved for a vertical, one-dimensional velocity model following the formalism of Backus and Gilbert (1967) by approaching the problem as under-determined. They introduced the parameter-separation technique to reduce the joint problem to a tractable size and proposed the progressive inversion scheme developed by Roecker (1982). O'Connell (1991)

extended the Pavlis-Booker method to the joint inversion for P- and S-velocity structures and station corrections. Thurber (1983) also adopted this progressive inversion scheme, using a three-dimensional ray-tracer on a model parametrized in terms of linear interpolating functions. This method specifies velocities at a discrete number of node points in a 3-D rectangular mesh. Because of its relative simplicity and practicability, this inversion scheme has found a wide variety of applications such as in geothermal regions (Julian et al., 1993; O'Connell and Johnson, 1991; Eberhart-Phillips, 1986),in fault zones (Foxall et al. (1992), Michelini and McEvilly (1991), and in volcanic regions (Toomey and Foulger, 1989). O'Connell and Johnson (1991) incorporated S-waves in the progressive inversion scheme, making it possible to estimate the Vp/Vs structure, an important parameter in determining the mechanical properties of rocks and fluids at depth. Michelini and McEvilly, (1991) modified the interpolation scheme of the Thurber method using of cubic spline basis functions and later employed this procedure to construct relatively smooth models of the San Andreas Fault zone around the vicinity of Parkfield, Calif. As part of this study, this procedure has been extended to obtain differential attenuation structure because of the close analog between travel times and the differential attenuation operator t*. The seismic velocity and attenuation structure provide independent and complimentary information on the mechanical properties of rocks and fluids at depth.

This study is part of the continuing work being undertaken by Lawrence Berkeley laboratory (LBL), in cooperation with industry partners at The Geysers geothermal field, California, during the last several years to evaluate microearthquake data to study the origin and significance of geothermal seismicity. Seismicity at The Geysers is a well-known occurrence. Several previous studies have concluded that seismicity in The Geysers is related to geothermal development (e.g. Hamilton and Muffler, 1972; Majer and McEvilly, 1979; Ludwin and Bufe, 1980; Eberhart-Phillips and Oppenheimer, 1984; Stark, 1990; and Romero et al., 1994). Currently, The

Geysers supplies about 8% of PG&E's Northern California power production. Since 1984, the steam pressure has been declining in an increasing rate (Barker et al 1992). It was hoped that microearthquake research could help shed some light in understanding the physical processes that is causing this trend. The purpose of this study is to use the microearthquakes as energy sources for imaging the in situ physical properties within the reservoir area. It applies the Thurber (1983) progressive inversion method, as modified by Michelini and McEvilly (1991), to develop 3-D velocity model of the geothermal reservoir beneath the Northwest Geysers. The resulting P- and S-wave models can be used to construct a three-dimensional Vp/Vs distribution that may provide some information on the degree of fluid saturation of the reservoir rocks. In addition, microearthquakes can be relocated more precisely using the three-dimensional velocity models. Evidence for induced seismicity is investigated by analyzing the patterns of seismicity in relation to geothermal activities. The spatial and temporal variations of seismicity and the velocity and attenuation structures are useful in understanding the dynamics of the geothermal reservoir.

This study develops a progressive inversion method to model the 3-D differential attenuation structure beneath the Northwest Geysers geothermal field. The differential attenuation structure is obtained from the P- and S-wave amplitude spectral ratios. The spectral ratios were constructed by dividing each spectrum with a reference spectrum from each observing station. The reference spectrum was derived from the average spectrum of all events that were recorded in that station. This was done to correct for the strong site-dependence of the observed spectra. The differential attenuation operator t* was then estimated from the slopes of the spectral ratios. The velocity models and the ray paths for all events are known from the previous velocity inversion. The inversion for the differential attenuation structure was carried out using a modification of the progressive inversion scheme of Thurber (1983).

The study exploits the high quality data from high-resolution networks located at

the Coldwater Creek Steam Field (CCSF) at the Northwest Geysers. The CCSF array is unique in its capability because of a dense station coverage (16 stations covering a 125 km^2 area), high-frequency digital sampling (400 samples/second/channel), and the borehole emplacement of geophones. LBL has been working with the Central California Power Agency No. 1 in the recording and analysis of the microearthquake data set. Legal and technical complications forced the array to shut down in 1989. However, it was brought back into operation in October 1993.

Finally, this study has applied the modified progressive inversion procedure at the Long Valley Caldera, California to image the top 10 km of the caldera and search for a shallow magma chamber. A number of geophysical studies argue for the existence of a magma body at shallow to midcrustal depths beneath Long valley calera (LVC) (Sanders, 1984; reviews are presented by Hill et al., 1985a; Rundle et al., 1986; Goldstein, 1988; and Goldstein and Stein, 1988). Other studies have found no indications of anomalous regions beneath the caldera (Kissling, 1988; and Hauksson, 1988). In an attempt to resolve these conflicting results on the presence of a shallow magma chamber under LVC, a special high-resolution tomographic study was initiated. LBL installed a fan array of eight three-component borehole (80-160 m depths) receivers on the northwestern rim of the caldera to supplement the dense microearthquake network at Long Valley operated jointly by the U.S. Geological Survey (USGS) and the University of Nevada, Reno (UNR). The fan array provided added ray path coverage in and below the Resurgent Dome, in the region of the proposed magma chamber, from microearthquake sources in the southeast. While the main purpose of this study was to confirm or refute the presence of a shallow magma chamber, it also allowed the delineation of the geothermal reservoir beneath the western part of the caldera.

A clear understanding geothermal processes is important because it represents a vast resource and may well bridge the gap between the shift from fossil fuel to a cleaner, long-lasting energy source in the 21st century. This dissertation discusses the utility of

seismic tomographic techniques in the characterization of geothermal systems. Chapter two summarizes relationship between microearthquakes and geothermal systems and discusses the physical basis of the seismological parameters used in the delineation of the reservoir rocks, including the relationship between seismic velocity and attenuation and the mechanical state of rocks. Chapter two also presents a review of the mechanisms for induced seismicity in geothermal regions. Chapter three presents the results of the 3-D velocity inversion study conducted at the Northwest Geysers geothermal field. Chapter three also includes a study of the spatial and temporal occurrence of microearthquakes at the Northwest Geysers. The 3-D attenuation structure beneath the Northwest Geysers geothermal field is presented in chapter four. The Long Valley caldera velocity inversion study is discussed in chapter five. Finally, chapter six presents the overall conclusions regarding the applicability of seismic inversion techniques in geothermal investigations.

Chapter 2

PHYSICAL BASIS FOR THE APPLICATION OF SEISMIC TOMOGRAPHIC TECHNIQUES IN THE CHARACTERIZATION OF GEOTHERMAL SYSTEMS

2.1 Definition of a Geothermal System

A geothermal resource is any region in the earth that has relatively high heat content and sufficient porosity and permeability so that the working fluid (water or steam) is accessible enough that it can be harnessed profitably. The earth continually produces thermal energy at depth primarily through the decay of radioactive elements. This heat rises through the crust where it is lost through the surface. Although this thermal energy is enormous, the heat is generally too diffuse for economic recovery. Only in regions of high heat concentration, such as active or geologically-young igneous provinces, is there the possibility for commercial geothermal exploitation at shallow depths. To illustrate the degree of concentration of thermal energy in a geothermal region, the enthaply of saturated steam (at 236°C and 3.2 MPa), 2790 kJ/kg is a factor of 30 greater than the average heat content of crustal rocks in the upper 10 km, 85 kJ/kg (Rybach, 1981).

Figure 2.1 presents a conceptual model of a typical convective geothermal system adapted from Grant et al. (1982) and based on White (1967). The model depicts meteoric water percolating downward through bounding faults and fractures where it heated by close contact with hot rocks, usually associated with magmatic bodies, at depths of several kilometers. Buoyancy imbalance brought about by temperature differences then drives the hot fluid upwards where part of it is vented to the surface as geysers or hot springs while the rest is prevented by a low permeability cap rock and is

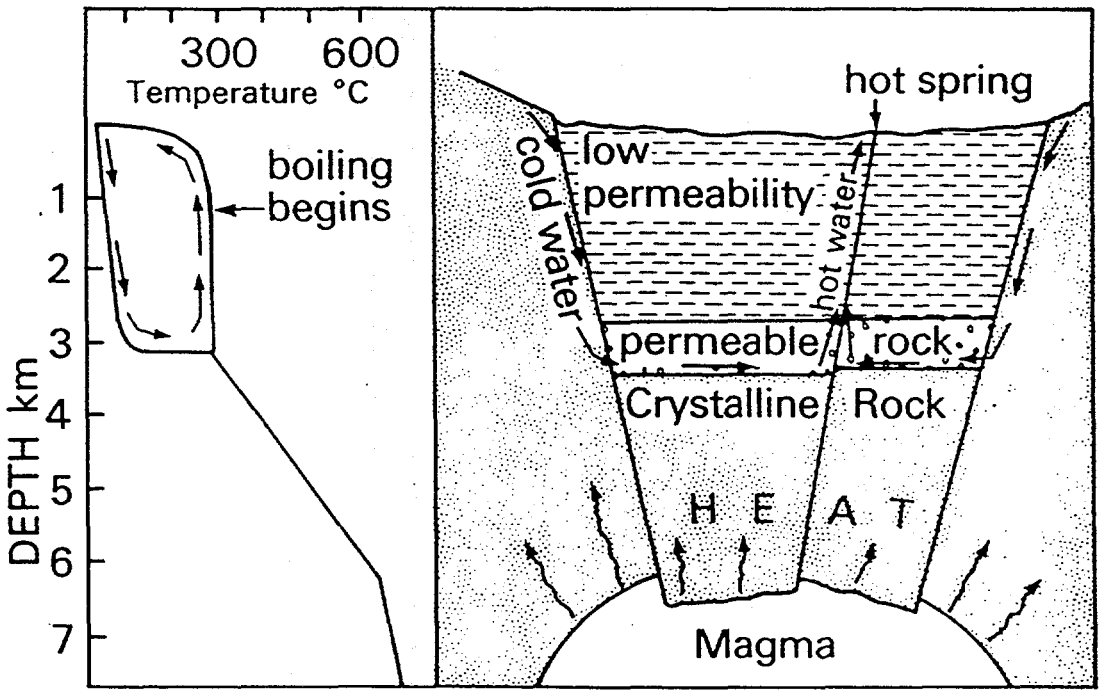

Figure 2.1 Conceptual model of a typical geothermal system adapted from Grant et al. (1982) based on White (1967). The model depicts meteoric water percolating downward through bounding faults where it heated by close contact with hot rocks at depths of several kilometers. Buoyancy imbalance drives the hot fluid upwards where part of it is vented to the surface while the rest is prevented by a low-permeability cap rock and is stored in high permeability reservoirs.

stored in high permeability reservoirs.

Geothermal potential depends highly on the degree of porosity and permeability of the host rocks. The reservoir must have high porosity for heat storage and sufficient permeability to access the working fluid for economic viability. The driving force that moves the working fluid is usually density difference between the up-going hot geothermal fluids and down-going colder recharge water. Hot water sometimes reaches the surface in some geothermal regions forming hot springs, fumaroles and geysers (The Geysers, northern California; Yellowstone National Park, Wyoming; Taupo geothermal field, New Zealand; and Tiwi geothermal field, Philippines) while in other areas, limited surface manifestation disguises geothermal reservoirs (e.g. Heber and East Mesa geothermal fields, southern California).

The depth of the geothermal reservoir is another critical parameter in determining the economic feasibility of the geothermal resource. Magma bodies, the heat source of geothermal systems, occur at any depth and can be extruded at the surface. Geothermal reservoirs can be found anywhere from the surface to several kilometers deep, depending on the local geothermal gradient and the vigor of circulating fluids. Exploitable geothermal resources must lie within commercially drillable depths, roughly 4 km or less with current drilling technology (Duffield et al., 1994). An ideal geothermal resource therefore must have high temperatures at shallow depths.

Geothermal reservoirs may be classified according to their hydrological and heat transfer characteristics (Rybach, 1981; Muffler, 1976):

1) Convective geothermal systems
    a) Hydrothermal systems in high porosity/permeability regions related to young, shallow silicic intrusion.
    b) Circulation systems in low porosity/permeability regions, in areas of normal to high regional heat flow.
2) Conductive geothermal systems

a) Low temperature aquifers in high porosity/permeability sedimentary sequences (including geopressured regions), in areas of normal to elevated heat flow.

b) Hot dry rock in high temperature/low permeability regions.

Convective geothermal systems are characterized by the natural circulation of the hydrothermal fluid which transfers heat mainly by convection. Because of the highly permeable host rocks, high temperature gradients exist at the boundary of the reservoir while the central parts are in near isothermal conditions. This system usually develops in plate margins and young tectonic provinces where the heat source is primarily active or young silicic magmatic intrusions located at the base of the reservoir. Springs, fumaroles or geysers are usually found at the surface. This type of system comprises a majority of the commercially developed geothermal fields in the world. Two types of convective geothermal systems are recognized: vapor-dominated systems such as The Geysers, California and Larderello, Italy; and liquid-dominated systems like Wairakei, New Zealand; Imperial Valley, California; and Tiwi, Philippines. Geophysical methods that could characterize convective systems include heat flow studies (temperature gradient wells usually indicate high geothermal gradients), gravity methods (lower densities brought about by higher porosities due to high water/steam fraction and by thermal expansion), electrical methods (presence of highly conductive geothermal fluids) and seismic methods (microearthquake monitoring, teleseismic residuals and tomography).

Circulation geothermal systems result from the deep circulation of meteoric water in regions of normal to high heat flow. Usually, the presence of faults or fracture zones provide the necessary fracture permeability to permit water circulation despite the low rock porosity/permeability. The eventual temperature of the water depends on the depth of circulation and the regional heat flow. This system also precludes the presence of nearby igneous activity and may develop in a wide range of geologic settings. Warm

springs are usually present near faults or fractures. This system is usually characterized by high heat flow, high electrical conductivity, shallow Curie temperature, low regional P-wave velocities, and high regional Bouger gravity anomaly indicating some anomalous processes that produce local high-density anomalies and occurring perhaps at the base of the crust (Diment, 1980).

Conductive geothermal systems are characterized by conductive heat flow. The working fluid can either be present, as in deep aquifers in sedimentary basins, or absent as in hot dry rocks. Convection is prohibited by low temperature gradients or low permeability. A special type of the conductive geothermal environment is the geopressured system where hot water is almost completely sealed from exchange with surrounding rocks. The trapped pore fluid is under pressure exceeding the normal hydrostatic pressure at that depth, accounting for a large fraction of the lithostatic pressure and supporting the overburden (Ryback, 1981). This system usually forms in basins where pore water expelled during diagenetic compaction cannot escape at a rate in balance with the accumulation of overlying sediments. Geopressured systems are sandwiched between relatively impermeable shale layers as in the northern Gulf of Mexico basin (Wallace et al., 1979) and also contain considerable amounts of methane. Thus, the exploitable thermal energy resource is roughly partitioned between the temperature of the water and the combustion energy of the dissolved methane (Duffield et al., 1994).

Hot dry rocks are high-temperature geothermal environments usually located in high heat flow regions with considerable thermal energy, accessible with current drilling technology, but having very little fluid to transfer the stored energy. These systems are also characterized by low permeability. Hot dry rocks represent the highest potential geothermal resources because of the presence of great regions with high heat flow and low permeability. Since working fluids are absent, heat must be harnessed by establishing artificial fluid circulation. Water is pumped down an injection well and after

being heated at depth is brought back to the surface through a production well. Research of this type has been conducted at Fenton Hill, New Mexico to develop the necessary technology for this type of artificial geothermal system. The state of regional stress is very important in hot dry rock applications. The orientation of the fractures formed by hydraulic fracturing, used to increase the permeability of rocks, is critically dependent on the stress regime at depth. Furthermore, the in situ stress level determines the injection pressure required to keep the fractures open and permit circulation. Knowledge of the stress field is essential to better understand the potential for induced earthquakes by the injection of water at depth and sufficiently increase the pore pressureto cause shear failure on pre-existing faults that are near failure. The next section discusses the relationship between microearthquakes and geothermal systems.

2.2 Mechanisms of Induced Seismicity in Geothermal Regions

Geothermal regions are characterized by high levels of seismic activity and previous studies indicate that seismicity is associated with exploitation-related activities, e.g. Larderello, Italy (Batini et al., 1985); Wairakei, New Zealand (Sherburn, 1984); and The Geysers, California (Hamilton and Muffler, 1972; Majer and McEvilly, 1979; Ludwin and Bufe, 1980; Eberhart-Phillips and Oppenheimer , 1984; Stark, 1990; Romero et al., 1994). Eberhart-Phillips and Oppenheimer (1984) showed that high seismicity at The Geysers was caused by steam production. On the other hand, Stark (1990), using Unocal proprietary and public microearthquake data, argued that seismicity correlates with injection activities. He showed striking temporal and spatial correlations between injection wells and deep seismicity nearby (deeper than 4000 ft). Romero et al (1994) also documented the close association between microearthquake occurrence and two injection wells at the Northwest Geysers area. One of the earliest

comprehensive microearthquake studies at The Geysers was done by Majer and McEvilly (1979). Using explosion and microearthquake sources they developed velocity and attenuation models of the geothermal reservoir and analyzed the source properties of "geothermal" earthquakes and offered possible inducing mechanisms.

Although the close association between geothermal activities and seismicity is well established, the mechanism of earthquake generation is still an area of controversy. Several possible mechanisms have been proposed. Among them:

A) Injection -related mechanisms:

1) Increase in pore pressure leading to decrease in effective normal stress (Healy et al., 1968; Hubbert and Ruby, 1959; Stark,1990).

2) Thermal contraction (Denlinger, 1980; Denlinger and Bufe, 1982).

B) Production-related mechanisms:

1) Volumetric contraction (McGarr, 1976; Majer and McEvilly, 1979; Eberhart-Phillips and Oppenheimer, 1984).

2) Collapse of overburden (Seagall, 1989).

3) Increase in shear stress due to fracture deflation (Denlinger and Bufe, 1982).

4) Thermal contraction (Denlinger 1980; Denlinger and Bufe, 1982).

5) Conversion of steady to stick-slip behavior due to a reduction in pore pressure or an increase in friction due to silica precipitation (near failure criterion) (Allis, 1982).

In order to understand the different types of seismicity-inducing mechanisms in geothermal regions, it is necessary to review the basic relationship between the stresses and failure on an existing fracture. Given the regional maximum (σ_1) and minimum (σ_3) principal stresses and the pore pressure P, the normal (σ) and shear (τ) stresses acting on a fracture with a given orientation are given by:

$$\sigma = \frac{(\sigma_1 + \sigma_3)}{2} - P + \frac{(\sigma_1 - \sigma_3)}{2}\cos 2\theta \qquad (1)$$

$$\tau = -\frac{(\sigma_1 - \sigma_3)}{2}\sin 2\theta \qquad (2)$$

where θ is the angle between the normal to the fracture and the σ_1 direction. By convention, positive σ denotes compression. Assuming that an earthquake results from shear failure, the necessary shear stress, τ, for this to occur is given by the Coulomb failure criterion:

$$\tau = S_o + \sigma\mu \qquad (3)$$

where S_o is the cohesional strength of the rock and μ is the friction coefficient of the fracture surface. The Mohr circle provides a graphical representation of equations (1) to (3). Figure 2.2 presents a typical tri-axial compressional configuration that is analogous to the stress field existing at depth. A necessary condition for shear failure is that the shear stress across the fracture (y-axis) exceeds the shear stress value of the Coulomb failure criterion, that is, the Mohr circle intersects the Coulomb failure line, as illustrated in Figure 2.2. There are several ways that this scenario could happen. An increase in pore pressure, P, brought about by the injection of fluids would shift the Mohr circle to the left, as defined in (1). If the fault or fracture is already close to failure, a small increment in pore pressure could decrease the effective normal stress enough to cause a shear failure (Hubbert and Ruby, 1959) . This mechanism can explain the occurrence of microearthquakes beneath injection wells at The Geysers. As pointed out by Stark (1990), the standing column of water within the injection wells could locally provide enough hydraulic head to cause seismic slip even in sub-hydrostatic reservoir pressure conditions. In another case, Majer and McEvilly (1979), following McGarr (1976), proposed that volumetric changes brought about by steam withdrawal could cause the observed seismicity at The Geysers. McGarr (1976) demonstrated that if the withdrawal

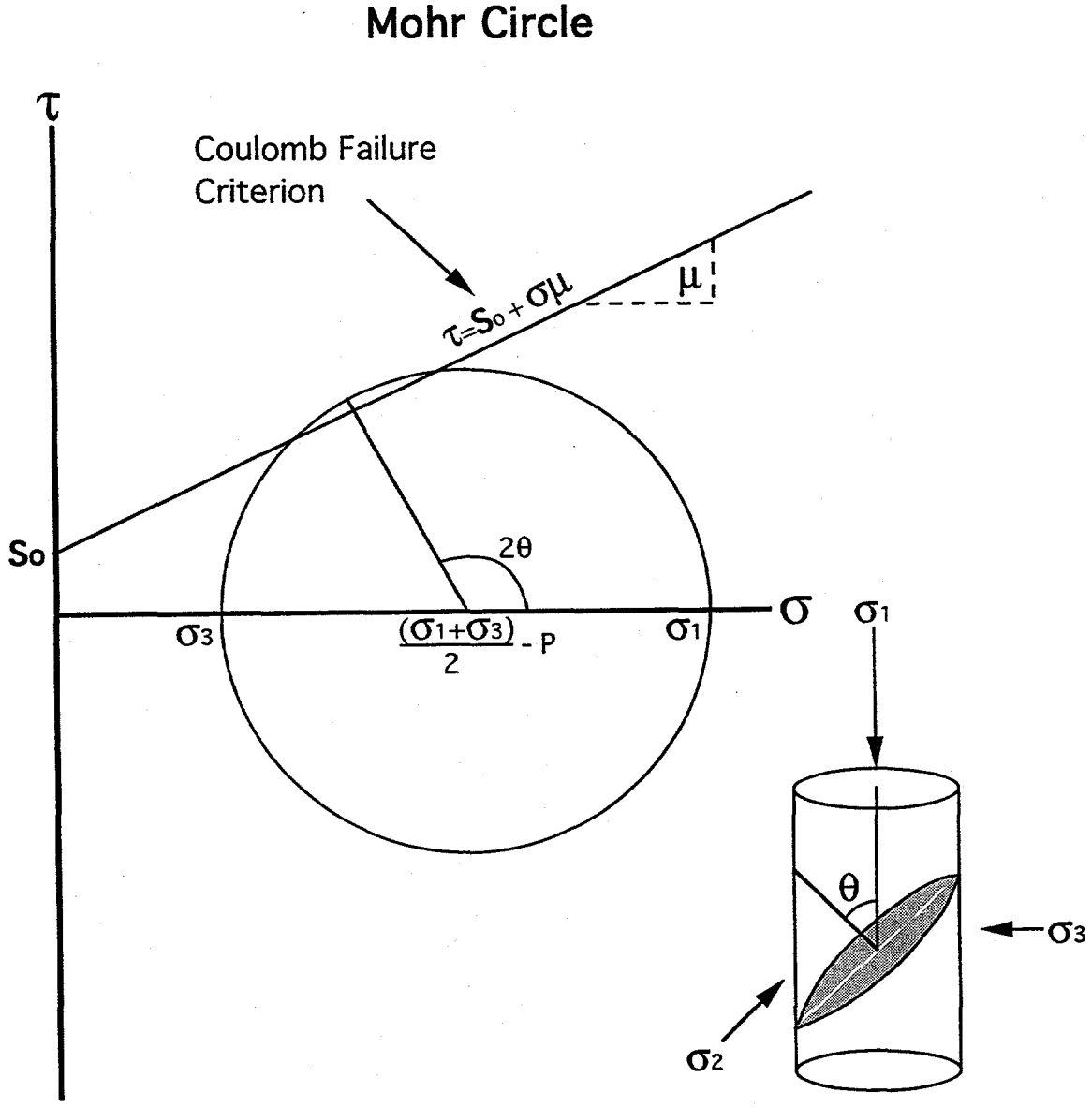

Figure 2.2 Mohr circle representation of normal (horizontal axis) and shear stress (vertical axis) across a fracture. A tri-axial compressional configuration, where $\sigma_1>\sigma_2>\sigma_3$ and similar to the stress field existing at depth, is shown. θ is the angle between the normal vector of the fracture and the σ_1 direction, P is the pore pressure and σ and τ are the normal and shear stresses, respectively. The line represents the Coulomb failure criterion. Here S_o is the cohesional strength of the rock; and μ is the frictional coefficient of the fracture surface.

of fluid were accommodated by contraction in the direction of the maximum principal stress, then the volume change would induce shear stress leading to shear failure. In the Mohr circle, this is represented by an increase in σ_1. This extends the diameter of the circle causing the circumference to intersect the Coulomb failure line. Subsidence is a special case of volumetric change where the direction of the maximum principal stress, σ_1, is vertical. A similar mechanism proposed by Denlinger and Bufe (1982) pointed out that pore-pressure decline could induce fracture deflation. That, in turn, increases shear stress across the fractures leading to shear failure. Another mechanism for induced seismicity is the cooling of fracture surfaces that could decrease the effective normal stress (Denlinger, 1980). Temperature decrease could result from both steam withdrawal and injectate invading reservoir rocks, which could induce shear failure. Yet another mechanism proposed to explain the occurrence of seismicity at The Geysers is stick-slip behavior (Allis, 1982). A transition from aseismic creep to seismic slip could occur in response to both temperature and pore pressure decline or an increase in the coefficient of friction due to the deposition of silica from boiling pore water and the de-watering of clay. This is shown in Mohr circle as a movement of the circle to the right or an increase in the slope of the Coulomb failure line, both of which leads to "fracture/fault strengthening". In both cases, a stable aseismic creep behavior is converted to seismic slip because the fault can support higher stress loads.

The mechanisms discussed above may explain occurrence of the observed seismic activity in geothermal regions. Geothermal reservoirs are in a constant state of change, especially if the resource is being exploited. Continual fluid movement, heat transfer, chemical alterations and tectonic strain are some of the dynamic processes occurring in geothermal regions. Seismic activity is invariably connected to all these processes and may be indicative of the balance between fluid withdrawal and recharge as argued by McGarr (1976) and Majer and McEvilly (1979). Microearthquakes thus could be used to monitor changes in the evolving reservoir by analyzing the spatial and

temporal distribution of seismicity.

The microearthquakes also can be used to construct velocity and attenuation models of the reservoir. Several studies have used the high level of seismicity to delineate the geothermal reservoir, e.g. Ponko and Sanders (1994), Romero at al. (1994), Julian et al. (1993), O'Connell and Johnson (1991) and Eberhart-Phillips (1986). As a reservoir management tool, detectable variations of these models with time would be useful in tracking the changes in geothermal reservoir.

2.3 Physical Basis For Seismic Velocity And Attenuation Interpretations

2.3.1 Seismic Velocity

Seismic velocity has been used extensively to characterize various minerals and rock types (a compilation is given by Carmichael, 1982) In most cases, these measurements of seismic velocity were done on laboratory rock samples that no longer represent rocks in situ where properties are influenced by local conditions such as porosity, fracture density, degree of fluid saturation, pore pressure and temperature. Within a geothermal reservoir, all of these parameters are probably anomalous. The following discussion reviews the relationship between seismic velocity and these factors. A fully-saturated rock sample with an average fracture density and temperature consistent with the average geothermal gradient is used as a reference. The changes in seismic velocity brought about by perturbations from the reference state are considered.

2.3.1.1 Fluid Saturation

Fully-saturated rocks have higher P-wave velocities than unsaturated rocks. Nur and Simmons (1969) reported that the P-wave velocity increases by 20% if a dry rock is saturated with water. White (1975) found similar increases in the P-wave velocity with full saturation but reported no change in the S-wave velocity. The effect of liquids in joints is to increase the specific stiffness to compressional waves, but it does not inhibit the relative shear displacement across the joints. As a result, higher liquid saturation increases the effective Vp/Vs ratio while partial saturation (dry or gas-filled fractures) depresses it (Toksöz et al., 1976; Gregory, 1976). Christensen (1986) and Meissner and Theilen (1986) found that the presence of a gas-phase in fractures, or an increase in pore pressure, decreases the P-wave velocity. The P wave velocity of porous rocks has been shown theoretically and experimentally to be more sensitive to fluid saturation changes than the S-wave velocity (Castagna et al., 1985; O'Connell and Budiansky, 1974, 1977). Christensen (1984) demonstrated that Vp/Vs values increase with pore pressure at constant confining pressure. High Vp/Vs has been reported in liquid-dominated geothermal systems such as Travale field, Italy (Hirn and Ferrucci, 1985) while low Vp/Vs has been found in vapor-dominated ones such as The Geysers, California (Majer and McEvilly, 1979; O'Connell and Johnson, 1991), at the Yellowstone National Park (Chaterje et al., 1985), and Coso geothermal field, California (Walck, 1988).

2.3.1.2 Fracture Density

An increase in fracture density generally decreases the effective moduli of rocks. The theoretical studies by O'Connell and Budiansky (1974, 1977) show that an increase in fracture density in a dry rock decreases both P- and S-wave velocities, however, it has a more pronounced decline in the P-wave velocity so that Vp/Vs decreases . They found an increase in fracture abundance in a fully saturated rock to decrease both P- and

S-wave velocities, but S-wave velocity drops faster than the P-wave velocity, resulting in higher Vp/Vs ratio. Moos and Zoback (1983) also found that the presence of fully-saturated fractures decreases both P and S-wave velocities, and increases Vp/Vs. Fracture geometry has a profound effect on seismic velocities. Thin voids decrease the effective elastic moduli more than spherical voids (Toksöz et al., 1976; Mavko, 1980). In addition, large cracks reduce the elastic moduli more than a great number of small cracks with the same total crack area (O'Connell and Budiansky, 1974).

2.3.1.3 Temperature and Melting

Temperature increase mechanically weakens the rocks and decreases both the P- and S-wave velocities. Murase and McBirney (1973) found a 50% drop in the P-wave velocity in melts of volcanic rocks with variable silica concentrations. In a theoretical study, Mavko (1980) showed that partial melting decreases both P- and S-wave velocities and increases the Vp/Vs ratio. Sato et al. (1989) report a 2% decrease in P-wave velocity per 100^{o}C drop below the solidus of dry peridotite. They found a rapid drop in P-wave velocity of several tens of percent at solidus . Other laboratory studies using metal alloys showed that seismic velocity decreases with increasing temperature below the solidus and rapidly declines at the onset of melting (Christensen and Wepfer, 1989). Mizutani and Kanamori (1964) reported that S-wave velocity decreases four times faster than the P-wave velocity as the temperature of a metal alloy approaches solidus. At liquidus temperature, the S-wave velocity drops by 100% while the P-wave velocity decreases by 20%. Vp/Vs increases as temperature increases, and increases significantly with the onset of melting. About 90% of the total decrease in the P- and S-wave velocities occur in a narrow temperature range just below the solidus. The theoretical study of Mavko (1980) showed that the greatest reduction in velocity is expected where the melt is in film geometry, and the least where in a tubular geometry.

2.3.1.4 Lithology and Hydrothermal Alterations

Rock type and the degree of hydrothermal alterations will also influence seismic velocities in geothermal environments. Lin and Wang (1980) found that metamorphism of Franciscan graywacke could increase the P-wave velocity significantly. Deposition of silica from boiling pore water could increase the effective bulk modulus in thereby increasing the P-wave velocity. On the other hand, dissolution of deposited materials could decrease both the bulk and shear moduli and may invariably reduce P- and S-wave velocities. These offsetting effects may reduce the ability to distinguish these factors. Independent data are critical in resolving these mechanisms. Many of these above effects may be present in combination in a typical geothermal reservoir. Seismic wave attenuation provides independent and complementary information on the mechanical state of rocks in geothermal environments.

2.3.2 Seismic Wave Attenuation

Attenuation properties provide evidence on the mechanical state of rocks at depth. The same factors that affect seismic velocities, such as porosity, degree of fracturing, fluid saturation, pressure, temperature and partial melt are known to influence seismic attenuation. Q, the reciprocal of attenuation, is seen to vary over a wider range (10-500) than velocity (4-6 km/s) in shallow crustal rocks. A primary cause of intrinsic anelastic attenuation (as opposed to elastic scattering) is fluid flow between cracks and variations in crack geometry can account for the relative constancy of Q^{-1} over a wide frequency band (O'Connell and Budiansky, 1977). At microearthquake frequencies (1-100 Hz), the dominant absorption mechanism is proposed to be grain-boundary friction (Johnston et al., 1979). Attenuation for porous

rocks increases with increasing liquid saturation (Anderson et al, 1965; Winkler and Nur, 1979). At full saturation, $Q_p^{-1}/Q_s^{-1} < 1$, however Q_p^{-1} decreases considerably even with slight decrease in saturation so that at 95% saturation $Q_p^{-1}/Q_s^{-1} > 1$. Thus, small gas inclusions can significantly decrease Q_p^{-1}.

Murase and McBirney (1973) reported that Q_p^{-1} increased continuously with increasing temperature for basaltic, andesitic and rhyolitic rocks. Kampfmann and Berckhemer (1985) reported a linear increase in Q_s^{-1} with temperature for basaltic samples. The increase in Q_s^{-1} occurred at subsolidus temperature and does not necessitate partial melting. Mizutani and Kanamori (1964) found Q_p^{-1} about 90% higher in liquid compared to a solid metal alloy with most of the increase occurring near and at liquidus. In a theoretical study on the influence of melt geometry on attenuation, Mavko (1980) found that melts in thin films increase the effective attenuation more than spherical melts . Similarly, small amounts of liquid distributed in thin films significantly increase Q^{-1} (Mavko and Nur, 1979). Confining pressure decreases attenuation because of fracture closure, reducing frictional losses due to fluid flow. Johnston and Toksoz (1980) showed that Q^{-1} decreases with increasing confining pressure.

If the same factors are affecting both velocity and attenuation, then variations in velocity and attenuation will be related. Attenuation will increase with increasing fracture density, degree of metamorphism and alteration.

2.4 Summary

This chapter reviewed the relationship between microearthquakes and geothermal systems. The different types of geothermal systems were discussed and a survey of the possible mechanisms for microearthquakes induced by geothermal processes was presented. Physical conditions known to exist in geothermal environments and that can

affect the seismic velocity and attenuation of reservoir rocks were reviewed.

The degree of liquid saturation can significantly influence seismic velocity and attenuation. Velocity and attenuation are sensitive to slight changes in gas content, a property that is useful in delineating two-phase and steam reservoirs. Direct temperature effects on seismic velocity and attenuation are probably negligible in typical geothermal regions where the temperature is rarely more than 400°C. Indirectly however, temperature increase causes boiling of pore water to steam, influencing the degree of liquid saturation and thus affecting both the velocity and attenuation. To a lesser extent, fracture density, degree of metamorphism and alteration acting in combination can also affect the velocity and attenuation of reservoir rocks. All of these processes must be considered in the interpretation of the resulting velocity and attenuation models in the characterization of the geothermal reservoirs.

Seismic tomographic techniques are used in this dissertation to characterize geothermal systems. Chapter three is the 3-D velocity inversion study conducted at the Northwest Geysers geothermal field (Romero et al., 1995), including a study of the occurrence of microearthquakes. Chapter four presents the 3-D attenuation structure beneath the Northwest Geysers geothermal field (Romero et al., 1995). Chapter five is the velocity inversion study at the Long Valley caldera (Romero et al., 1993). Lastly, chapter six summarizes the conclusions as to the utility of seismic inversion techniques in the investigation of geothermal regions.

Chapter 3

CHARACTERIZATION OF THE NORTHWEST GEYSERS STEAM FIELD, CALIFORNIA FROM SEISMICITY AND VELOCITY PATTERNS

3.1 Introduction

The Geysers is a vapor-dominated geothermal field situated within the central belt of the Franciscan Assemblage located in the northern California Coast Ranges (Figure 3.1). At The Geysers, the Franciscan Assemblage is a complex of metasedimentary rocks consisting mainly of metamorphosed turbidite graywacke with lesser amounts of chert, argillite, greenstone, and serpentinized ultramafic rocks juxtaposed during the Mesozoic to early Tertiary subduction of the Farallon plate beneath the North American continent (Blake and Jones, 1974; McLaughlin, 1981). The surface geology of the study area, located at the Northwest Geysers region (Figure 3.2), reflects the general geology of the region. The Geysers steam reservoir lies primarily within an indurated and fractured metagraywacke, locally called the "main graywacke", and is overlain by Franciscan greenstone melanges and unfractured metagraywacke in steeply dipping thrust packets that constitute the cap rock (Thompson, 1992). The subsurface structure generally dips to the northeast and is deformed by major northwest trending faults related to the San Andreas fault system (Figure 3.1). McNitt et al. (1989), integrating earlier geologic studies by McNitt (1968), McLaughlin (1981), and Thomas (1981), concluded that the steam reservoir is contained within a northeast-dipping structural high bounded on the southwest by the Big Sulphur Creek fault and on the northeast by the contact between the graywacke-shale cap rock and the reservoir metagraywacke. Elsewhere, the reservoir boundaries are roughly delineated

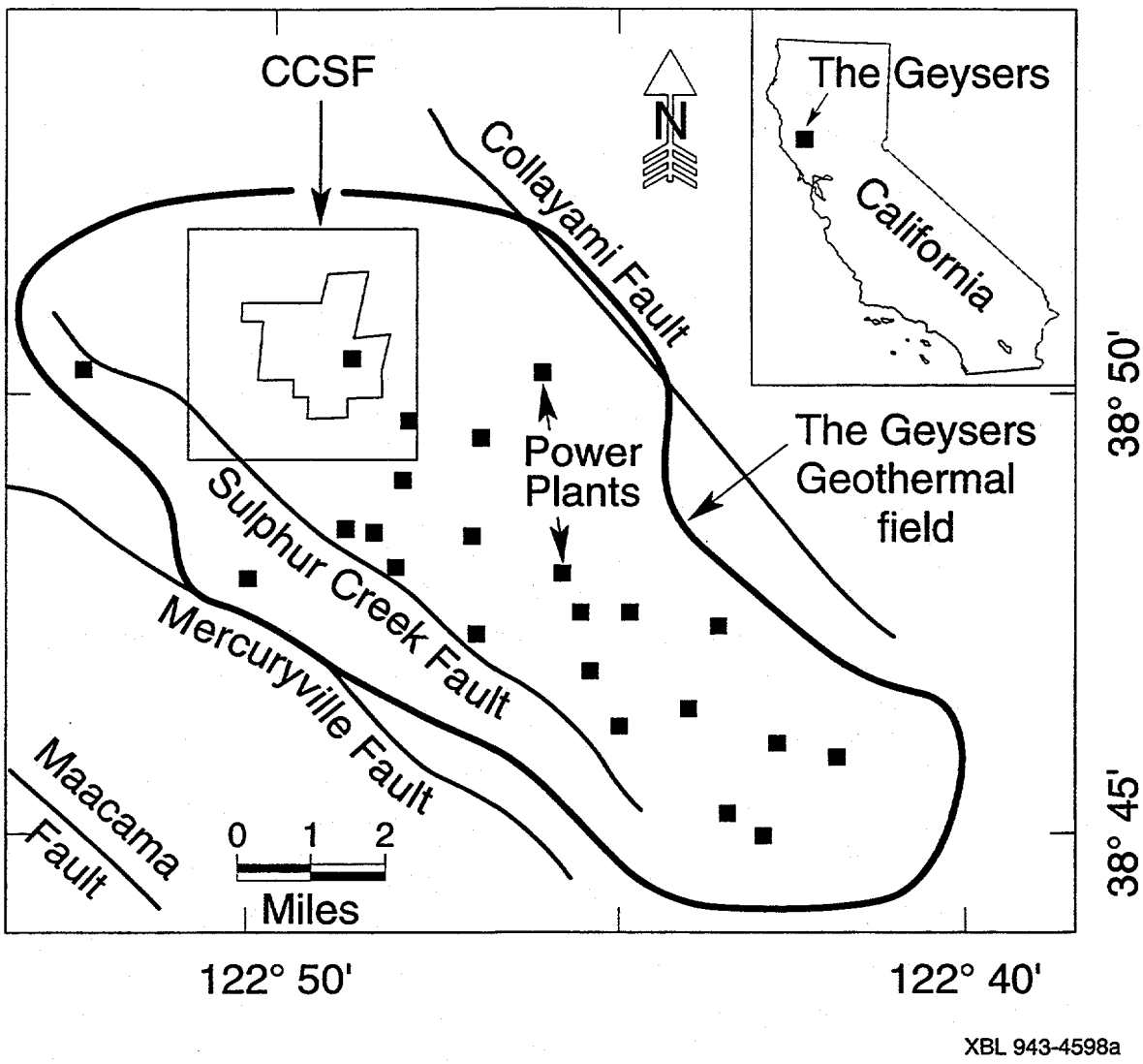

Figure 3.1 Location map of The Geysers geothermal field and the Northwest Geysers area (from Thompson, 1992). The Coldwater Creek Steam Field (CCSF) is shown for reference. Small squares mark power plant locations.

Figure 3.2 Simplified surface geologic map of the Northwest Geysers region (adopted from Nielson et al., 1991). CCSF is shown by the dotted outline. Heavy lines represent mapped faults and major geologic contacts in the area (Adapted from field mapping by M. Walters).

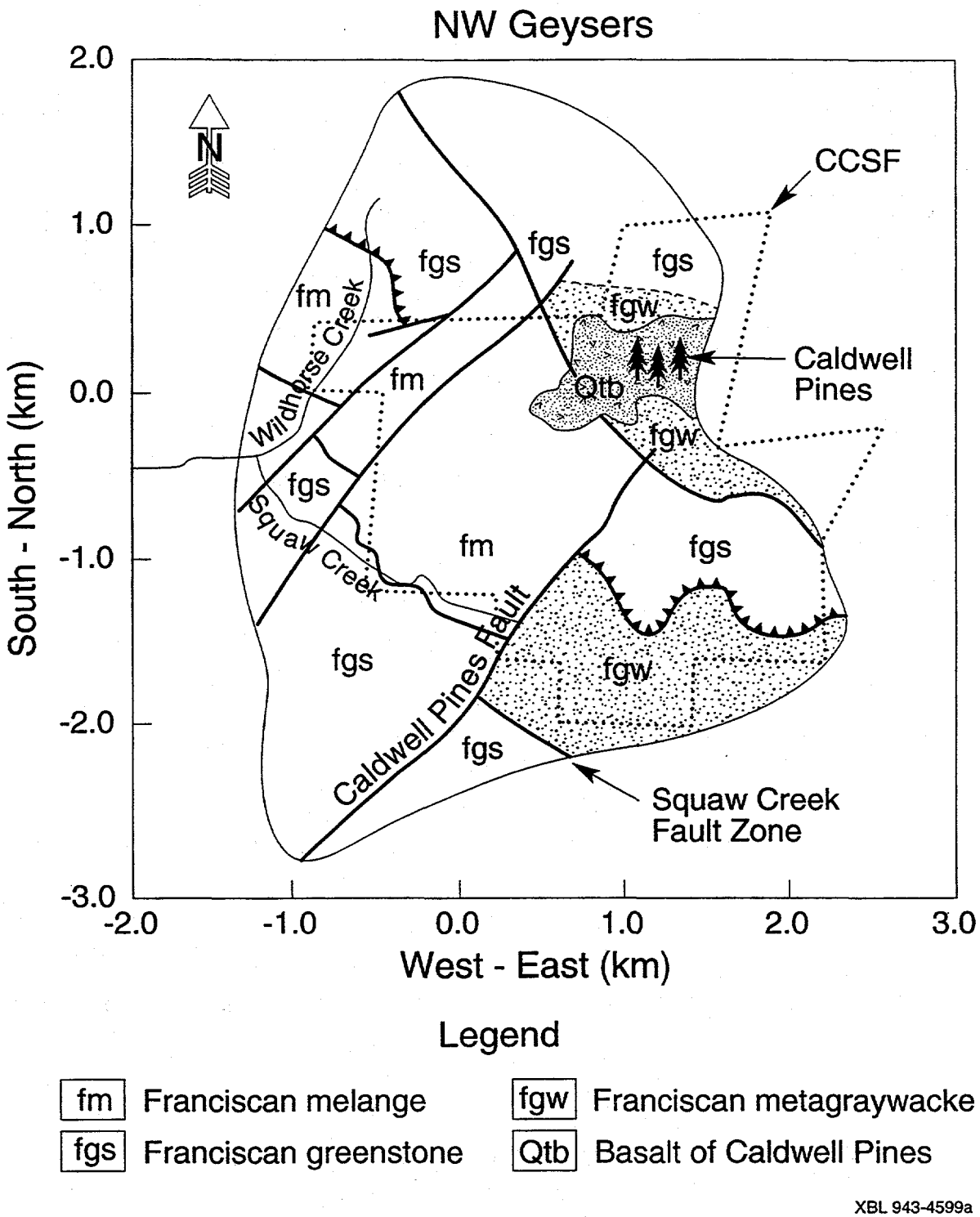
NW Geysers
2.0
1.0
0.0
-1.0
-2.0
-3.0
South - North (km)
-2.0
-1.0
0.0
1.0
2.0
3.0
West - East (km)
N
CCSF
Caldwell Pines
Squaw Creek Fault Zone
Wildhorse Creek
Squaw Creek
Caldwell Pines Fault
fm
fgs
fgw
Qtb
Legend
fm Franciscan melange
fgs Franciscan greenstone
fgw Franciscan metagraywacke
Qtb Basalt of Caldwell Pines
XBL 943-4599a

Figure 3.2

by a series of dry wells to the northwest and southeast.

A silicic pluton (felsite) intruded the base of the metagraywacke during the Pleistocene, accompanied by the extrusion of the equivalent Clear Lake volcanics which are exposed over a large area northeast of the field (Schriener and Suemnicht, 1980). This felsite body, which has a roughly antiformal shape with a linear axis striking northwest, may underlie the whole field (Thompson, 1992). The felsite lies entirely in the subsurface. Good correlation exists between the top of the steam reservoir and the depth to the felsite (Hulen and Walters, 1993). The shallowest steam entries occur at the central and southeastern parts of the field where the felsite is shallowest. Steam entries deepen towards the northwest where the felsite is deeper (Thomas, 1981; Hebein, 1983, 1986; Sternfeld, 1989). The emplacement of the felsite is believed to have hydrothermally altered and hydraulically fractured the brittle metagraywacke, thereby increasing its permeability to host the present geothermal reservoir.

A number of seismological studies at The Geysers have exploited the high level of seismicity as natural sources for imaging the geothermal reservoir. Using multiple-event Wadati plots, Majer and McEvilly (1979) found high P- and S-wave velocities within the production area. Eberhart-Phillips (1986), using arrival times from 170 local earthquakes, developed a three-dimensional (3-D) P-wave velocity model that contained high seismic velocities within the production area and lower velocities on the Collayami and Maacama fault zones, bounding the known reservoir to the northeast and southwest (Figure 3.1). O'Connell and Johnson (1991) conducted a progressive inversion for P- and S-wave velocities using 39 microearthquakes. They observed peaks in Vp/Vs ratio at shallow depths which they interpret as the steam condensation zone. Majer and McEvilly (1979) reported low Vp/Vs values within the steam producing horizon. This observation is consistent with the vapor-dominated nature of the reservoir. Vp/Vs values slowly increase with depth, indicating increasing liquid saturation in the reservoir rocks (Toksöz et al., 1976; Gregory, 1976). On the basis of station delays O'Connell

and Johnson (1991) also inferred a high-velocity anomaly in the Southeast Geysers. More recently, Julian et al. (1993) developed a 3-D, P-wave velocity model for the Central Geysers, attributing several high-velocity bodies to the hornfelsic-graywacke aureole above the felsite and to a sliver of high-density melange. They also found a low-velocity anomaly near the west-central part of The Geysers between the Mercuryville and Big Sulphur Creek faults which they believe is due to hydrothermally-altered material. In a study correlating P-wave velocity and attenuation structure, Zucca et al. (1994) reported a high P-wave velocity associated with the felsite body and low velocity in the steam reservoir. In this study 3-D, P- and S-wave velocity models are developed for the Coldwater Creek Steam Field (CCSF) at the Northwest Geysers region (Figures 3.1 and 3.2). The microearthquake hypocenters are also relocated using the new velocity models. The seismicity and the resulting velocity structures are interpreted in terms of the active geothermal system.

3.2 Data and Methodology

Beginning in March 1990, Lawrence Berkeley Laboratory undertook the archiving and interpretation of the microearthquake data from a 16-station, digital, three-component, high-frequency (400 samples/sec/channel) network in place at the Northwest Geysers region. The study focused on approximately 5000 microearthquakes recorded in 1988 prior to full production and injection activities. A set of 480 events, distinguished by high signal-to-noise ratios (>20) and with a minimum of 10 impulsive P-wave arrivals, were selected for the inversion. Figure 3.3 presents the station distribution, the inversion nodes, and the epicenters of the microearthquakes used in the inversion. Most of these events were characterized by sharp P-wave arrivals, making it possible to pick arrival times to an accuracy of one sample interval, or

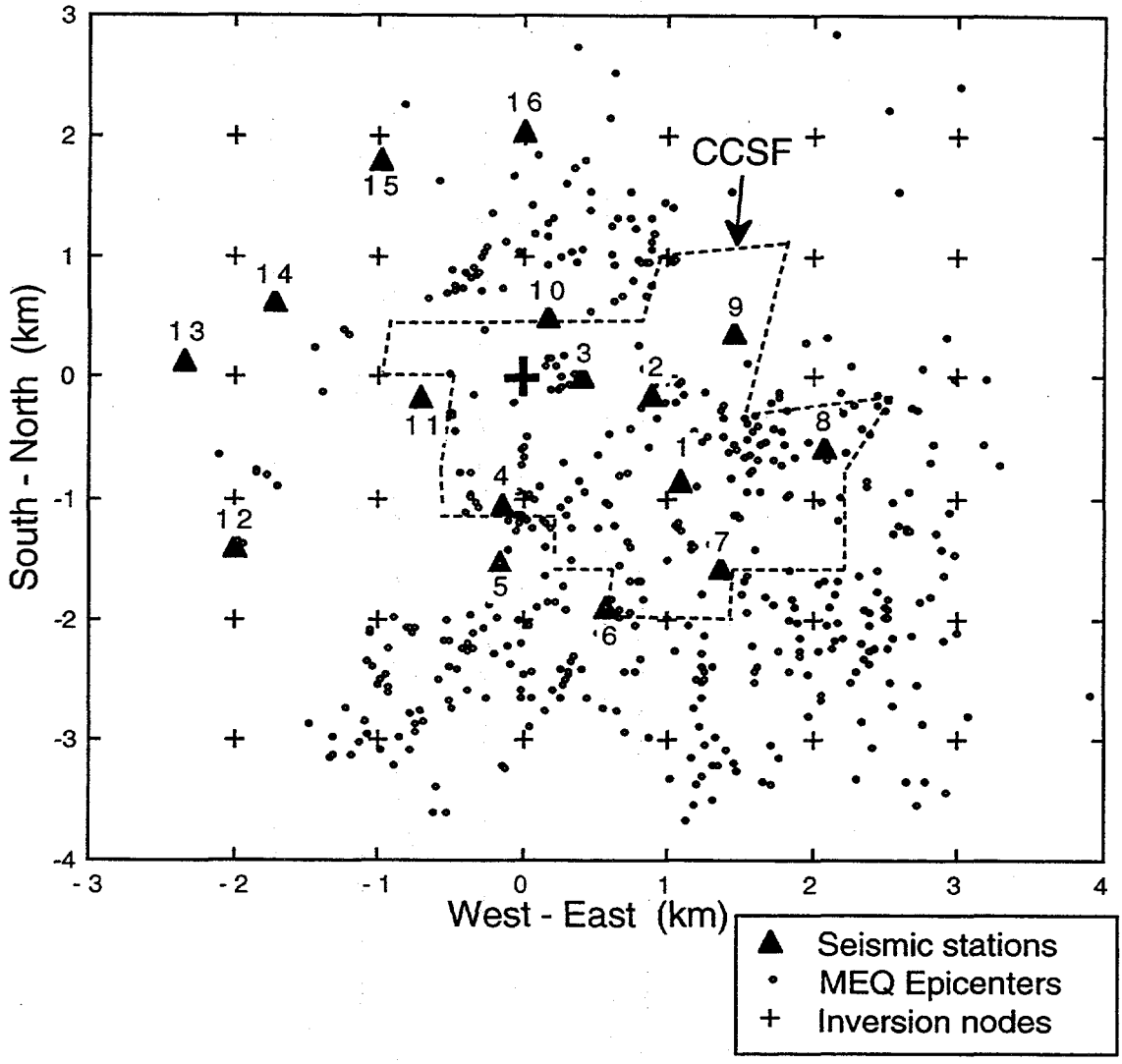

Figure 3.3 Map showing the station locations (triangles), inversion nodes (small crosses) and the epicenters of the 480 microearthquakes (small dots) used in the inversion. The origin of the local coordinates is centered at 38°50.55'N, 122°49.64'W (large cross). CCSF outline is given for reference.

2.5 ms. The S-wave arrival times were picked on the horizontal components only when they were distinct and unambiguous. Picks that differ by more than 10 ms between the two horizontal components were discarded, a complication induced by S-wave splitting. Events that were well-distributed within the region of interest were selected. In areas with fewer microearthquakes, such as the region west of the CCSF, lower-quality events were selected to achieve uniformly dense ray coverage. The final data set consisted of approximately 9700 arrival times, including about 2700 S-wave arrivals.

The problem of simultaneous earthquake relocations and velocity inversion is solved using the method of progressive inversion proposed by Thurber (1983), modified by the incorporation of cubic spline interpolation (Michelini and McEvilly, 1991). The following discussion of this technique follows Michelini and McEvilly (1991). The method of simultaneous inversion of seismic-wave arrival times for earthquake locations and velocity structure minimizes travel-time residuals using damped least-squares. Because the problem is non-linear, solutions are found by linearizing the problem and solving iteratively. The following discussion of the technique is patterned after the formulation of Thurber (1983) and Michelini and McEvilly (1991). Theoretical travel times are first calculated for each ray path using a 3-D ray tracer. Velocity $V(x,y,z)$ at any position is solved using the cubic spline interpolation:

$$V(x,y,z) = \sum_{i,j,k=1}^{N} \rho_{ijk}(x,y,z) a_{ijk} \qquad (1)$$

where $\rho_{ijk}(x,y,z)$ are the normalized cubic-spline basis functions; N the number of basis functions; a_{ijk} the velocity spline coefficients. The travel-time residual r which is the difference between the observed and the calculated arrival time for each source-receiver pair, can be expressed to the first order as follows:

$$r = \Delta t + \frac{\partial t}{\partial x}\Delta x + \frac{\partial t}{\partial y}\Delta y + \frac{\partial t}{\partial z}\Delta z + \sum_{i,j,k=1}^{IJK} \frac{\partial t}{\partial a_{ijk}}\Delta a_{ijk} + \sum_{i=1}^{M} \frac{\partial t}{\partial s_m}\Delta s_m \qquad (2)$$

where:

$\Delta t, \Delta x, \Delta y, \Delta z$ are the perturbations to the origin time and hypocentral parameters; $\frac{\partial t}{\partial x}, \frac{\partial t}{\partial y}, \frac{\partial t}{\partial z}$ the derivatives of the travel times with respect to the hypocentral coordinates;

Δa_{ijk} the perturbations to the velocity spline coefficients;

$\frac{\partial t}{\partial a_{ijk}}$ the derivatives of the travel times with respect to the velocity coefficients;

IJK the total number of velocity parameters along the x,y,z axes, respectively;

Δs_m the perturbations to the station delays;

M the total number of stations; and

$\frac{\partial t}{\partial s_m}$ the partial derivatives of the travel times with respect to the station delays.

$\frac{\partial t}{\partial x}, \frac{\partial t}{\partial y}, \frac{\partial t}{\partial z}$ are obtained from:

$$\frac{\partial t}{\partial x} = -\frac{1}{V}\frac{dx}{ds}, \quad \frac{\partial t}{\partial y} = -\frac{1}{V}\frac{dy}{ds}, \quad \frac{\partial t}{\partial z} = -\frac{1}{V}\frac{dz}{ds}$$

where *x, y,* and *z* are the hypocenter coordinates, *V* is the velocity at the hypocenter and *ds* the element of length along the ray path. $\frac{\partial t}{\partial a_{ijk}}$ is obtained from:

$$\frac{\partial t}{\partial a_{ijk}} = -\int_{source}^{receiver} \left(\frac{1}{V(x,y,z)}\right)^2 \frac{\partial V(x,y,z)}{\partial a_{ijk}} ds$$

Each earthquake i yields a set of matrix equation:

$$\mathbf{r}_i = \mathbf{H}_i \Delta \mathbf{h}_i + \mathbf{M}_i \Delta \mathbf{m}_i + \mathbf{S}_i \Delta \mathbf{s}_i \qquad (3)$$

where $\mathbf{H}_i$ is the matrix of $\frac{\partial t}{\partial x}, \frac{\partial t}{\partial y}, \frac{\partial t}{\partial z}$; $\Delta \mathbf{h}_i$ the perturbations to the hypocentral parameters, $\mathbf{M}_i$ the matrix of $\frac{\partial t}{\partial a_{ijk}}$; and $\Delta \mathbf{m}_i$ the perturbations to the velocity coefficients. Parameter separation (Pavlis and Booker, 1980) is used to decouple the hypocenter location from the velocity adjustment problem by applying a linear annulling transformation:

$$\mathbf{Q}_i^T \mathbf{H}_i = \mathbf{0}$$

resulting in the reduced problem:

$$\mathbf{r}_i^r = \mathbf{M}_i^r \Delta\mathbf{m}_i + \mathbf{S}_i^r \Delta\mathbf{s}_i$$

Defining an expanded matrix $\mathbf{M}_i^e = \langle \mathbf{M}_i^r | \mathbf{S}_i^r \rangle$ and $\Delta\mathbf{m}_i^e = \langle \Delta\mathbf{m}_i | \Delta\mathbf{s}_i \rangle$ such that

$$\mathbf{r}_i^r = \langle \mathbf{M}_i^r | \mathbf{S}_i^r \rangle \left\langle \frac{\Delta\mathbf{m}_i}{\Delta\mathbf{s}_i} \right\rangle = \mathbf{M}_i^e \Delta\mathbf{m}_i^e$$

The matrix equation is solved using the damped least-squares procedure

$$\Delta\mathbf{m}_i^e = \left(\mathbf{M}_i^{eT} \mathbf{M}_i^e + \varepsilon^2 \mathbf{I} \right)^{-1} \mathbf{M}_i^{eT} \mathbf{r}_i^r \qquad (4)$$

where $\mathbf{I}$ is an identity matrix and ε a damping parameter (Menke, 1989) . The matrix inverse is obtained using singular value decomposition. The resulting velocity and station delay adjustments $\Delta\mathbf{m}_i^e$ are added to the initial velocity model and new theoretical travel-times are then computed from the updated model. Travel-time residuals are recalculated and a system of linear equations is solved for new velocity adjustments. This procedure is repeated until the residuals fall below a predefined threshold which is based, in part, on the estimated picking errors. The process also terminates when the variance does not change significantly between iterations. Following Michelini and McEvilly (1991), the damping parameter is selected at each iteration so that the largest standard error of the velocity adjustments is less than a previously assigned threshold. Initially, the damping parameter is set to a large value which is then relaxed at each succeeding iteration as the solution converges and smaller data variances are obtained.

The region of interest was divided into a 3-D rectangular grid with seismic velocities assigned to each grid point. Based on the results of the synthetic tests discussed below, a grid spacing of 1 km (x 6 nodes) horizontally and 1 km (x 5 nodes) vertically centered on the region of interest was adopted. To limit the CPU time required in travel-time computation, the approximate ray tracer developed by Um and Thurber

(1987) was used. The starting velocity model was derived from the one-dimensional P-wave velocity model of O'Connell and Johnson (1991) and an assumed normal Vp/Vs ratio of 1.73.

3.2.1 Synthetic Data Tests and Model Errors

Tests with synthetic data were conducted to explore the resolving power of the data set and to determine an optimal parametrization for the actual inversion. In geophysical problems, parametrizations with a finite number of nodes impose a low-pass filter on true earth structure that degrades short-wavelength features, resulting in an artificially-smooth earth model. On the other hand, overly-fine node spacing leads to sparsely sampled nodes due to the limit imposed by the seismic ray density. Overparametrization leads to a poorly constrained model and hence large uncertainty in the model estimate. In order to find the optimum parametrization, synthetic arrival times were first generated from artificial starting models with varying node spacing and anomalies, using the same source-receiver geometry as in the real inversion problem. The synthetic travel times were randomly perturbed with times ranging from ±2 ms and ±10 ms for P and S arrivals, respectively, to simulate the effects of picking errors. The synthetic structures were then inverted for and the results were assessed by comparing recovered images to the original structures and evaluate the spatial variations of the model resolution matrix, **R**, for the resulting models.

The rows of **R** are the normalized averaging kernels which describe the influence of neighboring model parameters to the prediction of each model parameter (Menke, 1989). If **R** is the identity matrix, then each model parameter is uniquely determined. For this data set, results of the synthetic test showed that a node spacing of 1 km represents the optimum parametrization producing relatively good model resolution over the target region while still preserving small-scale features in the velocity structure.

Finer parametrization led to small-scale velocity oscillations while coarser ones produced smooth structures unrelated to the initial synthetic model. Figures 3.4a and 3.4b present the P- and S-wave model resolution over the target region. Shaded areas denote regions with good model resolution while lighter areas represent decreasing resolution. Blank areas at the edges of the target region indicate poor model resolution. The tests have shown that the center of the target region is reasonably well-resolved to a depth of 3 km. It is concluded that the inverse procedure can infer heterogeneity with scale lengths of 1 km within well-resolved regions. The P- and S-wave model uncertainties are superimposed in Figure 3.4 as contour lines. Standard errors range between 0.02 and 0.10 km/s and generally increase towards the edges of the model and also with depth. These model errors are less than 2% of the final velocity values. The final model exhibits an root mean square residual of 12 ms, an improvement of 64% after four iterations over the starting 1-D model. The robustness of the data set was investigated by using different starting models and evaluating the recovered models. To generate the starting models, the initial 1-D velocity model was perturbed with uniformly distributed random deviates ranging from 8 to 15 % velocity contrasts. The resulting P- and S-wave velocity models show remarkable similarity in that the main anomalies were consistently recovered, attesting to the robustness of the data set.

Figure 3.4 Plots of the model resolution and standard error. The horizontal cross sections are taken at several depths and centered at the CCSF (dotted outline). Datum plane is at 0.7 kmasl. Shading denotes variations in model resolution with dark areas having the highest resolution. Contour lines show standard errors with intervals of 0.01 km/s. (A) P-wave model. Cross section at 3 km depth has standard error of 0.1 km/s. (B) S-wave model. Cross section at 2 km depth has standard error of 0.04 km/s.

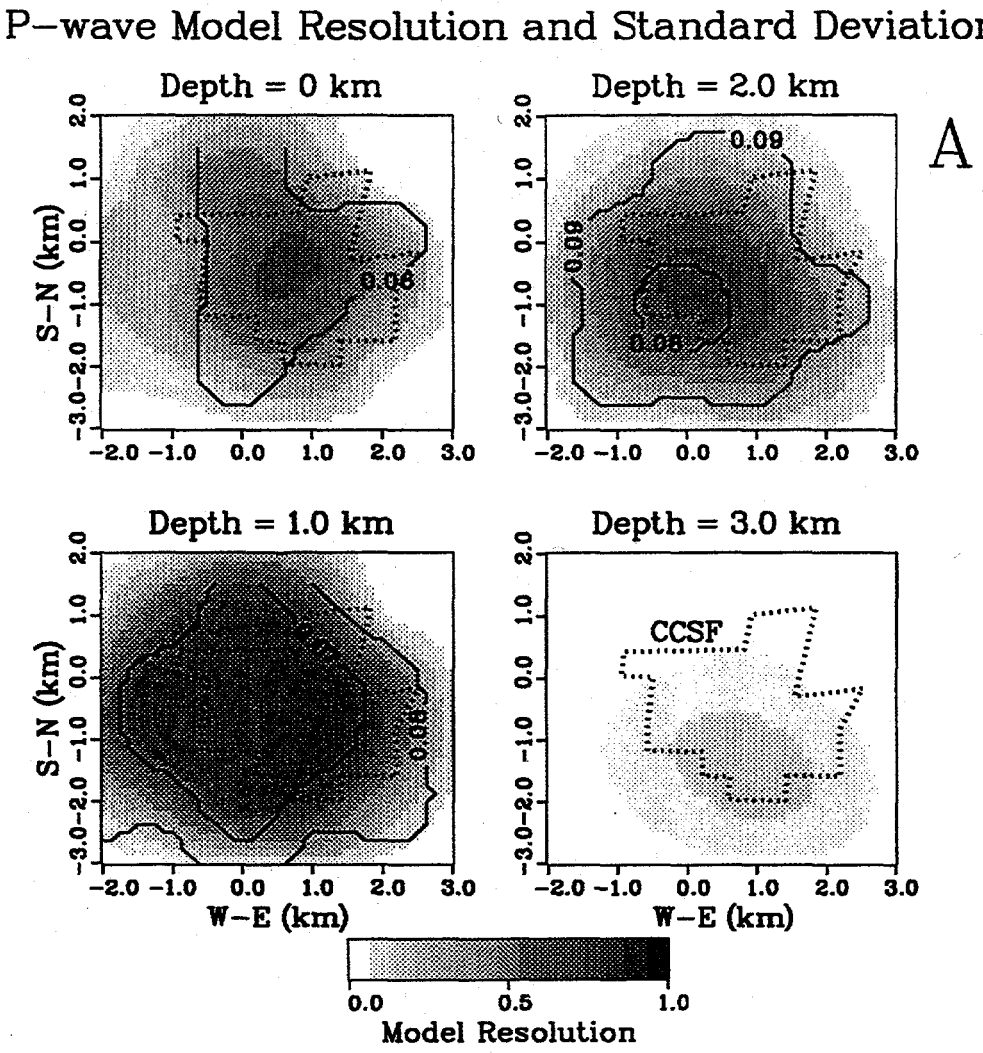
P–wave Model Resolution and Standard Deviation
Depth = 0 km
Depth = 2.0 km
Depth = 1.0 km
Depth = 3.0 km
A
0.09
0.06
0.08
CCSF
S–N (km)
W–E (km)
2.0
1.0
0.0
-1.0
-2.0
-3.0
-2.0 -1.0 0.0 1.0 2.0 3.0
0.0 0.5 1.0
Model Resolution

Figure 3.4a

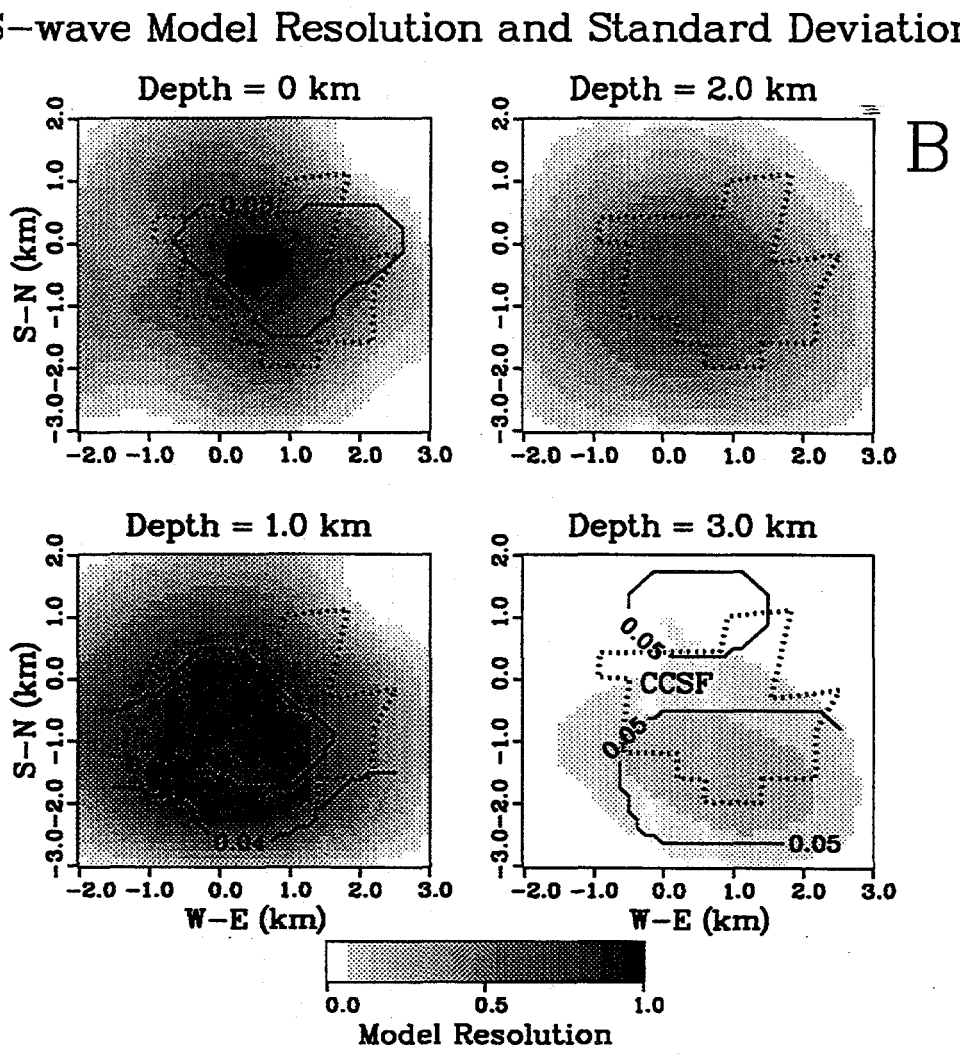
S–wave Model Resolution and Standard Deviation
Depth = 0 km
Depth = 2.0 km
B
Depth = 1.0 km
Depth = 3.0 km
CCSF
0.05
0.04
S–N (km)
W–E (km)
2.0
1.0
0.0
-1.0
-2.0
-3.0
-2.0 -1.0 0.0 1.0 2.0 3.0
0.0 0.5 1.0
Model Resolution

Figure 3.4b

3.3 Inversion Results

3.3.1 Relocated Hypocenters

Figures 3.5a and 3.5b show the 480 relocation vectors of the hypocenters used in the inversion in plan view and north-south cross-sections. The arrows show the shift in hypocentral locations with the 3-D velocity model relative to the 1-D locations. The average relocation shift along the x, y and z axes were : -95±121 m, -17±98 m, -13±120 m, respectively (The origin of the local coordinates is given in Figure 3.3). The relocated hypocenters exhibited a systematic movement to the west probably due to the station distribution and relatively higher velocities in the western half of the CCSF (Figure 3.5a). Figures 3.6a-c present in map view and two cross sections of about 5000 relocated events recorded at the NW Geysers in 1988. microearthquakes are concentrated within the CCSF extending south and east into the adjacent Unocal steam field. Seismicity in the CCSF is low to the north and west in the direction where the field is undeveloped. Seismicity occurs within two distinct depth zones. A shallow zone of seismicity between depths of 1.5 and 2.5 km underlies most of the CCSF. Depths are referenced to a datum plane 0.7 km above sea level (kmasl), the average elevation of the region. A deeper cluster of microearthquakes is located between 4 and 5 km depth just beyond the southeast edge of the CCSF. A cluster of microearthquakes with focal depths between 2 and 3 km is located beneath the injection well A, as shown in Figure 3.6. Injector A was an the only active injection well at that time. In an expanded view of the microearthquake cluster around injector A, Figures 3.7a-c clearly show the strong spatial correlation of the seismicity around the bottom of injector A and extending several hundred meters beneath the well. The microearthquake distribution seems to define a vertical planar structure striking roughly north-south. This result is compatible with the regional maximum stress direction which is oriented roughly north-

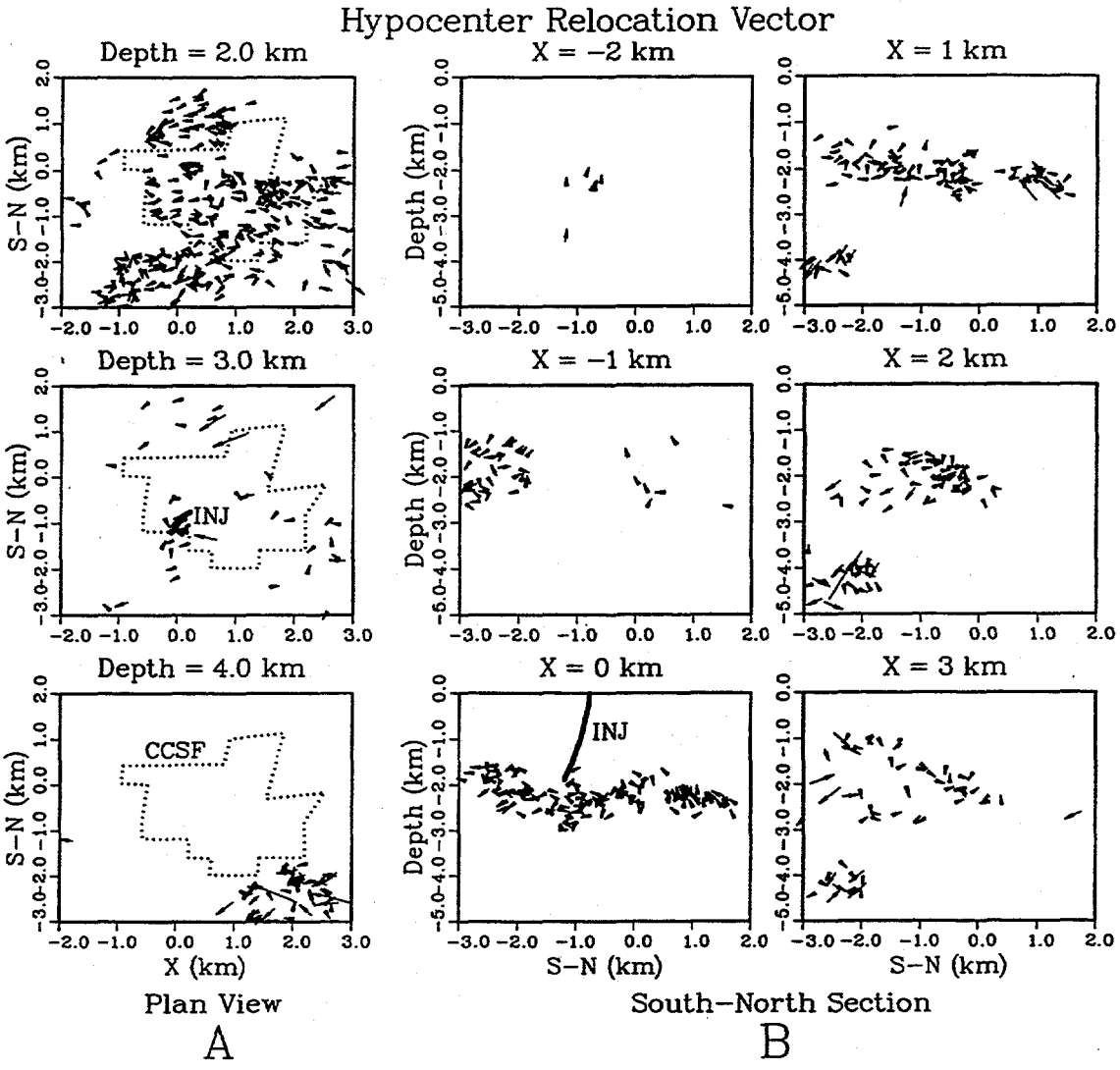

Figure 3.5 Hypocenter relocation vectors. Arrows denote the shift in hypocentral locations from a 1-D to a 3-D velocity model. Datum plane is at 0.7 kmasl. INJ denotes location and trace of injection well. (A) Plan view of the relocated hypocenters around the CCSF at several depths. Events within ±0.5 km of the layers are projected. CCSF outline is shown for reference. (B) North-south cross sections at several east-west positions.

Figure 3.6 Hypocenter relocation results. (A) Map view and of the relocated hypocenters of the events recorded in 1988 at the NW Geysers region. Local origin is centered at 38°50.55'N, 122°49.64'W. Triangles mark seismometer locations. (B) West-east cross section across the region with all events projected. (C) North-south cross section across the region with all events projected. Datum plane is 0.7 kmasl.

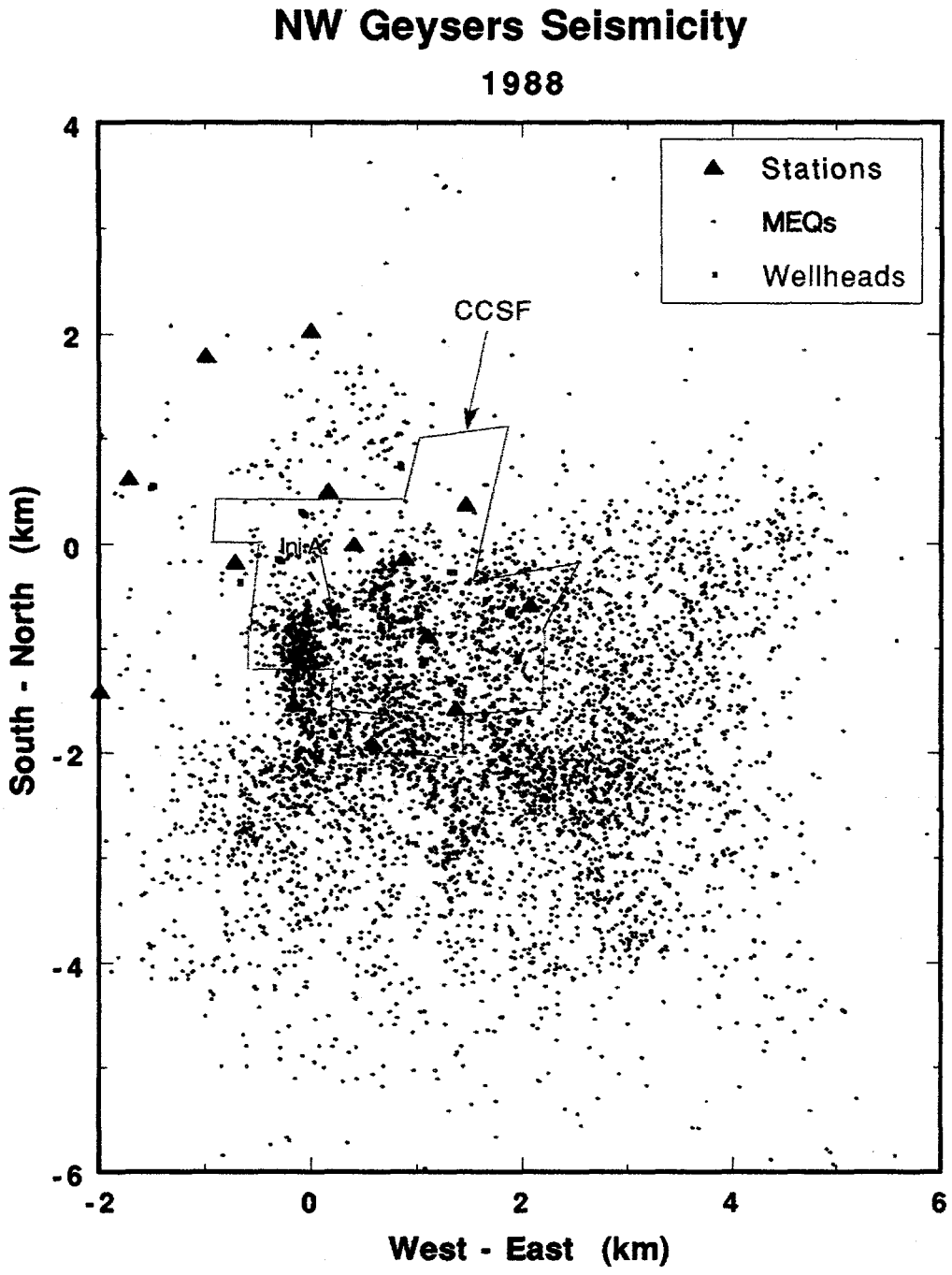
NW Geysers Seismicity
1988
Stations
MEQs
Wellheads
CCSF
Ini-A
South - North (km)
West - East (km)
4
2
0
-2
-4
-6
-2
0
2
4
6

Figure 3.6a

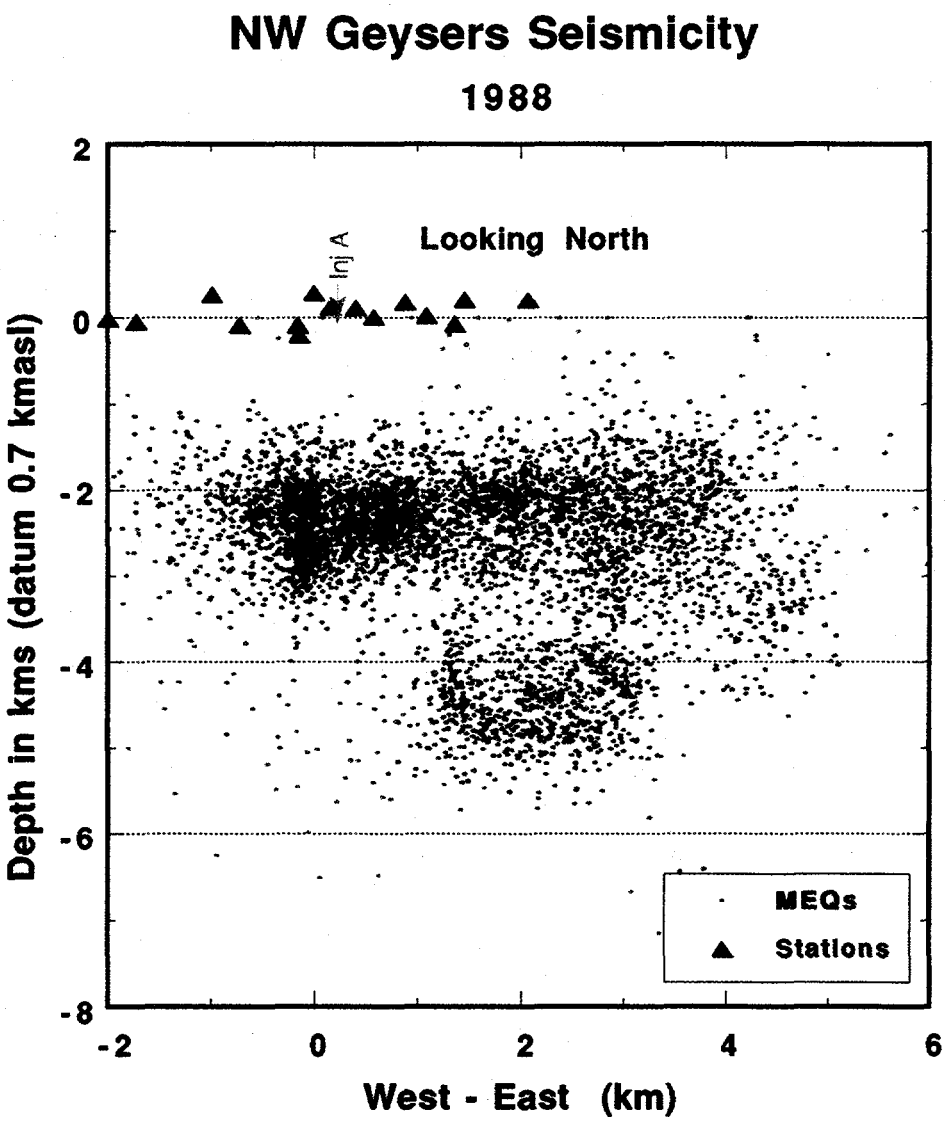
NW Geysers Seismicity
1988
Looking North
Inj A
Depth in kms (datum 0.7 kmasl)
2
0
-2
-4
-6
-8
-2
0
2
4
6
West - East (km)
MEQs
Stations

Figure 3.6b

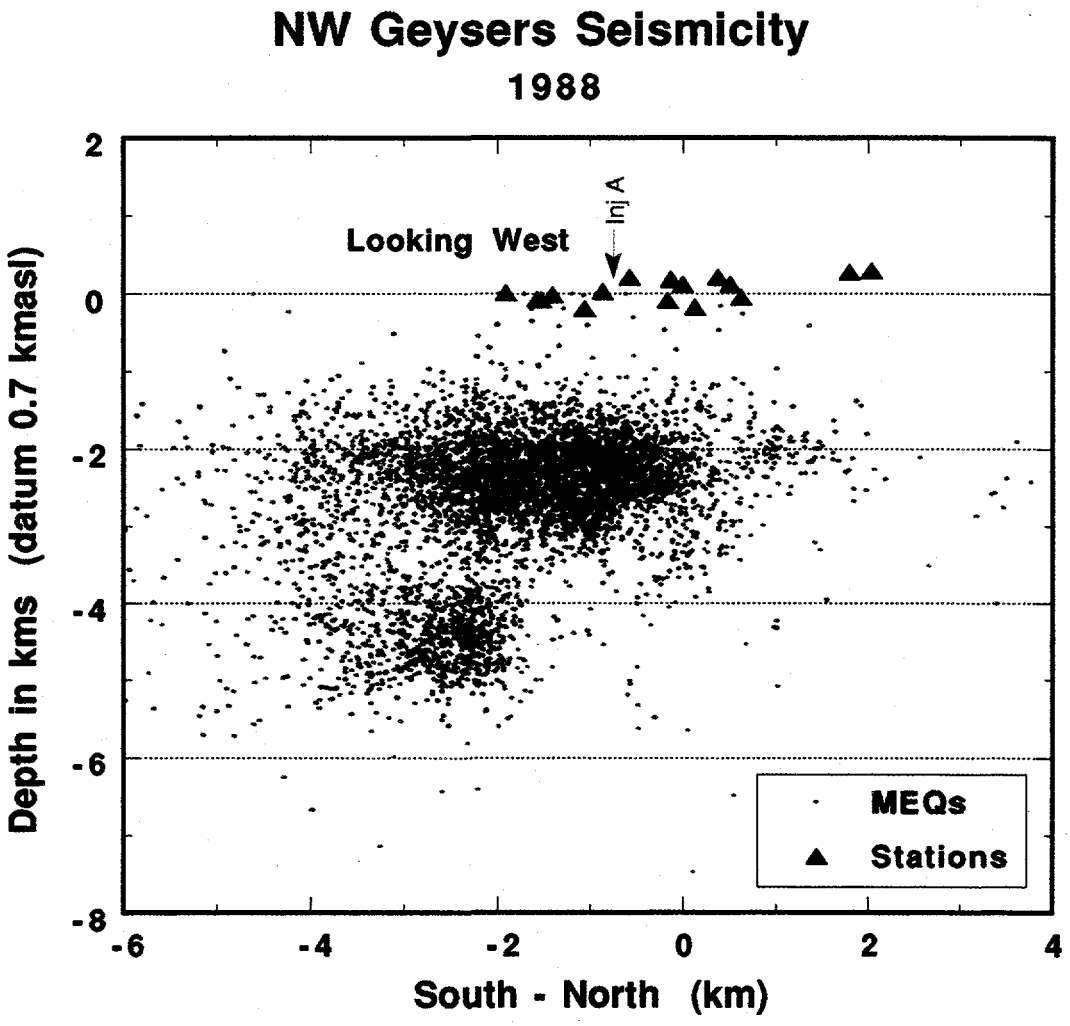
NW Geysers Seismicity
1988
Looking West
Inj A
MEQs
Stations
Depth in kms (datum 0.7 kmasl)
South - North (km)
2
0
-2
-4
-6
-8
-6
-4
-2
0
2
4

Figure 3.6c

Figure 3.7 Seismicity around Injector A. A) Map view showing the locations of microearthquakes around injector A. (B) West-east cross section across the region. (C) North-south cross section. The microearthquake distribution seems to define a vertical planar structure striking roughly north-south. Datum plane is 0.7 kmasl.

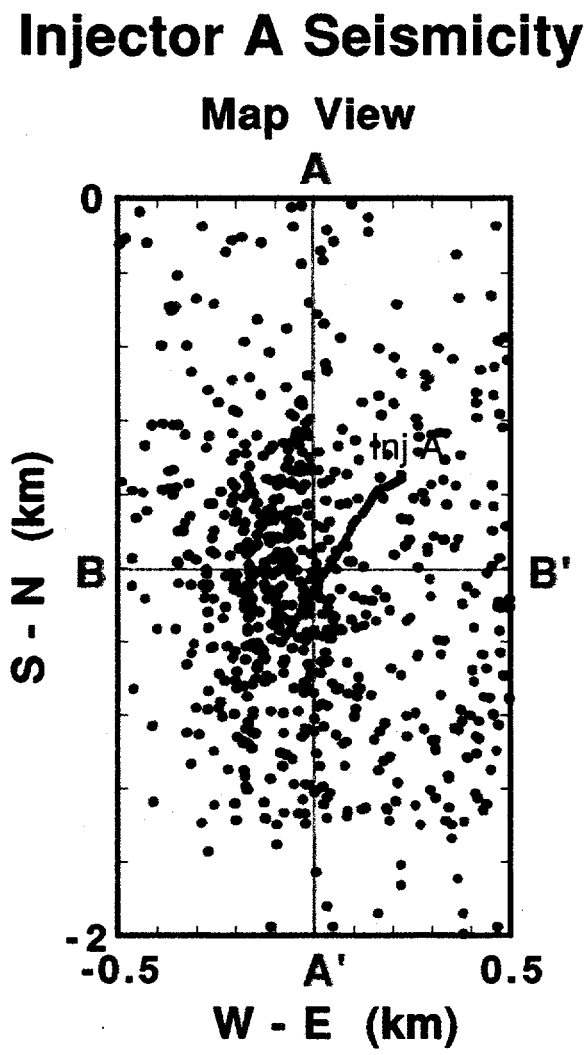

Figure 3.7a

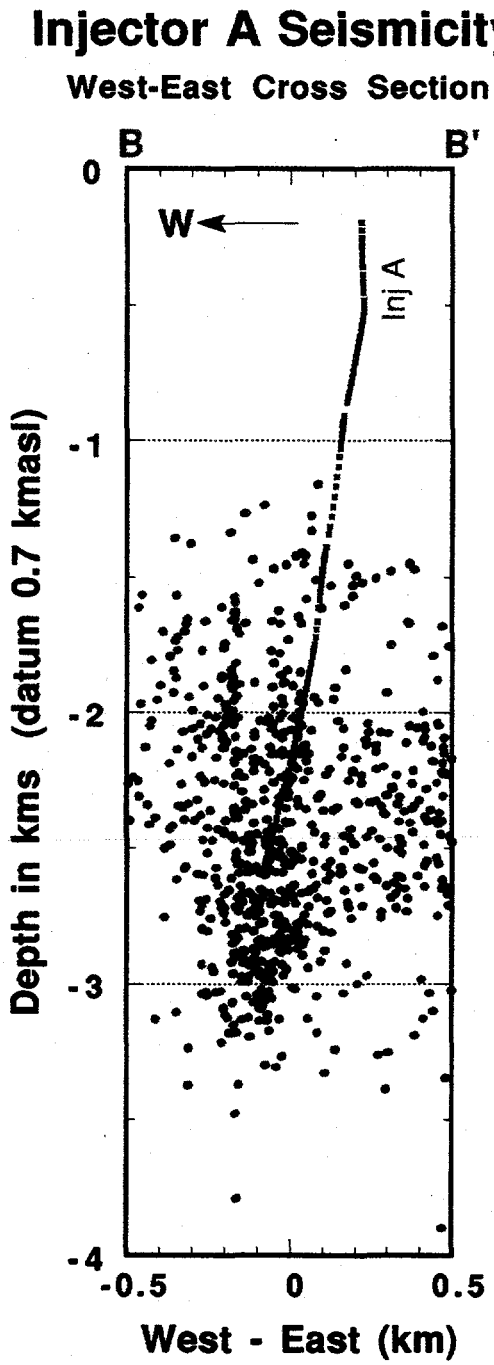
Injector A Seismicity
West-East Cross Section
B
B'
0
-1
-2
-3
-4
W
Inj A
Depth in kms (datum 0.7 kmasl)
-0.5
0
0.5
West - East (km)

Figure 3.7b

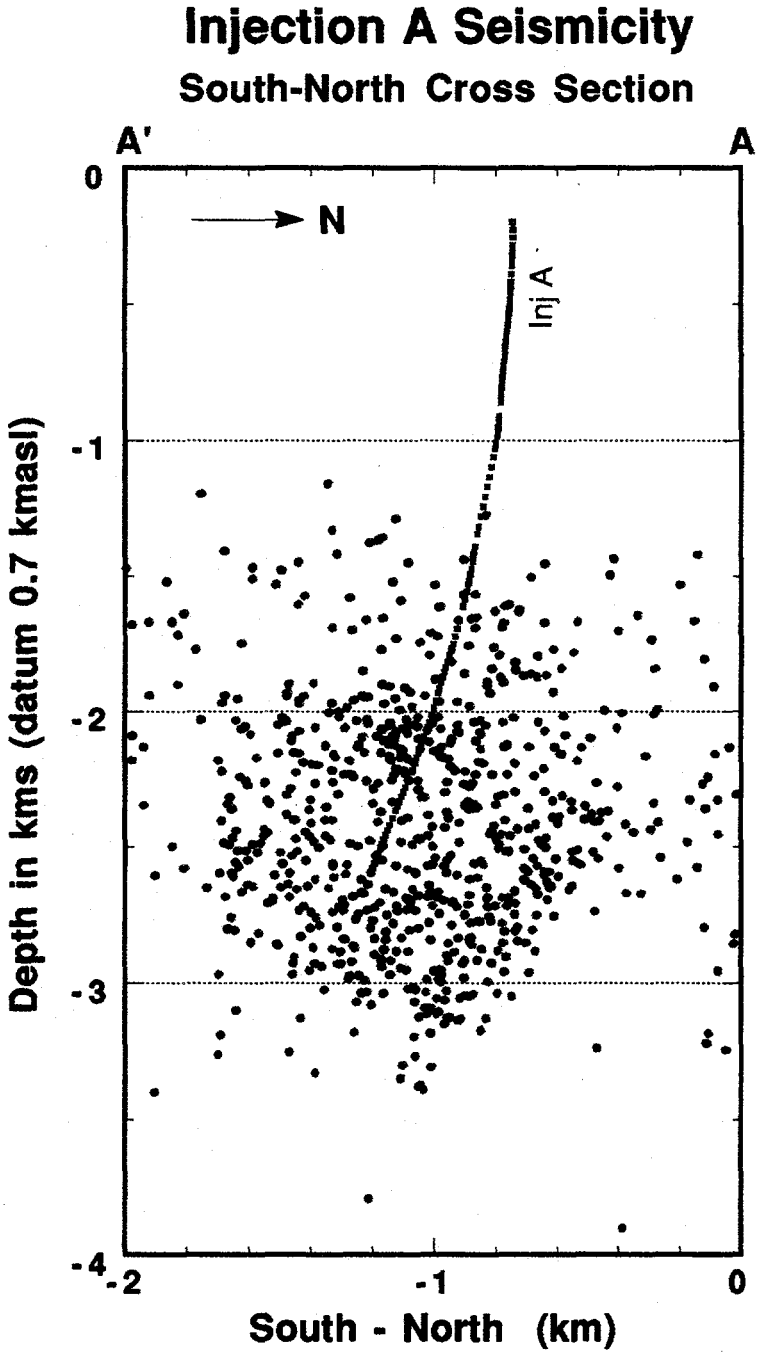
Injection A Seismicity
South-North Cross Section
A'
A
N
Inj A
0
-1
-2
-3
-4
-2
-1
0
Depth in kms (datum 0.7 kmasl)
South - North (km)

Figure 3.7c

Figure 3.8 Comparison between the seismicity rate within the CCPA steam field and the field-wide steam production rate. Seismicity more than doubled with the start of sustained production.

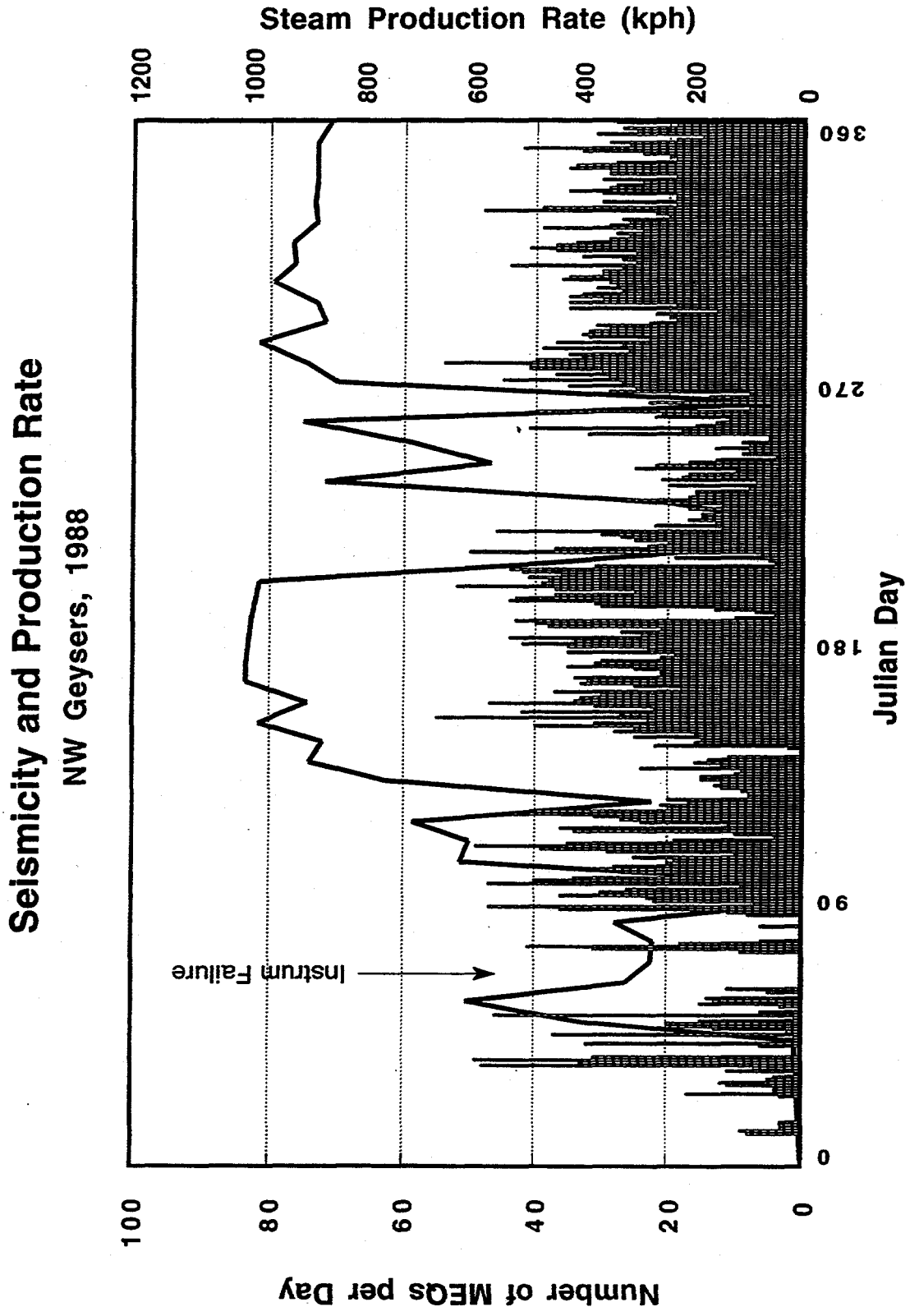
Seismicity and Production Rate
NW Geysers, 1988
Steam Production Rate (kph)
1200
1000
800
600
400
200
0
Number of MEQs per Day
100
80
60
40
20
0
Julian Day
360
270
180
90
0
Instrum Failure

Figure 3.8

Figure 3.9 Comparison between injector A's injection history and seismicity rate nearby. Note the good correlation between peaks in seismic activity and injection rate.

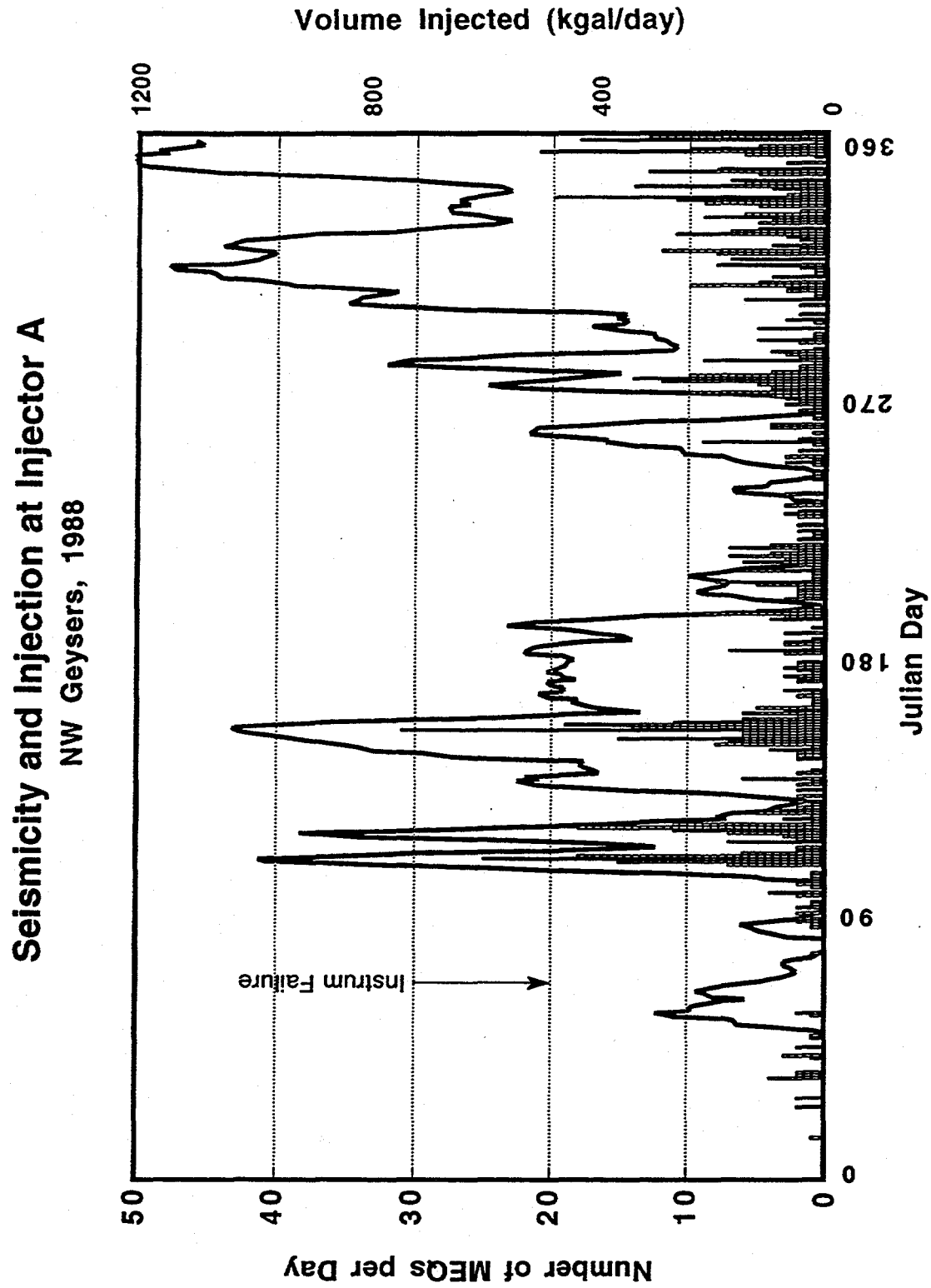
Volume Injected (kgal/day)
1200
800
400
0
Seismicity and Injection at Injector A
NW Geysers, 1988
Instrum Failure
360
270
180
90
0
Julian Day
50
40
30
20
10
0
Number of MEQs per Day

Figure 3.9

northeast to north-south (Zoback et al., 1987), assuming that the events were caused by hydraulic fracturing. On the other hand, siesmicity around the rest of the field exhibit no preferred orientation, lending support to the fact that production-related seismicity may be caused by a number of inducing-mechanisms.

In terms of temporal correlation, Figure 3.8 presents a comparison between the seismicity rate within the CCPA area and the field-wide steam production rate. Beginning at Julian day 90, 1988, seismicity increased significantly to approximately 20 events per day, more than double the pre-production seismicity rate. High seismicity was sustained during the course of steam production except during a short lull between Julian days 225 and 270 when production rate decreased temporarily. Figure 3.9 presents a comparison between injector A's injection history and seismicity rate nearby. Note the good correlation between peaks in seismic activity and injection rate. Seismicity increased with the start of sustained injection, and peaks in seismicity occurred during periods of maximum injection.

3.3.2 Velocity Structure

The resulting P-wave velocity (Vp) and S-wave velocity (Vs) from the inversion are presented in Figures 3.10 and 3.11. Shading of the figures indicate velocity deviations from the average 1-D model. This model, whose velocities are presented in Table 1, is obtained by taking the average of the velocity values over each of the five depth inversion layers (Depths are referenced to a datum plane 0.7 kmasl). The Vp/Vs structure is shown in Figure 3.12. Horizontal slices at four depths through the 3-D velocity volume are presented for each case. The cross sections display a 5 x 5 km^2 area centered at the CCSF. It should be mentioned that the resolution worsens with depth and also towards the edges of the CCSF (see Figures 3.4a and 3.4b). Therefore anomalies that are located in these border regions are given less weight and considered

Table 1. Average 1-D Velocity Model

Depth (km)	Vp (km/s)	Vs (km/s)	Vp/Vs
0	3.105	1.765	1.759
1	4.106	2.371	1.732
2	4.795	2.776	1.727
3	5.492	3.188	1.723
4	5.604	3.248	1.725

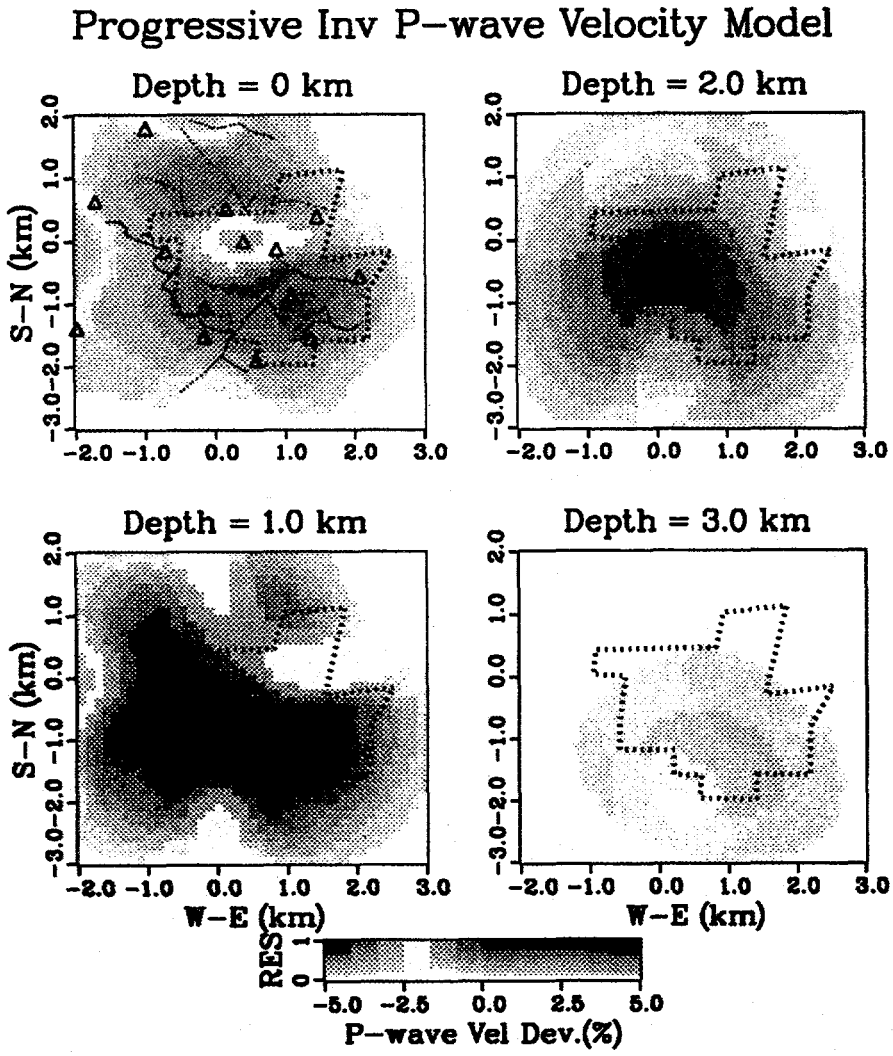

Figure 3.10 Final P-wave velocity model presented as deviations from an average 1-D model (Table 1). Colors denote velocity variations while intensity shows model resolution as shown in Figure 3.4a. The horizontal cross sections taken at four depths are centered on the CCSF. Datum plane is at 0.7 kmasl. Fault traces are shown in the top layer while triangles mark station locations. CCSF outline is shown for reference.

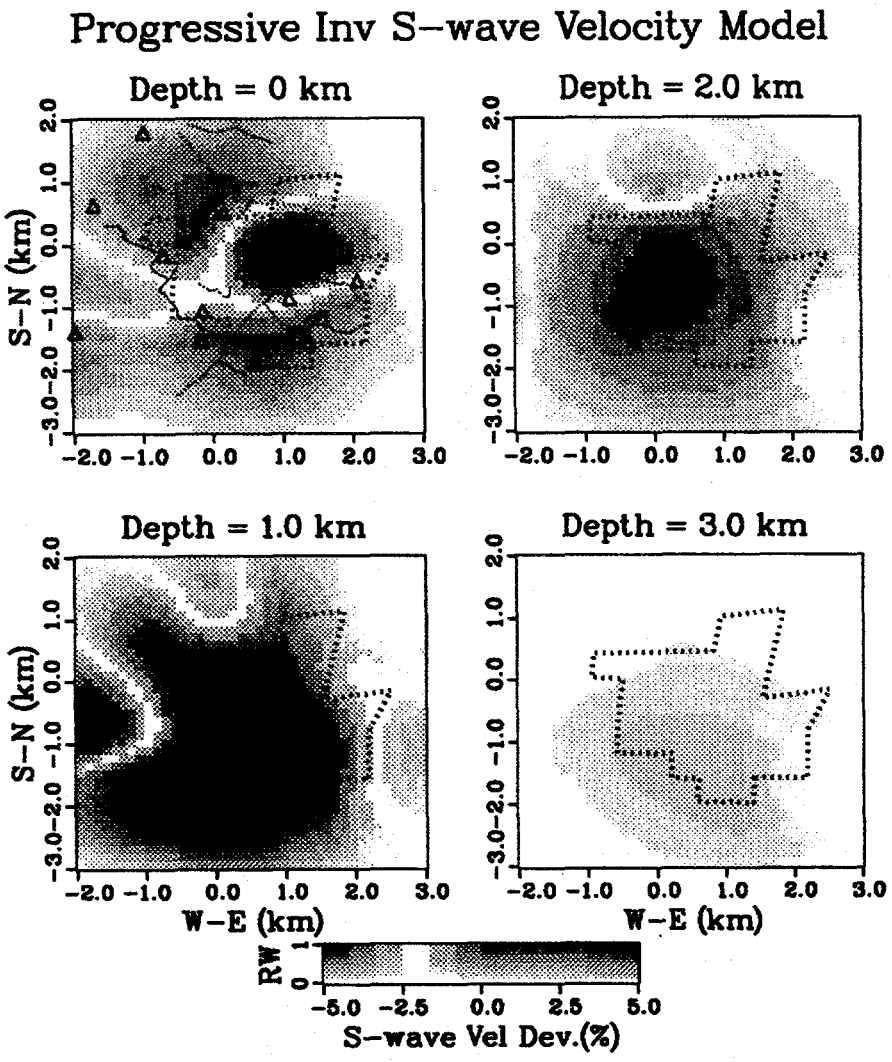

Figure 3.11 Final S-wave velocity model presented as deviations from an average 1-D model (Table 1). Colors denote velocity variations while intensity shows model resolution as shown in Figure 3.4b. See Figure 3.10 caption.

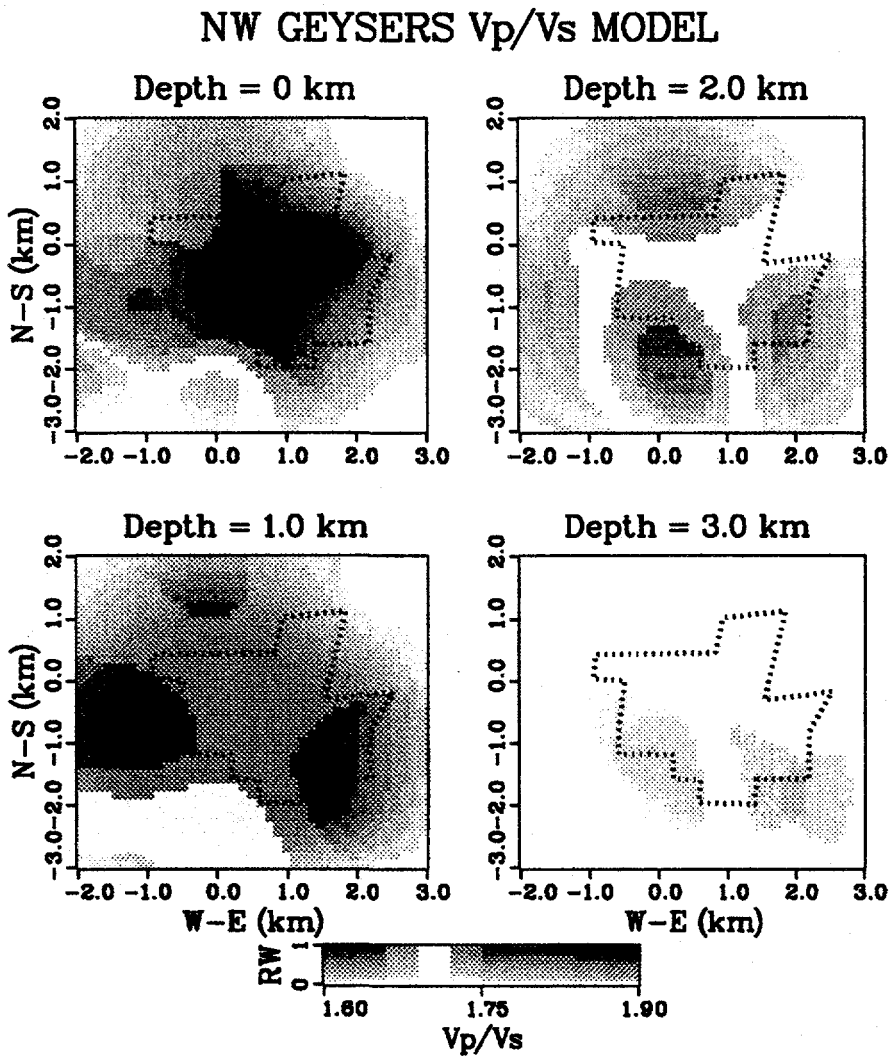

Figure 3.12 Final Vp/Vs model. Colors denote Vp/Vs variations while intensity shows model resolution as shown in Figure 3.4b. See Figure 3.10 caption.

artifacts of the inversion process.

The P-wave velocity structure (Figure 3.10) contains significant lateral variations in the upper 2 km, presumably due to the complex geology of the region. A prominent high Vp anomaly (+5%) is evident at the southeastern edge of the CCSF to a depth of 1 km. Lower velocities (-3%) characterize the central part of the CCSF at shallow levels that shift to the north with depth. The anomalies also exhibit some correlation with topographic elevation. For example, near-surface high-velocity anomalies (+4%) correspond to the ridge line at the northern edge of the CCSF while a narrow low-velocity anomaly (-5%) west of the field is parallel to Squaw Creek (Figure 3.2). Finally, a diffuse low-velocity region (+3%) is seen at the southern edge of the field at a depth of 1 km depth and becoming more extensive with depth.

The Vs structure (Figure 3.11) exhibits the general features of the Vp model but with more lateral variability. The near-surface seems to be characterized by a low-velocity band that crosses the central part of the CCSF and parallel to Squaw Creek. Where resolution is adequate, the region beneath the CCSF is characterized by high Vs anomalies (+3 to +5%) down to a depth of 3 km, except for a low-velocity anomaly (-3%) near the western border of the CCSF at a depth of about 1 km.

The Vp/Vs structure in Figure 3.12 displays high values (1.8) near-surface at the central and western parts of the CCSF. Although less well-resolved, two isolated high Vp/Vs anomalies (1.8) are located at the eastern and western margins of the CCSF at a depth of 1 km. Low Vp/Vs (1.6) also characterize the southern and central regions of the CCSF at 1 km depth. This feature extends northward at 2 km depth. The extent of this low Vp/Vs region below 3 km depth is unknown due to poor resolution.

3.4 Discussion

3.4.1 Seismicity

Several previous studies have inferred that the high seismicity in The Geysers region is related to geothermal development. Eberhart-Phillips and Oppenheimer (1984) concluded that it is related to steam production, and Stark (1990) documented a clear correlation between seismicity and injection. Results of this study indicate that seismicity is related to both production and injection activities. The seismicity zone between depths of 1.5 and 2.5 km present throughout most of the CCSF field (Figure 3.6) is presumably related to production of the steam reservoir. This seismicity zone deepens to the north, consistent with a greater depth to the top of the steam reservoir in that direction. The extent of seismicity probably maps the region that is hydraulically affected by both steam withdrawal and injection. Possible mechanisms put forward for the cause of this seismicity include volumetric contraction and collapse of overburden in response to continued steam withdrawal (Majer and McEvilly, 1979), conversion of aseismic creep to stick-slip behavior due to either an increase in the effective rock pressure or an increase in frictional coefficient due to clay dehydration and silica precipitation (Allis, 1982; Denlinger and Bufe, 1982). The deeper microearthquake clusters are probably related to long-term injection . Very few microearthquakes are deeper than 3 km, suggesting a near-ductile state of the rocks because of the high temperatures (>300°C) at these depths. However, injectate may cool the surrounding rocks sufficiently to induce brittle behavior, and this may explain the deep cluster of seismicity beneath injection wells. Nielson (1989) suggested that thermal variations are the dominant cause of stress variation within geothermal systems. Injection fluids may also locally increase the pore pressure thereby decreasing the normal stress and promoting shear failure (Kisslinger, 1976). Pressure data from injector A suggest that

injection does have an effect on the saturation of the formation as fluid invades the zones around the well (Pers Comm., M. Walters, Russian River Energy Corp.).

3.4.2 Station Delays

The station delays are tabulated in Table 2 together with the general lithology observed in the seismometer boreholes. The station delays show little correlation with near-surface velocity anomalies. However, the P-wave delays exhibit some correlation with elevation, as shown in Figure 3.13. The line shows the approximate linear relationship between P-wave station delay and elevation (The regression coefficient is 0.85 and is linear at the 95% confidence level.). Except for stations 6 and 16, stations below the datum plane have positive delays, while those above have negative delays. The abnormal negative delays at Stations 6 and 16 may be attributed to local geology as both are situated on higher-grade metagraywacke units. The positive delays at Station 11 may be due to an underlying layer of low-velocity Franciscan melange consisting of clay, chert and greenstone. S-wave delays also show some correlation with elevation, as shown in Figure 3.13, but the correlation is weaker than for the P-wave delays.

3.4.3 Lithological Interpretation of Velocities

A number of laboratory studies on seismic velocities have demonstrated that velocity variations do not necessarily reflect mineralogical variations (Stewart and Peselnick, 1977, 1978; Lin and Wang, 1980). Seismic velocities are also influenced by parameters such as porosity, fractures, degree of fluid saturation, and pore pressure. Therefore, lithologic inferences based on seismic velocity data must be made with caution. At the Northwest Geysers, the subsurface geology consists mainly of interbedded metagraywacke, metasiltstone and argillite partially overlain by relatively thin layers of

Table 2. Station Delays

Station	Elevation (m)	P delay (s)	S delay (s)	Lithology
1	722	0.01	0.005	chert
2	877	-0.01	-0.015	metagraywacke
3	814	0.00	0.015	greenstone
4	502	0.03	-0.010	metagraywacke
5	615	0.02	0.020	chert
6	705	-0.01	-0.025	metagraywacke
7	627	0.02	-0.010	metagraywacke
8	902	-0.01	-0.020	metagraywacke
9	906	-0.01	0.020	basalt
10	816	0.00	-0.020	metagraywacke
11	610	0.05	0.055	greenstone
12	684	0.00	-0.040	greenstone
13	525	0.03	0.020	metagraywacke
14	649	0.02	0.005	metagraywacke
15	969	-0.01	-0.010	metagraywacke
16	985	-0.05	-0.040	schistose meta-graywacke

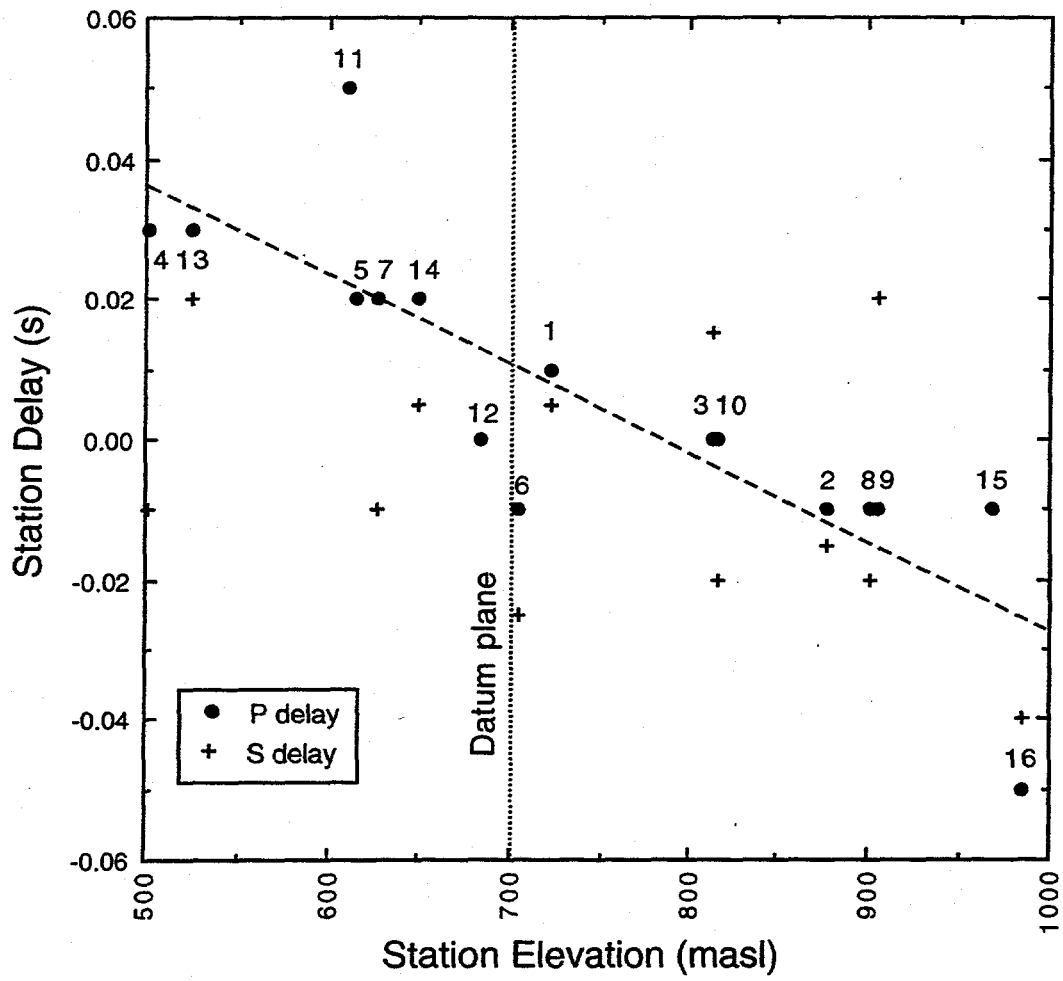

Figure 3.13 Station delay times for P- and S-waves versus station elevations. Stations are identified by numbers (locations shown in Figure 3.3). Datum plane is shown for reference. The dashed line depicts the approximate linear relationship between P-wave station delay and elevation. Regression coefficient is 0.85 and is linear at the 95% confidence level.

Franciscan melange and greenstone units (Sternfeld, 1989).

In Figure 3.14, the average 1-D velocities derived from the inversion were compared with the laboratory-measured velocities of representative graywacke and metagraywacke samples obtained from Stewart and Peselnick (1977); and Lin and Wang (1980). The samples (all from California) include W2, an unmetamorphosed graywacke obtained from western Mendocino County; GW1, SR70 and SP740 low- to medium-grade metagraywacke, obtained from Marin County; and GW5, a highly-metamorphosed jadeitic metagraywacke obtained from Pacheco Pass in the Diablo Range. The laboratory velocity values were corrected for lithostatic pressure and temperature effects based on the average geothermal gradient at the Northwest Geysers (Walters and Combs, 1992; Williams et al., 1993, Mark Walters, pers. comm. 1993).

The resulting seismic velocities from the CCSF are within the range of laboratory velocities for graywacke and low-grade metagraywacke between depths of 1.5 and 2.5 km and approach high-grade metagraywacke velocities at depths greater than 2.5 km. This observation is supported by geologic studies of Walters et al. (1988) and Sternfeld (1989) at the Northwest Geysers which describe the thermal alteration of the metagraywacke as hornfelsic starting at about 2.5 km depth. Above 1.5 km depth, the 1-D velocities are less than the laboratory values for graywacke, perhaps reflecting the different lithology overlying the metagraywacke (e.g. melange units). Alternatively, the lower velocities may be due to higher porosities and weathering at shallow depths.

The observed velocity model (Figures 3.10, 3.11 and 3.12) correlates well with mapped surface geology (Nielson et al., 1991; CCPA unpublished geologic maps). High velocities to the north and southeast of the CCSF appear to be associated with greenstone and metagraywacke units (refer to Figure 3.2). In particular, the prominent high velocity southeast of the CCSF is coincident with the only substantial metagraywacke exposure. On the other hand, low velocities at the center of the CCSF at shallow depths seem to be related to a Franciscan melange unit and to the surficial

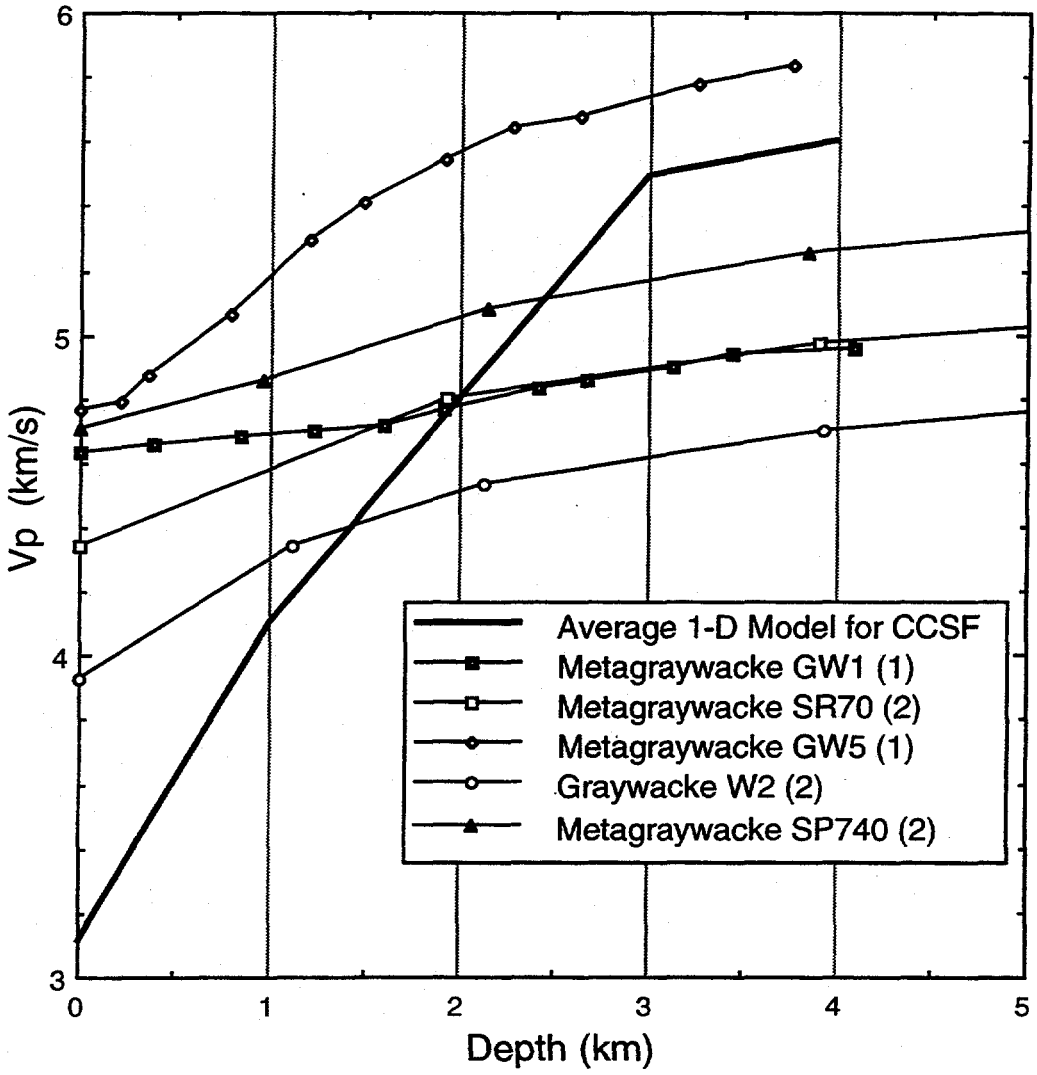

Figure 3.14 Graph of the average 1-D, P-wave velocity profile for the CCSF derived from the inversion. Measured velocities of representative graywacke and metagraywacke samples obtained from (1) Lin and Wang (1980), and (2) Stewart and Peselnick (1977) are plotted for comparison.

Pleistocene basalt flows at Caldwell Pines. Walters (pers. comm. 1993) described these basalts, which have lower densities than the indurated graywacke, as brecciated with poorly-consolidated volcanic lapilli components. The melange unit is offset by shears and shallow-dipping thrust faults that were subsequently displaced by high-angle normal and strike-slip faults (Nielson et al., 1991).

One northeast-striking fault known as the Caldwell Pines fault (Figure 3.2) seems to define the northwest boundary of the prominent high velocity region located southeast of the CCSF. Lower velocities at 1 km depth to the north of the CCSF may indicate the melange units dipping to the northeast, following the general structure of the region. Low Vp anomalies underlie the southern region between depths of 1 and 3 km with evidence of extending deeper even as resolution is lost. This decrease in velocity may be explained by high rock temperatures and the presence of gases within an underlying high-temperature reservoir (HTR) described by Walters et al. (1988). The HTR is characterized by higher steam enthalpies, gas concentrations, and reservoir temperatures compared to the overlying "normal" Geysers reservoir. The HTR is in hornfelsic-metagraywacke host rocks, the hornfels being indicative of a deeper felsite. Walters et al. (1988) postulated that the HTR is a transient phenomenon resulting from the geologically-recent venting of a liquid-dominated system transforming the reservoir to a vapor-dominated one which has not sufficiently cooled down. Heat transfer within the HTR is probably dominated by conduction in contrast to the convectional heat transport within the typical reservoir.

Truesdell et al. (1993), integrating current geological, geochemical and reservoir engineering data, have proposed a conceptual model for the origin of the whole Geysers geothermal system. They postulate that The Geysers field is tapping heat from a relatively young (0.1 Ma or younger) igneous intrusion near the Northwest Geysers based on several lines of evidence: high heat flow, an HTR containing high non-condensible gas content and magmatic gasses. The different reservoir characteristics at

the Northwest Geysers are attributed to lower recharge and heat loss rates, and less venting compared to the rest of The Geysers.

No seismic evidence for the felsite body or young intrusives was found, probably because of lower resolution at depth. The predominantly shallow microearthquake focal depths in the Northwest Geysers does not provide enough ray coverage to image the regions deeper than 3 km beneath the CCSF. In this field, no wells have encountered the felsite to 3 km, however, in this region it is postulated to be around 3.5 km depth based on thermal metamorphism of the hornfelsic graywacke (Sternfeld, 1989).

3.4.4 Vp/Vs and the Geothermal Reservoir

The Vp/Vs structure in Figure 3.12 displays features relating to the geothermal reservoir. Liquid in fractures increase the specific stiffness to compressional waves, but do not inhibit the relative shear displacement across the joints. As a result, higher liquid saturation increases the effective Vp/Vs ratio while partial saturation (dry or gas-filled fractures) depresses it (Toksöz et al., 1976; Gregory, 1976). Moos and Zoback (1983) also found that the presence of fully-saturated fractures decreases both P and S-wave velocities, and increases Vp/Vs. High Vp/Vs values characterize the central and western regions of the CCSF near the surface. The high Vp/Vs anomaly is most prominent near the Caldwell Pines basalt flows and near the confluence of Wildhorse and Squaw Creeks west of the CCSF (Figure 3.2). The Caldwell Pines basalt supports a small ground water unit, evidenced by springs which emerge at its base. This anomaly probably indicates liquid-saturated regions that are confined to the near surface. Isolated high Vp/Vs anomalies extend to a depth of 1 km at the western and eastern edge of the CCSF. These regions were interpreted as zones affected by surface recharge. The eastern anomaly also coincides with the region where the metagraywacke outcrops.

McNitt et al. (1989), using geologic data, suggested that recharge may come through these outcrops. This high Vp/Vs zone may also indicate a condensation zone above the producing horizon, as previously reported by O'Connell and Johnson (1991) and supported by CCPA's drilling data in the Northwest Geysers. Sternfeld (1989), summarizing the characteristics of wells drilled in that area, described water and saturated steam at the shallowest fluid entries.

Low Vp/Vs values occur between 1 and 3 km depth suggesting partial saturation of the reservoir rocks. Most steam entries in the wells lie within the low Vp/Vs region. There is also a good agreement between the first steam entries and the top of the low Vp/Vs anomaly. This low is interpreted to delineate the steam reservoir, underlying most of the CCSF at 2 km depth and which seems to trend northwest parallel to the regional structure. The vertical extent of the low Vp/Vs region is unknown because of poor resolution below 3 km. O'Connell and Johnson (1991) also found low Vp/Vs values within the production zone. Lastly, no seismic distinction was found between the HTR and the normal reservoir. Walters et al. (1988) suggested that the two reservoirs are in hydraulic contact as evidenced by pressure continuity and their boundary is mainly thermodynamic in nature.

3.5 Conclusions

The results of the study suggest that the velocity structure and the seismicity pattern in the CCSF are related to geothermal activity. Velocity variations correlate with the known geology and hydrology of the reservoir. Near-surface high-velocity anomalies correspond to mapped sections of Franciscan metagraywacke and greenstone while low-velocity anomalies are associated with Franciscan melange and poorly-consolidated basalt flows near the Caldwell Pines. High Vp/Vs values near-surface may

indicate liquid-saturated regions affected by meteoric recharge. A high Vp/Vs anomaly found east of the CCSF at a depth of 1 km suggests a zone influenced by surface recharge or a condensation zone above the reservoir. A low Vp/Vs anomaly delineates the steam production zone between 1 and 3 km depth, suggesting partial liquid saturation of the reservoir rocks. The estimated P-wave station delays correlate with elevation and exhibit some relationship with local geology. Spatial and temporal patterns of seismicity exhibit compelling correlation with geothermal exploitation. A cluster of microearthquakes with focal depths between 2 and 3 km is located beneath an injection well in the central part of the CCSF. This seismicity is superimposed on a more general pattern related to natural seismicity and effects of steam withdrawal. Presently, CCSF has a well-characterized velocity structure and seismicity patterns to serve as the baseline for subsequent monitoring.

Chapter 4

THREE-DIMENSIONAL P- AND S-WAVE ATTENUATION TOMOGRAPHY AT THE NORTHWEST GEYSERS GEOTHERMAL REGION, CALIFORNIA

4.1 Introduction

During the last decade, natural-event tomographic techniques have been applied in seismically-active regions to image the three-dimensional attenuation structure. In volcanic regions, they have been used to image partial melts and help delineate magma bodies (Clawson et al, 1989; Scherbaum and Wyss, 1990; Evans and Zucca, 1988, Ponko and Sanders, 1994). More recently, attenuation tomography has been used to image the complex fault geometry (Lees and Lindley, 1994), and to help delineate the steam reservoir in geothermal areas (Zucca et al, 1994). Coupled with seismic velocity, attenuation provides added independent complementary information on the mechanical properties of rocks and fluids at depth. In this study, the high-resolution microearthquake data from the seismic network in the NW Geysers geothermal region is exploited to construct a detailed 3-D attenuation structure of the shallow (< 4 km) crust to develop an image of the existing reservoir.

4.2 Background

The Geysers is a dry-steam geothermal field situated within the central Franciscan assemblage belt of the northern California Coast Ranges. The steam reservoir lies within a fractured metagraywacke, and is overlain by either Franciscan

greenstone melanges or unfractured metagraywacke in steeply dipping thrust packets that constitute the cap rock (Thompson, 1992). A location map and simplified surface geology of the NW Geysers region is shown in Figure 4.1. A more detailed description of the geology and the existing geothermal system in the NW Geysers is presented in chapter three.

Several inversion studies have developed velocity and attenuation models at The Geysers with the aim of delineating of the geothermal reservoir (Majer and McEvilly, 1979; Eberhart-Phillips, 1986; O'Connell and Johnson, 1991; Julian et al., 1993; Zucca et al., 1994). These studies variously interpreted the anomalies in terms of lithological variation, fault zones, and steam producing zones. The most consistent observation is that the steam zone, characterized by low Vp/Vs values, is overlain by a zone of relatively higher Vp/Vs which was interpreted as a condensation zone or zone affected by meteoric recharge. The two attenuation studies by Majer and McEvilly (1979) and Zucca et al. (1994) found high P-wave attenuation within the steam-producing zone compared to the surrounding rocks. The high attenuation and low Vp/Vs attest to the vapor-dominated nature of the reservoir.

4.3 Data and Methodology

The data for this study consist of P-wave and S-wave amplitude spectra obtained from a 16-station, digital, three-component, high-frequency (400 samples/sec/channel) network in place at the NW Geysers. The seismometers are about 30 m below the surface in boreholes . From approximately 5000 microearthquakes recorded in 1988, for the inversion about 480 events were selected, distinguished by high signal-to-noise ratio (>20) and having a minimum of 10 impulsive P-wave arrivals. The station distribution, inversion nodes, and the epicenters used in the inversion are shown in

Figure 4.1 Location map of The Geysers geothermal field (from Thompson, 1992) and a simplified surface geologic map of the Northwest Geysers region (adapted from Nielson et al., 1991). Heavy lines represent mapped faults and major geologic contacts in the area (Adapted from field mapping by M. Walters). The Coldwater Creek Steam Field (CCSF) is shown for reference. Small squares mark power plant locations.

The Geysers
California
The Geysers Geothermal field
Collayami Fault
Power Plants
CCSF
Big Sulphur Creek Fault
Mercuryville Fault
Maacama Fault
0 1 2 3 km
38° 50'
38° 45'
122° 50'
122° 40'
NW Geysers
CCSF
Caldwell Pines
Squaw Creek Fault Zone
Wildhorse Creek
Squaw Creek
Caldwell Pines
fgs
fgw
fm
Qtb
South - North (km)
West - East (km)
2.0
1.0
0.0
-1.0
-2.0
-3.0
3.0
Legend
fm Franciscan melange
fgs Franciscan greenstone
fgw Franciscan metagraywacke
Qtb Basalt of Caldwell Pines

Figure 4.1

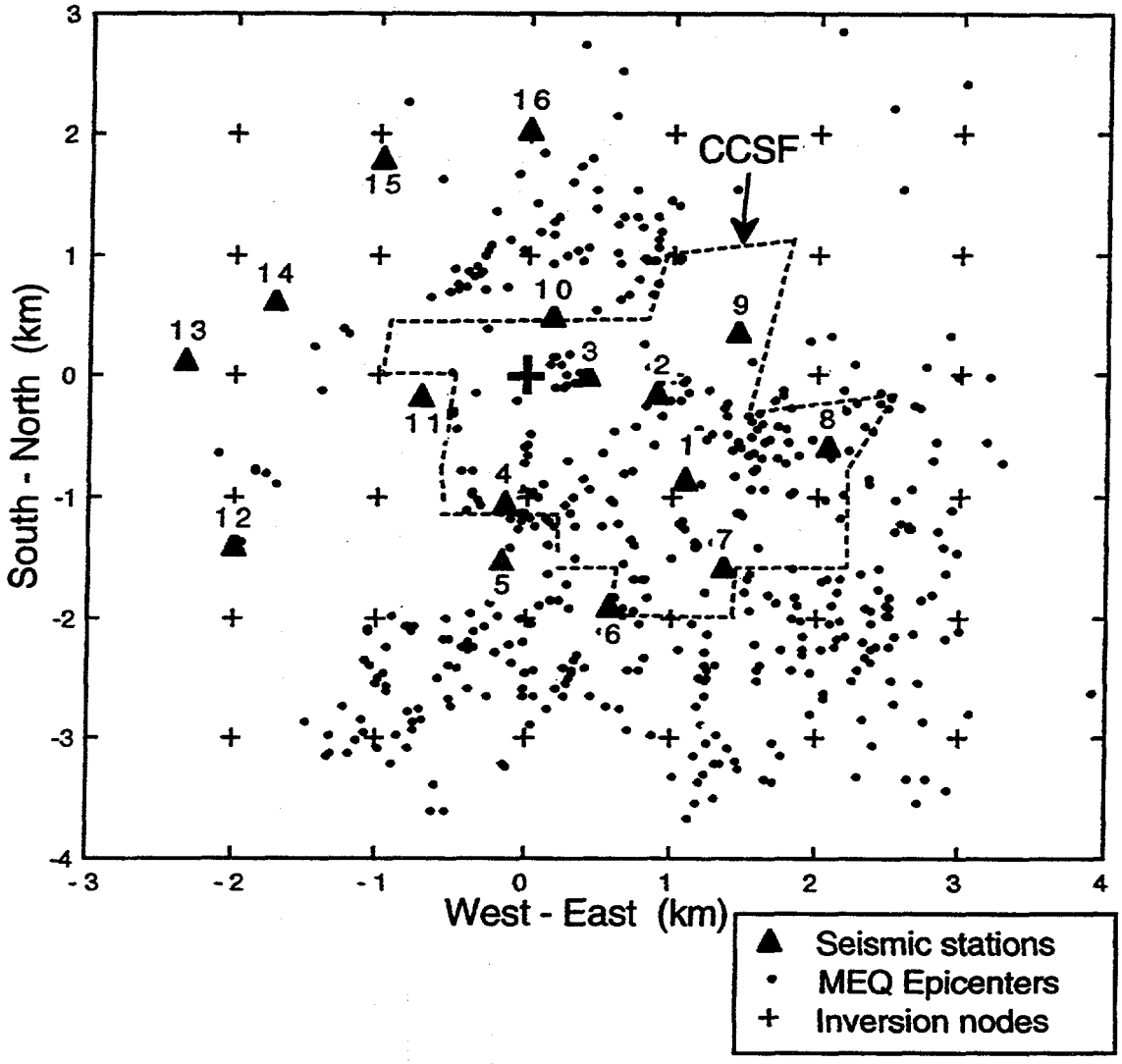

Figure 4.2 Map showing the station locations (triangles), inversion nodes (small crosses) and the epicenters of the 480 microearthquakes (small dots) used in the inversion. The origin of the local coordinates is centered at 38°50.55'N, 122°49.64'W (large cross). CCSF outline is given for reference.

Figure 4.2. The sharp P-wave arrivals make it possible to pick arrival times to an accuracy of one sample interval (2.5 ms). S-wave arrival times were picked only when they were unambiguous. Those that differ by more than 10 ms between the two horizontal components were discarded. These sources for the data set were well-distributed within the region of interest to achieve uniformly dense ray coverage. The raypaths, hypocenters and the 3-D velocity model used in this study were obtained from the velocity inversion discussed in Chapter 3.

The P- and S-wave amplitude spectra were computed using an FFT routine. There was concern on the effect of window length on the determination of the attenuation operator. Ideally, the window should be long enough to capture the energy of the impulsive main phase but exclude scattered and secondary arrivals. Because of the high digitizing rate, it was possible to use small window lengths and yet still have a sufficient number of spectral points to determine the ratios. The attenuation structure was solved with window lengths of 0.25 s, 0.5 s and 0.75 s. The results for 0.25 s and 0.5 s were very similar. Differences seen for 0.75 s windows were assumed to be due to contamination by secondary arrivals because most of the seismograms have S-P times of less than 1 s. A window length of 0.5 s was used in the final inversion. The natural frequency of the seismometer (4.5 Hz) and the anti-alias filter (100 Hz) define the usable bandwidth of the data. The pre-P-wave noise spectra was subtracted (assuming the noise is uncorrelated) to correct the amplitude spectra. The instrument response is canceled in the spectral ratio.

4.3.1 Spectral Ratio Technique

The use of local earthquake tomography in determining crustal attenuation has been used for many years (Sanders (1993) presents a concise review). The amplitude

spectrum observed at the *j*th station for the *i*th event is usually represented in the frequency domain as:

$$A_{ij}(f,r,\theta,\phi) = G_{ij}(r,\theta,\phi)S_i(f)I_j(f)L_j(f)\exp(-\pi f t_{ij}^*) \quad (1)$$

where the attenuation operator

$$t_{ij}^* = \int_{raypath} \frac{dr}{Q_{ij}(r)V_{ij}(r)} \quad . \quad (2)$$

$G_{ij}(r,\theta,\phi)$ is the geometrical spreading term; r is the distance along the raypath; θ,ϕ are the propagation direction with respect to the source; $S_i(f)$ is the source response; $I_j(f)$ is the instrument response; $L_j(f)$is the site response; $Q_{ij}(r)$ is the path attenuation factor; and $V_{ij}(r)$ is the three-dimensional velocity structure. Normally $S_i(f)$ is also a function of θ and ϕ due to source directivity, but it is assumed this effect to be negligible in the microearthquake range (Scherbaum, 1990). It is also assumed that $Q_{ij}(r)$ is independent of frequency over the bandwidth of interest. From (1) and (2), the path attenuation $Q_{ij}(r)$ is determined from measurements of A_{ij}.

The spectral ratio method involves the cancellation of several parameters by spectral division using a reference spectrum. Investigators have used several approaches for obtaining the reference spectrum. The reference spectrum may be taken from the spectrum of one receiver or from an average over several receivers for the same source. This latter approach will cancel the source contribution and isolate the path effects (assuming that the receivers have the same instrument response). The reference spectrum may also be obtained from a receiver outside the region of interest. This approach would yield differential attenuation between the other receivers and the reference site. Lastly, a reference spectrum taken from the average spectra of several earthquakes observed at one receiver could provide a site correction factor for that particular receiver. This last approach was adopted because of the severe site-

dependence observed in the spectra, as discussed below. Evans and Zucca (1988, 1992) also argued that a reference spectrum derived from an average of several spectra is more stable compared to one obtained from a single spectrum. Taking the natural logarithm of (1):

$$\ln A_{ij}(f,r,\theta,\phi) = \ln G_{ij}(r,\theta,\phi) + \ln S_i(f) + \ln I_j(f) + \ln L_j(f) - \pi f t^*_{ij}. \quad (3)$$

The site reference spectrum for the jth station is the average of all spectra observed at that station:

$$\overline{\ln A_j(f)} = \frac{1}{N}\sum_i^N \ln A_{ij}(f,r,\theta,\phi) \quad . \quad (4)$$

The spectral ratio of (3) and (4) is:

$$\Delta \ln A_{ij}(f) = A_{ij}(f) - \overline{\ln A_j(f)} \quad . \quad (5)$$

This ratio yields differences in the attenuation between the reference spectrum and all other spectra, removing common variables such as instrument and local site response and simplifying the problem to contributions from the source and the path only. It will be argued later that the source contribution is negligible, so that the ratios are assumed to reflect differential path attenuation effects only. Figures 4.3a and 4.3b illustrate the estimation of t* for a typical earthquake. Following Solomon and Toksöz (1970) and Ponko and Sanders (1994), (5) can be equated to an equation similar to (1) that explicitly contains a sum of a background t^* and a deviation from the background δt^* :

$$\Delta \ln A_{ij}(f) = \ln A^o_{ij} - \left[f\left(t^*_{ij} + \delta t^*_{ij}\right)\right] - \frac{1}{N}\sum_i^N \left\{\ln A^o_{ij} - \left[f\left(t^*_{ij} + \delta t^*_{ij}\right)\right]\right\} \quad (6)$$

Figure 4.3 Plot of the spectrum of a typical earthquake observed from one station, the reference spectrum for that station, the spectral ratio, and the estimated t* obtained from the slope of the ratio. Error bar is 1 σ. (A) P-wave. (B) S-wave.

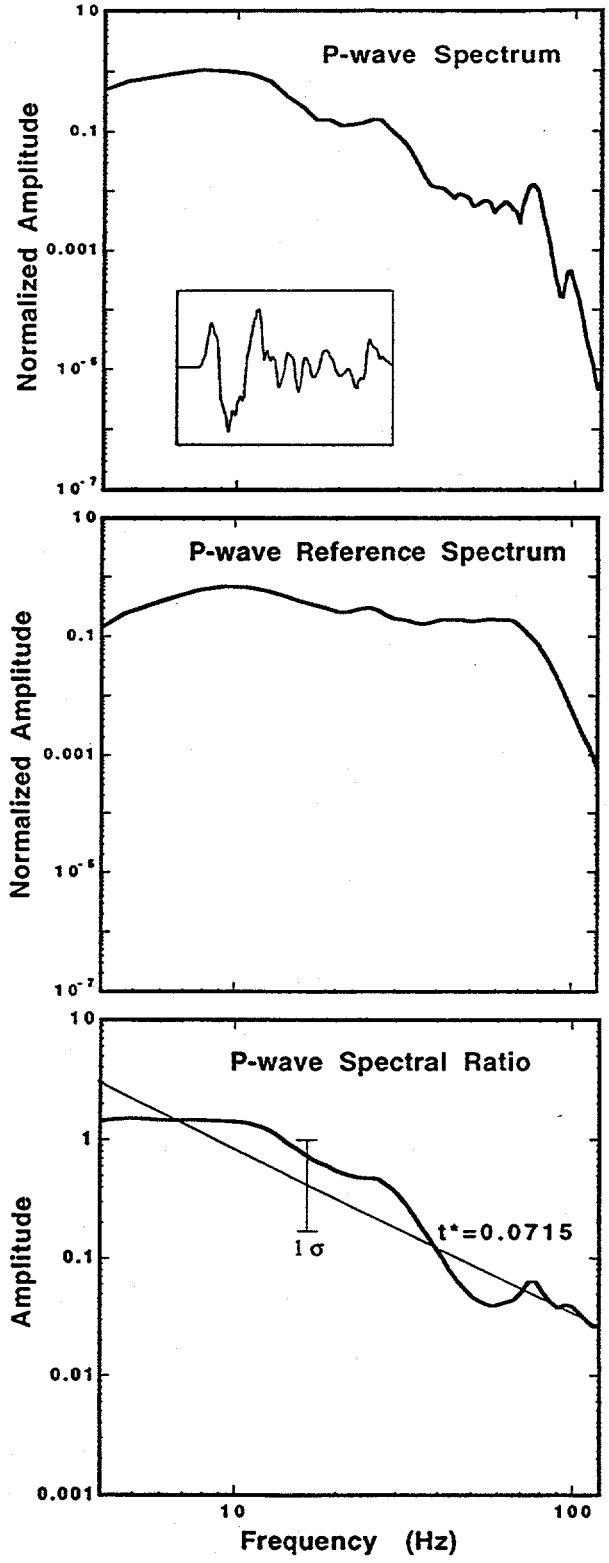
P-wave Spectrum
Normalized Amplitude
10
0.1
0.001
10⁻⁵
10⁻⁷
P-wave Reference Spectrum
Normalized Amplitude
10
0.1
0.001
10⁻⁵
10⁻⁷
P-wave Spectral Ratio
Amplitude
10
1
0.1
0.01
0.001
1 σ
t*=0.0715
10
100
Frequency (Hz)

Figure 4.3a

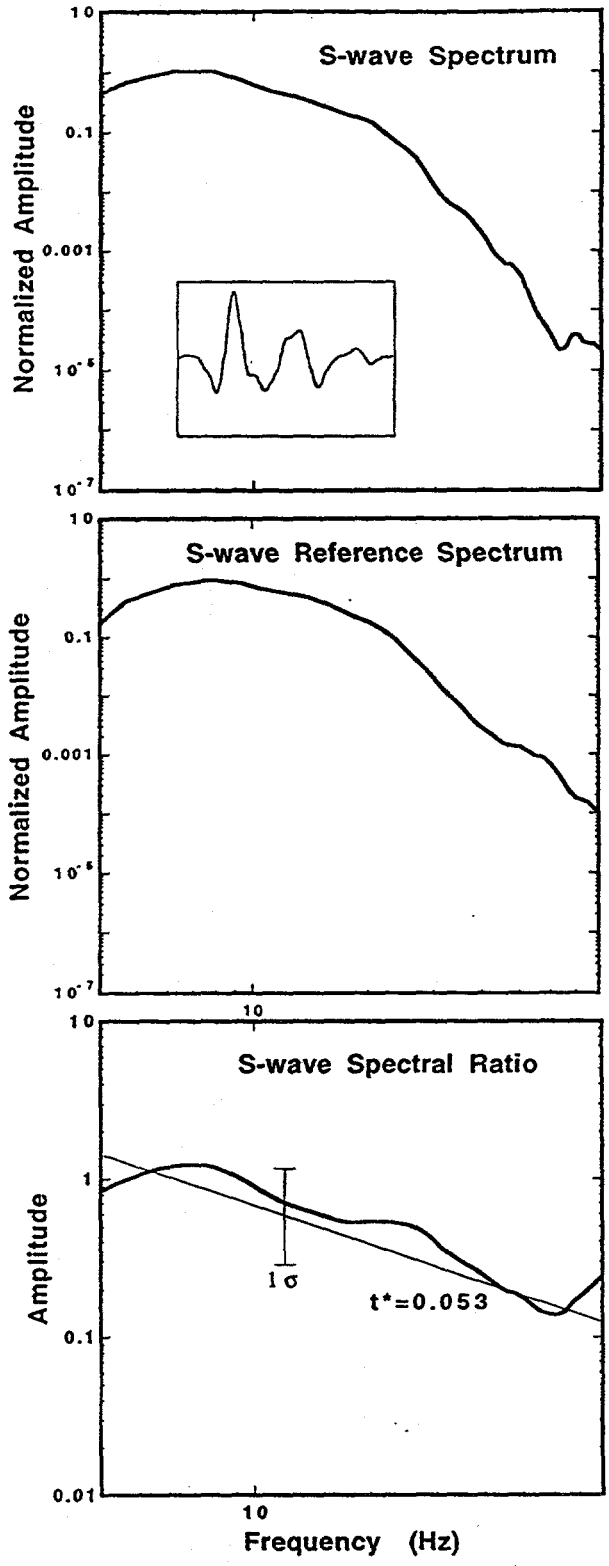
S-wave Spectrum
Normalized Amplitude
10
0.1
0.001
10⁻⁵
10⁻⁷
S-wave Reference Spectrum
Normalized Amplitude
10
0.1
0.001
10⁻⁵
10⁻⁷
10
S-wave Spectral Ratio
Amplitude
1
0.1
0.01
1σ
t*=0.053
10
Frequency (Hz)

Figure 4.3b

where

$$\delta t_{ij}^{*} = \pi \int_{raypath} \frac{dr}{\delta Q_{ij}(r) V_{ij}(r)} \quad . \tag{7}$$

Simplifying (6)

$$\Delta \ln A_{ij}(f) = B_o - f\left(t_{ij}^{*} + \delta t_{ij}^{*}\right) + f(\overline{t_j^{*}} + \overline{\delta t_j^{*}}) \tag{8}$$

where

$$\overline{t_j^{*}} = \frac{1}{N}\sum_{i}^{N} t_{ij}^{*} \tag{9}$$

$$\overline{\delta t_j^{*}} = \frac{1}{N}\sum_{i}^{N} \delta t_{ij}^{*} \tag{10}$$

$$B_o = \ln A_{ij}^{o} - \overline{\ln A_j^{o}} \quad . \tag{11}$$

B_o represents a constant that is not a function of frequency and therefor will not affect the attenuation calculation. It was assumed that the average differential attenuation $\overline{\delta t_j^{*}}$ to be equal to zero. Rearranging (8) gives

$$\Delta \ln A_{ij}(f) = B_o - f\left(t_{ij}^{*} - \overline{t_j^{*}}\right) - f\delta t_{ij}^{*} \quad . \tag{12}$$

Equation (12) is a linear equation relating the observed spectral ratio, $\Delta \ln A_{ij}(f)$, to the attenuation. The slope of (12), obtained through linear regression assuming $\left(t_{ij}^{*} - \overline{t_j^{*}}\right)$ is known, would then yield the differential attenuation, δt_{ij}^{*}, experienced by a raypath traveling from the ith event to the jth station. A linear regression method that uses the L1 norm instead of the more traditional L2 norm was used. This median method fits a line by minimizing the absolute deviation and is more robust than the least squares method because of its relative insensitivity to large but few outliers in the data (Press at al., 1989). The term $\left(t_{ij}^{*} - \overline{t_j^{*}}\right)$ is a correction factor that accounts for the difference in

attenuation suffered by any one raypath and the average attenuation experienced by all raypaths observed at the jth station. This term is computed from (2) and (9) using raypaths traced through a three-dimensional velocity model obtained in Chapter 3 and using background Q_p values from Zucca et al. (1994) and Majer and McEvilly (1979). Because of the absence of Q_s measurements at The Geysers, Q_s is assumed to be equal to Q_p. Several studies support this assumption, among them is the observation by Frankel (1982) that Q_p and Q_s are roughly proportional beneath the Caribbean and Taylor et al. (1986) found that near-surface Q_p is roughly equal to Q_s in North America.

The inversion for the differential attenuation structure was carried out using a modification of the progressive inversion scheme of Thurber (1983) with cubic spline interpolation (Michelini and McEvilly, 1991). The Thurber inversion method, which estimates the earthquake relocations and velocity variations by minimizing travel-time residuals, is applicable to the differential attenuation problem because of the direct analog between travel time and the attenuation operator t_{ij}^*. Travel times are calculated with an equation similar to (2) but without the Q factor. Theoretical δt_{ij}^* is calculated for each ray path using (7). The target region was divided into a 3-D rectangular grid with a grid spacing of 1 km (x 6 nodes) horizontally and 1 km (x5 nodes) vertically centered on the region of interest, and velocities were assigned to each grid point from the inversion results in chapter three. The differential attenuation factor, δQ^{-1}, was initially set to zero. Velocity and δQ^{-1} at any position is solved using the cubic spline interpolation:

$$V(x,y,z) = \sum_{i,j,k=1}^{M} \rho_{ijk}(x,y,z) a_{ijk} \tag{13}$$

$$\delta Q^{-1}(x,y,z) = \sum_{i,j,k=1}^{M} \rho_{ijk}(x,y,z) b_{ijk} \tag{14}$$

where $\rho_{ijk}(x,y,z)$ are the normalized cubic-spline basis functions; M is the number of

basis functions; a_{ijk} and b_{ijk} are the velocity and attenuation spline coefficients, respectively; *I, J, K* are the total number of velocity/attenuation model parameters along the three axes, *x, y,* and *z*, respectively. The residual *r* for each source-receiver pair, which is the difference between the theoretical δt^*_{cal} computed from (7) and the observed δt^*_{obs} based on spectral ratios , can be expressed to first order as :

$$r = \delta t^*_{obs} - \delta t^*_{cal} = \sum_{i,j,k=1}^{M} \frac{\partial \delta t^*}{\partial b_{ijk}} \Delta b_{ijk} + \varepsilon \qquad (15)$$

where Δb_{ijk} are the perturbations to the differential attenuation spline coefficients; $\frac{\partial \delta t^*}{\partial b_{ijk}}$ are the partial derivatives of the differential δt^* with respect to the differential attenuation spline coefficients b_{ijk}; ε is the residual error. $\frac{\partial \delta t^*}{\partial b_{ijk}}$ is obtained from:

$$\frac{\partial \delta t^*}{\partial b_{ijk}} = \pi \int_{raypath} \frac{\rho_{ijk}(x,y,z)}{V(x,y,z)} dr \quad . \qquad (16)$$

Using (15) and (16), each earthquake i yields a matrix equation:

$$\mathbf{r}_i = \mathbf{M}_i \Delta \mathbf{m} \qquad (17)$$

where $\mathbf{M}_i$ is the matrix of $\frac{\partial \delta t^*}{\partial b_{ijk}}$; and $\Delta \mathbf{m}$ the perturbations to the differential attenuation coefficients. The matrix equation is solved using the damped least-squares procedure

$$\Delta \mathbf{m} = (\mathbf{M}_i^{\mathrm{T}} \mathbf{M}_i + \xi^2 \mathbf{I})^{-1} \mathbf{M}_i^{\mathrm{T}} \mathbf{r}_i \qquad (18)$$

where $\mathbf{I}$ is an identity matrix and ξ a damping parameter (Menke, 1989). The matrix inverse is obtained using singular value decomposition. The resulting differential attenuation adjustments $\Delta \mathbf{m}$ are added to the initial model and new δt^*_{cal} are then computed from the updated model. New residuals are calculated and the least-squares problem is solved for new velocity adjustments. This procedure is done iteratively until

the residuals fall below a predefined acceptable value.

4.3.2 Site Correction

Figures 4.4a and 4.4b show the amplitude spectra for various-size events observed at 16 stations. The spectral shapes vary widely among stations but exhibit remarkable consistency for each station regardless of the size ($0.0<M_L<2.0$) and location of the events. The spectral roll-off at higher frequencies (apparent corner frequency f_c) for the recorded events are similar for each station. Stations 1, 2, 4, 5, 6 and 9 exhibit apparent corner frequencies of 40 Hz or higher while stations 12, 13, and 15 have corner frequencies below 30 Hz. The spectra also show consistent peaks at certain frequencies, but these peaks do not reflect source contributions since they are not common among stations for the same event. Rather these observations suggest that local site effects are strongly influencing the observed spectra. Majer and McEvilly (1979) also observed that corner frequencies at The Geysers are roughly independent of the seismic moment and suggested that possible path effects mask the source response due to high attenuation. Other studies have observed site-dependent spectra in other areas. Frankel (1982) and Frankel and Wennerberg (1989) found that microearthquake corner frequencies correlate with the receiver site in studies at the Caribbean and Anza, California. They argued that this effect was produced by severe local attenuation under each site. Hanks (1982) also observed that the corner frequencies in the acceleration spectra (f_{max}) are different values for stations located on bedrock and those located on alluvium, possibly arising from strong absorption by low-Q materials. The stations that display high f_c are located on chert and metagraywacke units while those that have relatively low fc tend to be situated on greenstone. Other mechanisms that would alter

Figure 4.4 Spectra of several events recorded at 16 stations. The spectra show similarity in shapes and apparent corner frequencies for various-size events recorded in a particular station and their variability among stations. The systematic site variations are corrected by the reference spectra in the spectral ratios. (A) P-wave, vertical component. (B) S-wave, horizontal component.

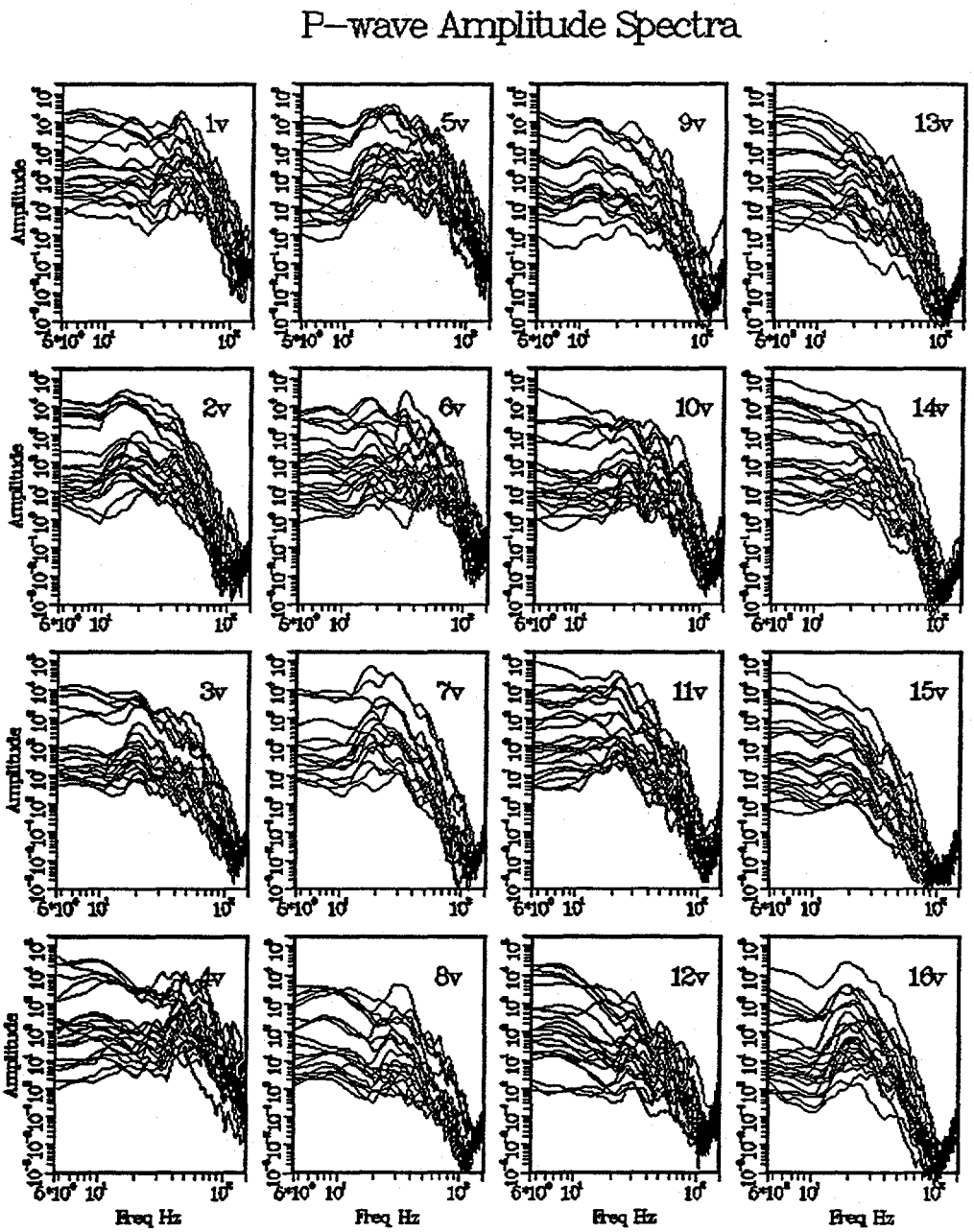
P--wave Amplitude Spectra
1v
5v
9v
13v
2v
6v
10v
14v
3v
7v
11v
15v
4v
8v
12v
16v
Amplitude
Freq Hz

Figure 4.4a

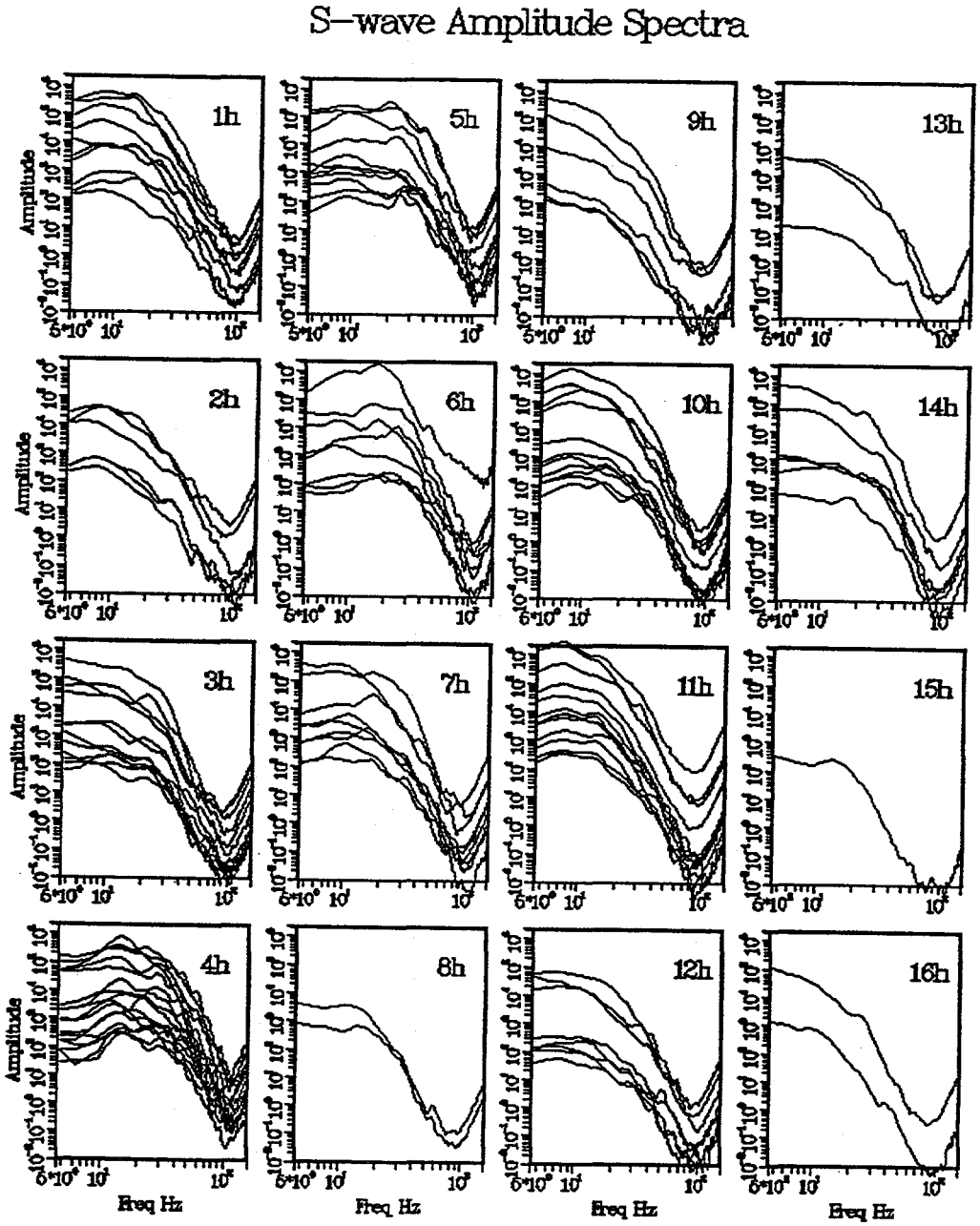
S–wave Amplitude Spectra
1h
5h
9h
13h
2h
6h
10h
14h
3h
7h
11h
15h
4h
8h
12h
16h
Amplitude
Freq Hz

Figure 4.4b

spectral shapes include site resonances (Cranswick et al., 1985) and near-surface scattering (Frankel and Clayton, 1984 and 1986) that can produce narrow-band amplification and sharp corner frequencies in the observed spectra. These observations demonstrate the need to deconvolve the reference site response from the observed spectra. Figures 4.5a and 4.5b present the normalized P- and S-wave reference spectra used for all stations.

The source contribution in the spectrum does not affect the attenuation calculation at frequencies below the corner frequency. Most events in the study have magnitudes $M \leq 1$, so expected corner frequencies would be in the range $f_c \geq 50$ Hz. The relatively constant apparent corner frequency for each site independent of event size, and the wide range of inter-station variation, suggest strongly that the source contribution to the spectrum is being masked by a site-specific response, and that attenuation is affecting the spectrum over a wide frequency range. Given these observations, a test was conducted to find the usable bandwidth in the attenuation calculation. The results of several inversion runs with different bandwidths were compared: case 1) 4 to 40 Hz for the P-wave and 4 to 30 Hz for the S-wave; case 2) 4 to 60 Hz and 4 to 40 Hz ; case 3) 4 to 80 Hz f and 4 to 60 Hz. The signal-to-noise ratio deteriorates above 80 Hz. The final inversion residuals for each case are 52, 39 and 30 ms for cases 1, 2 and 3, respectively. Figures 4.6a and 4.6b present the results of the tests with horizontal model slices at a depth of 1 km. The cross sections display a 5 x 5 km^2 area centered at the CCSF. Colors indicate variations in differential attenuation with red showing regions of high attenuation. Intensity denotes model resolution as defined in the next section. Comparison of the three cases show recovery of similar features, although the amplitudes of the anomalies vary somewhat. Some differences are apparent in the poorly resolved areas near the edges. Based on the similarity of the resulting structures and size of the residuals obtained in the inversion, it is concluded that the source corner frequency is not degrading the inversion at high frequencies. The maximum bandwidth,

Figure 4.5 Normalized reference spectrum of each station derived from the average of the spectrum of all events that were recorded in each particular station. Station names are shown on the upper right corner for each plot. (A) P-wave. (B) S-wave.

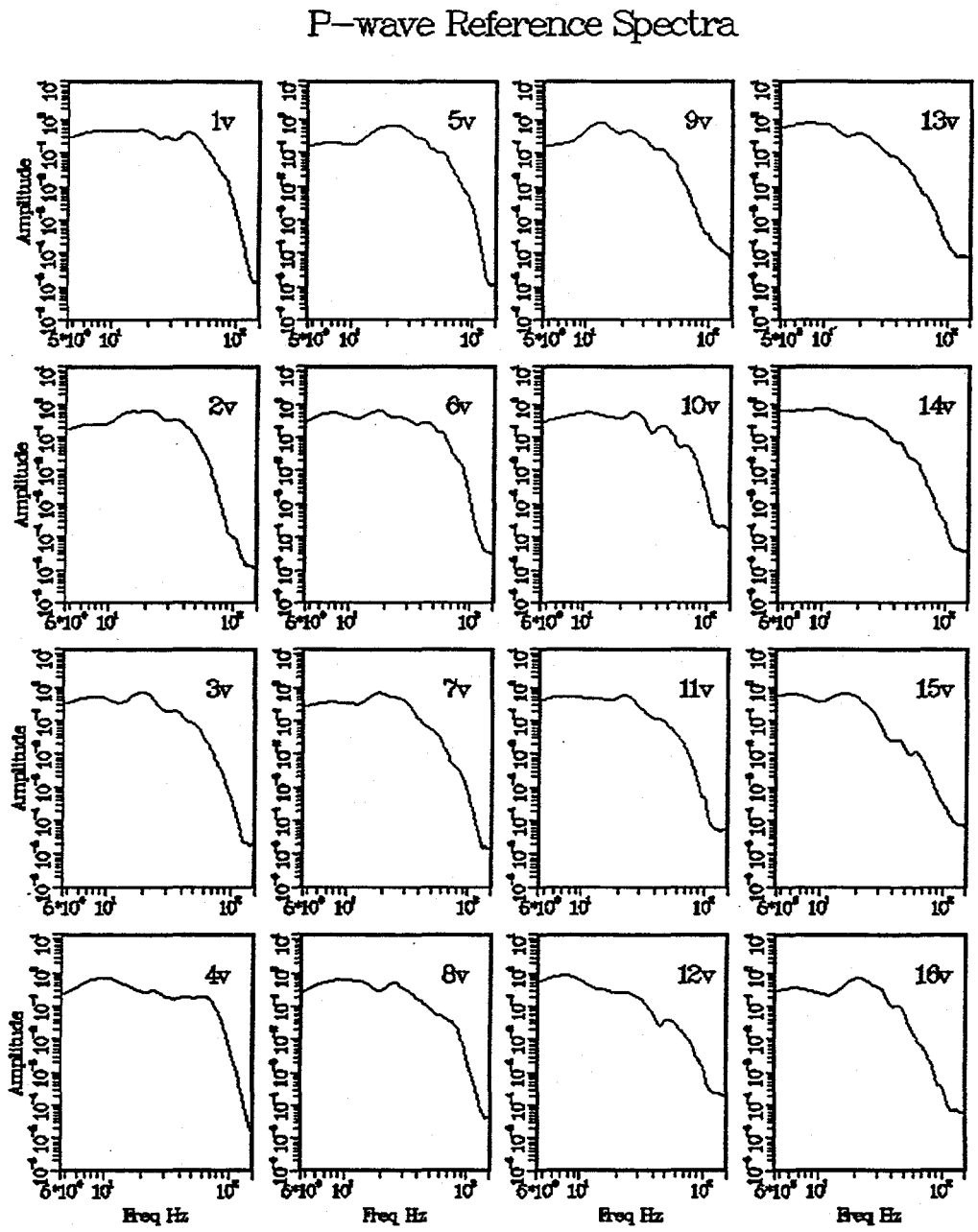
P–wave Reference Spectra
1v
5v
9v
13v
2v
6v
10v
14v
3v
7v
11v
15v
4v
8v
12v
16v
Amplitude
Freq Hz

Figure 4.5a

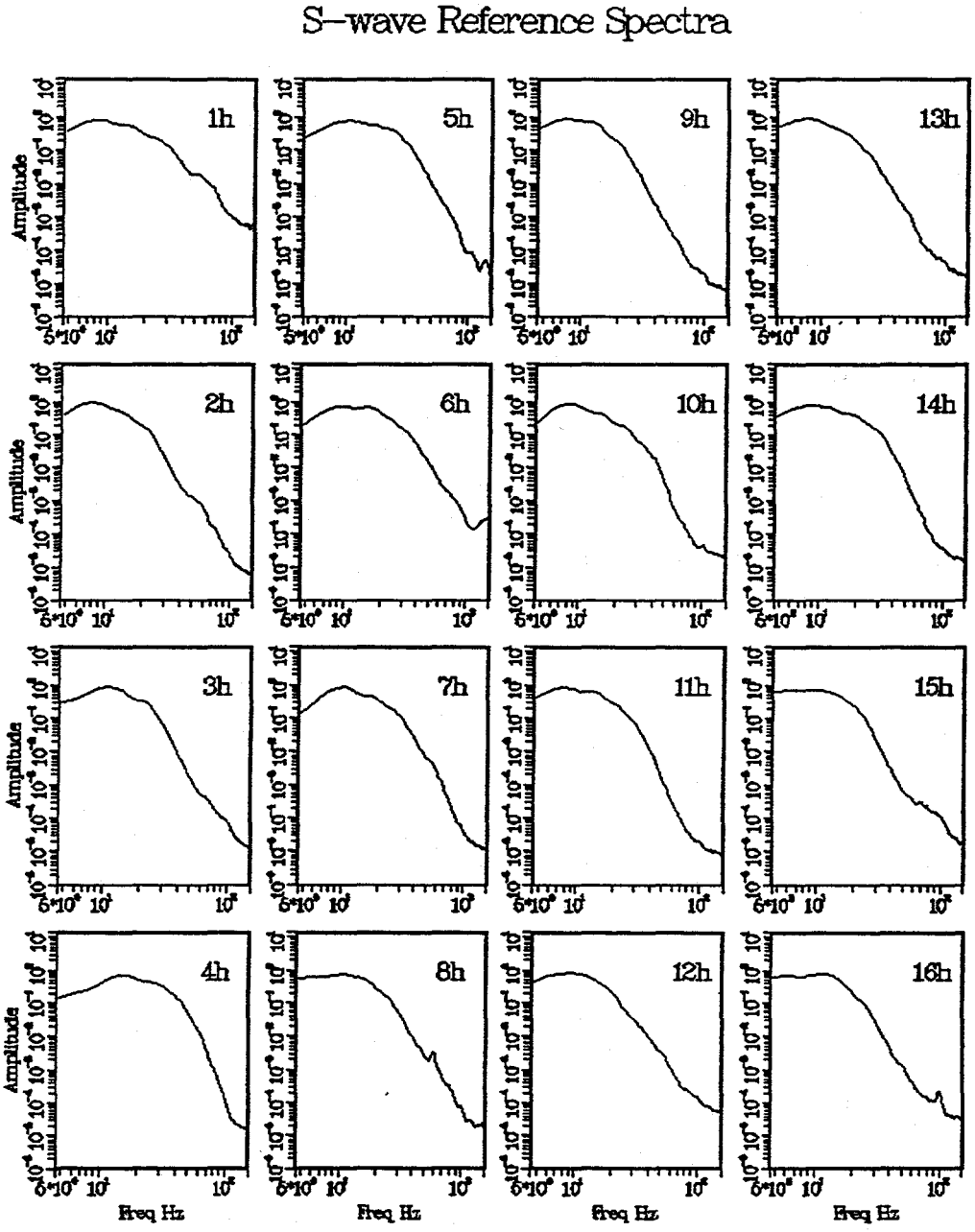
S–wave Reference Spectra
1h
5h
9h
13h
2h
6h
10h
14h
3h
7h
11h
15h
4h
8h
12h
16h
Amplitude
Freq Hz

Figure 4.5b

Figure 4.6 Differential attenuation and spectral bandwidth. The cross sections display a 5 x 5 km^2 area centered at the CCSF (outlined) at a depth of 1 km. Red indicate regions of high attenuation and blue for relatively low attenuating regions. Low intensity denotes poorly resolved regions. (A) P-wave. (B) S-wave. Note the similarity in the gross features of the resulting models despite the difference in the spectral bandwidth of the data.

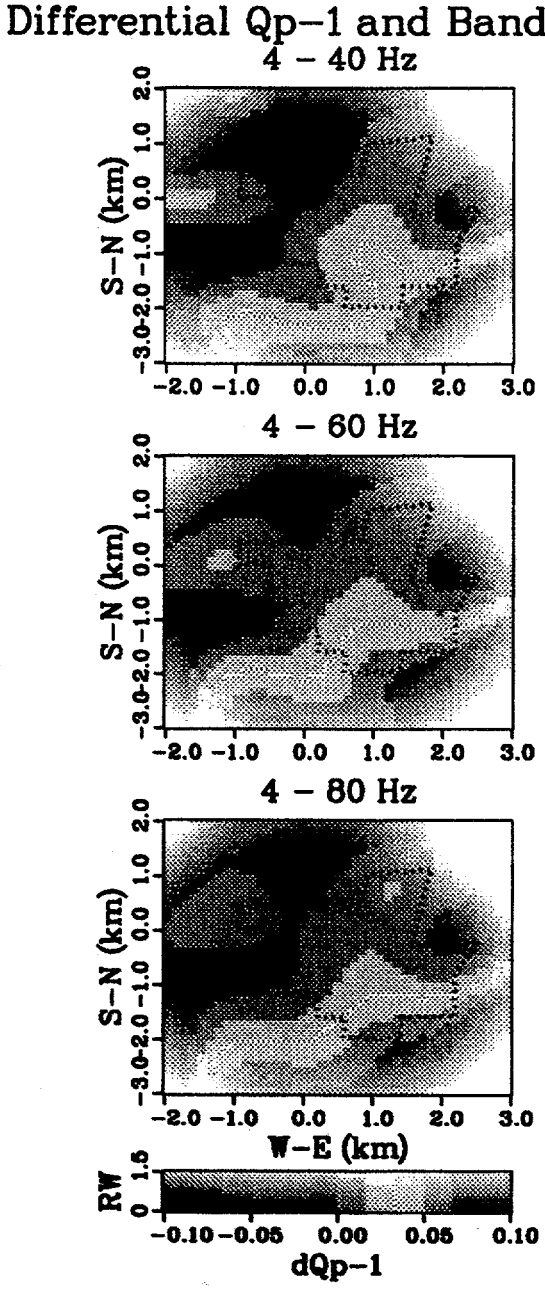
Differential Qp−1 and Bandwidth
4 − 40 Hz
4 − 60 Hz
4 − 80 Hz
S−N (km)
2.0
1.0
0.0
−1.0
−2.0
−3.0
−2.0 −1.0 0.0 1.0 2.0 3.0
W−E (km)
RW
1.5
0
−0.10 −0.05 0.00 0.05 0.10
dQp−1

Figure 4.6a

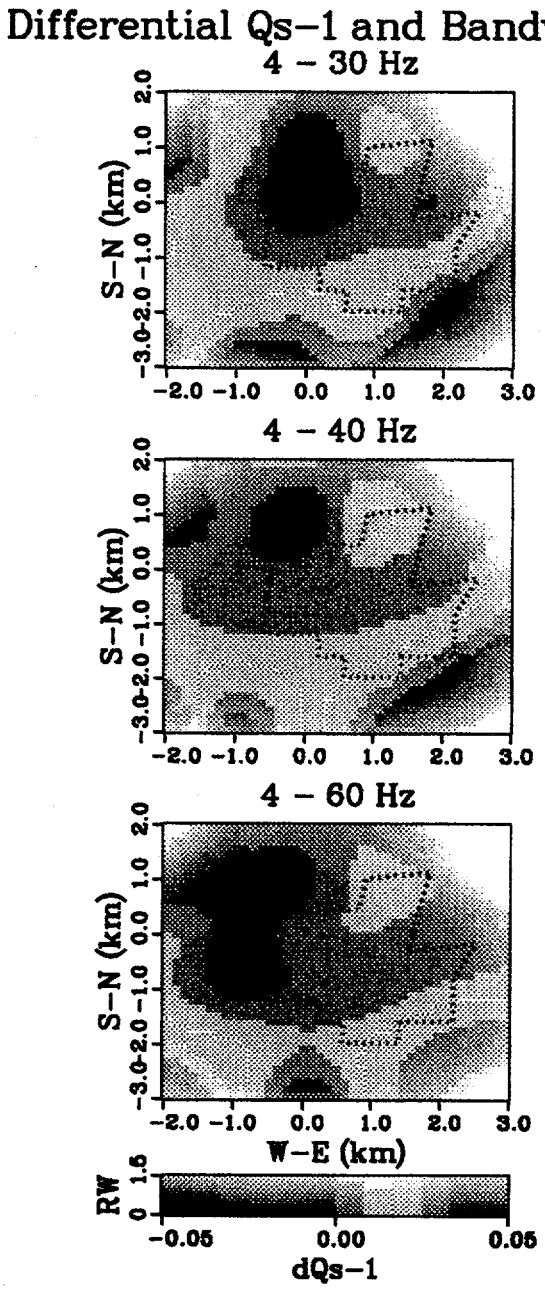
Differential Qs−1 and Bandwidth
4 − 30 Hz
4 − 40 Hz
4 − 60 Hz
S−N (km)
2.0
1.0
0.0
−1.0
−2.0
−3.0
−2.0 −1.0 0.0 1.0 2.0 3.0
W−E (km)
RW
1.5
0
−0.05 0.00 0.05
dQs−1

Figure 4.6b

case 3, having the best residuals, is selected as the optimum bandwidth for the final modeling.

4.3.3 Synthetic Data Tests

Tests with synthetic data were conducted to explore the resolving power of the data set. Synthetic amplitudes from two artificial starting models were first generated using the same source-receiver geometry as in the real inversion problem. The synthetic structures, shown in Figure 4.7 , consist of alternating positive and negative anomalies of amplitude ± 0.1 δQ^{-1} located at the southeast quadrant of the target region. Background Q^{-1} was obtained from Zucca et al. (1994) and Majer and McEvilly (1979). The synthetic structures were then inverted and the results were assessed by comparing recovered images to the original structure. Figures 4.8 and 4.9 present the recovered P- and S-wave synthetic structure over the target region. Shaded areas denote regions with good model resolution while lighter areas represent decreasing resolution. Blank areas at the edges of the target region indicate very poor model resolution. A compact form of describing the model resolution is using the resolving width function RW (Menke, 1989; Michelini and McEvilly, 1991). RW uses the distance between inversion nodes as a weighting factor for the rows of the model resolution. Well-resolved inversion nodes have RW values near zero while poorly resolved ones have higher positive values. The upper limit of RW is determined by the model resolution and the node spacing and therefore is unique for every inversion problem. For this inversion study, 1.5 was considered as the cut-off value for poorly resolved parameters. As expected, the spatial variation of the model resolution is identical to the one recovered in the velocity inversion discussed in chapter three because of similar ray paths. The results show that the target region is reasonably well-resolved to a depth of 2 km for both P- and S-wave synthetic structures. The test inversion adequately recovered the

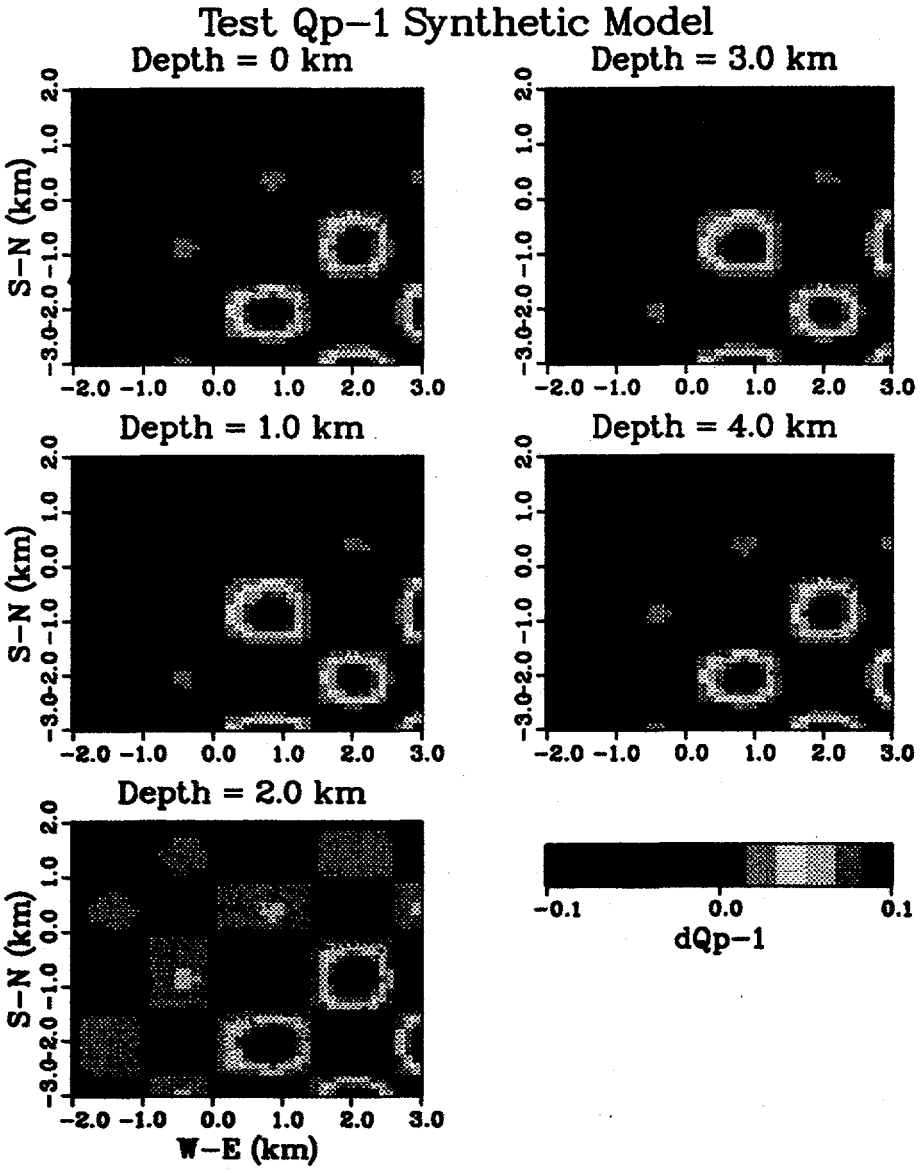

Figure 4.7 Horizontal cross sections of the test differential attenuation structure taken at several depths. The plots display a 5 x 5 km^2 area centered at the CCSF (outlined). The synthetic structure consists of alternating positive and negative anomalies of amplitude ±0.1 δQ^{-1} located at the southeast quadrant of the target region. Red indicate regions of high attenuation and blue for relatively low attenuating regions. Triangles mark station locations.

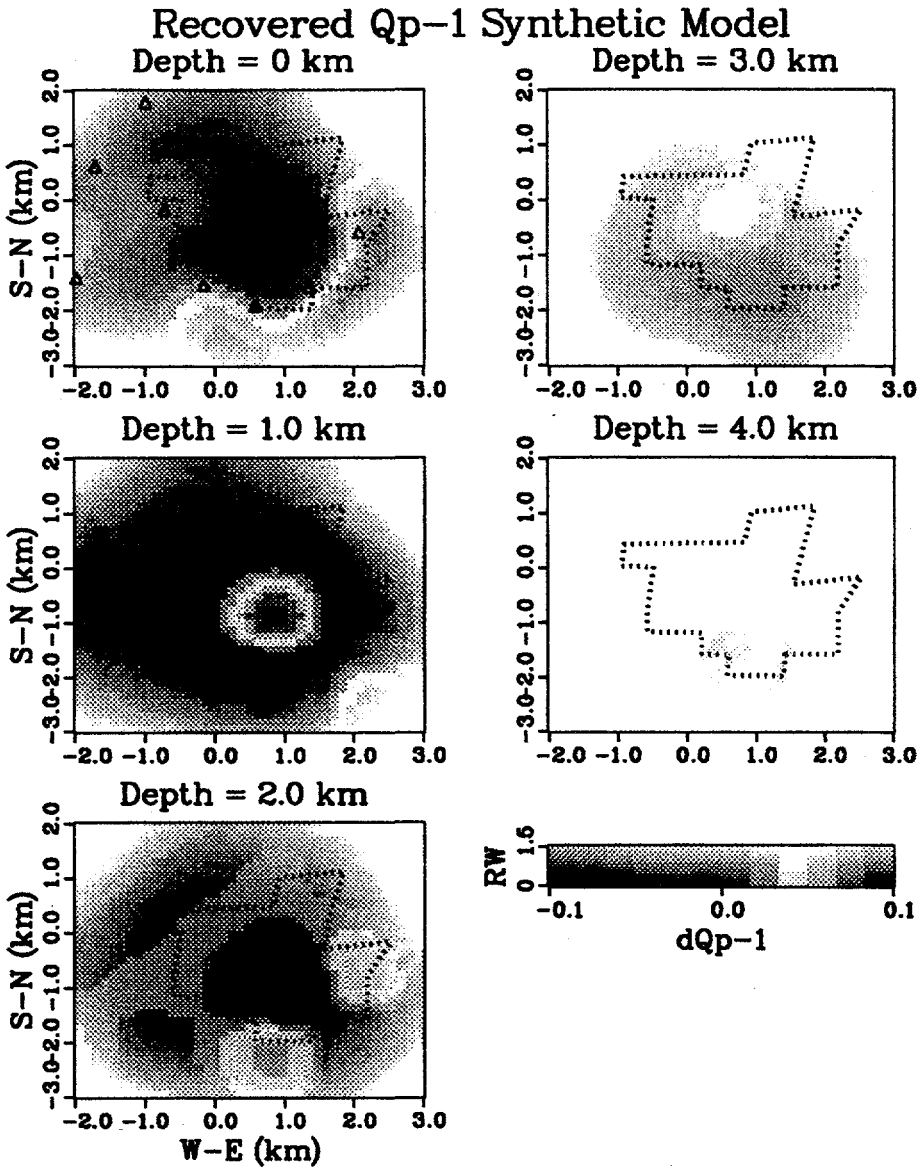

Figure 4.8 Horizontal cross sections of the resulting synthetic P-wave differential attenuation structure taken at several depths. Intensity indicates model resolution as defined by the resolving width function RW. Blank areas indicate regions with poor model resolution. Triangles mark station locations.

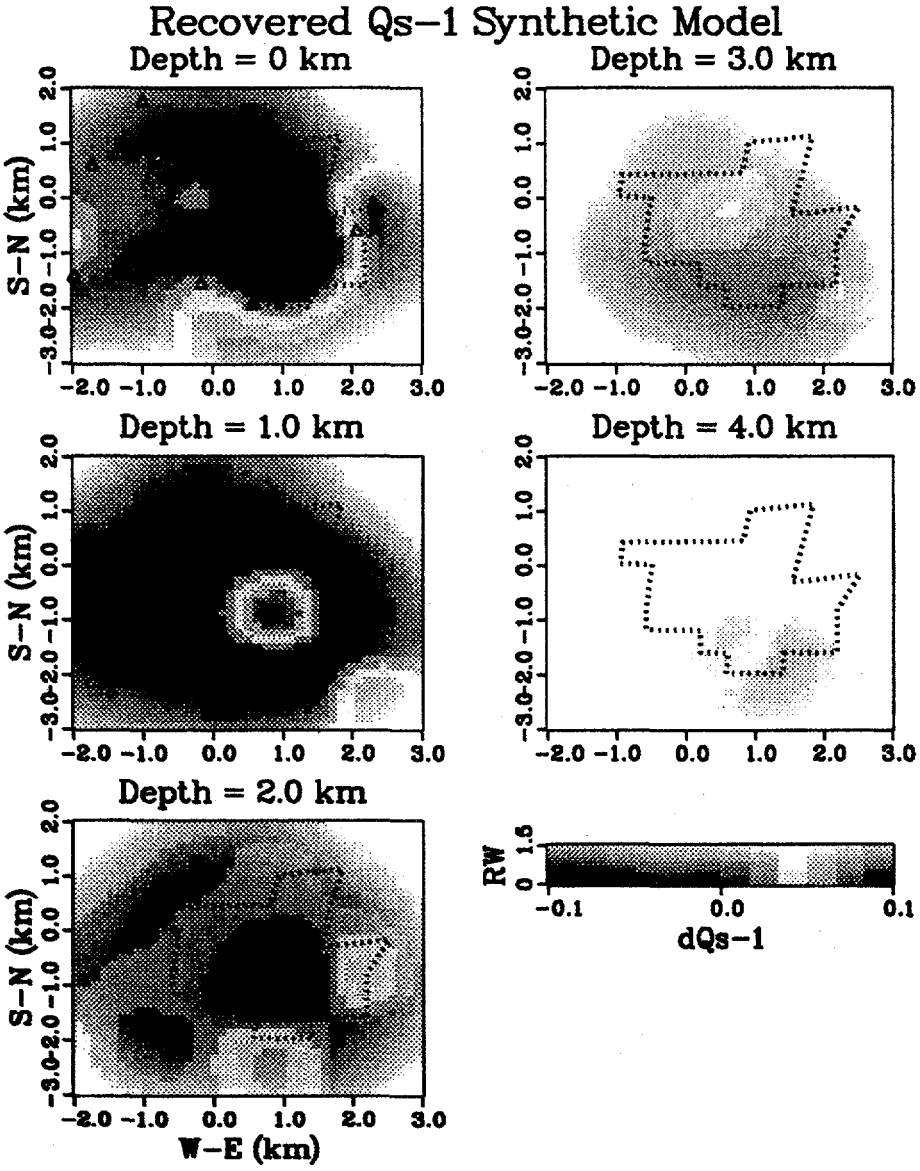

Figure 4.9 Horizontal cross sections of the resulting synthetic S-wave differential attenuation structure taken at several depths. See Figure 4.8 caption.

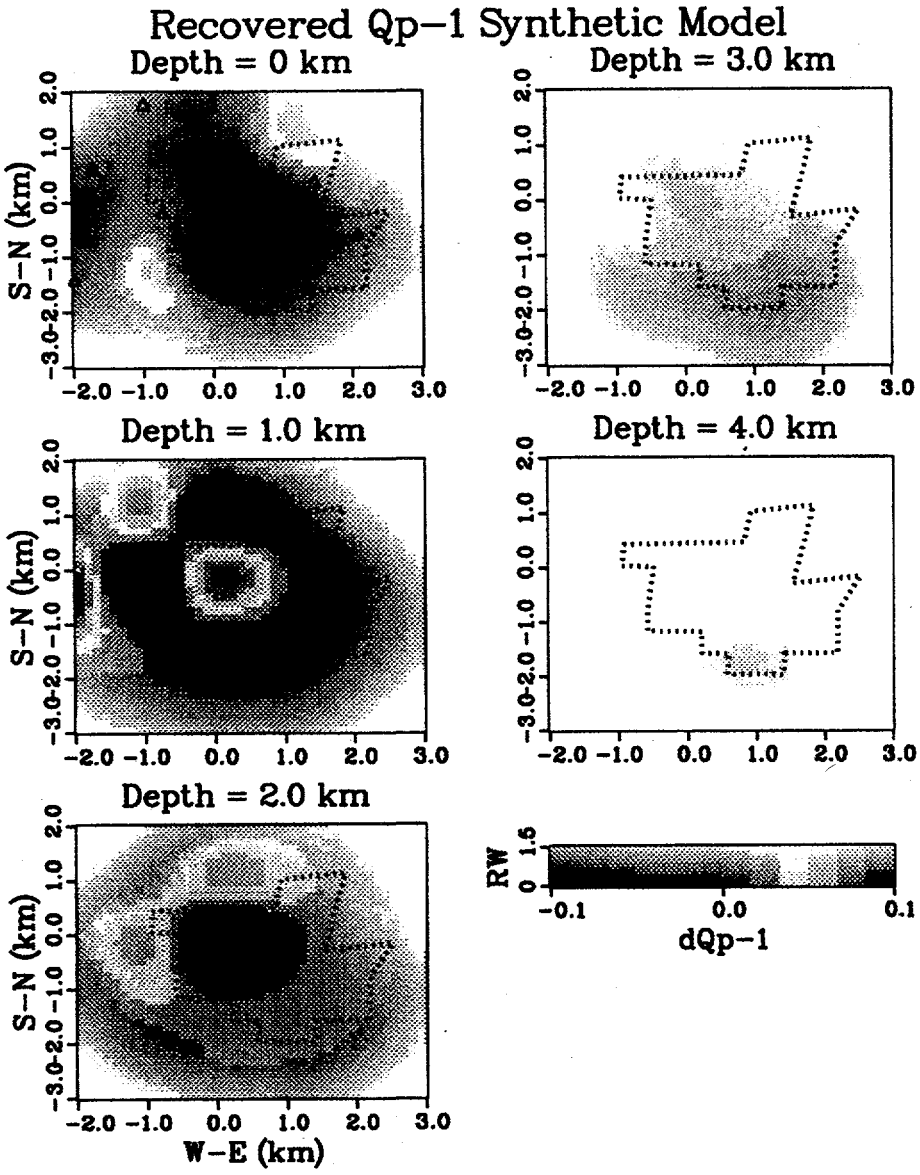

Figure 4.10 Horizontal cross sections of the resulting synthetic P-wave differential attenuation structure taken at several depths. The synthetic structure consists of alternating positive and negative anomalies of amplitude ±0.1 δQ^{-1} similar to that in Fig. 4.7, but located at the northwest quadrant of the target region. See Figure 4.8 caption.

southeastern anomalies with amplitudes of about 90% of the original in the well-resolved regions. The tests also reveal some smearing of the anomalies at the surface especially outside the network and near the edges of the target region. In the final inversion, less weight was given to the anomalies located at the edges of the target region. Some small anomalies not present in the original synthetic structure appear elsewhere in the region but their amplitudes do not exceed 10% of the original. The same test was repeated for synthetic anomalies located in the northwest quadrant of the target region., and again the main anomalies were basically recovered, as shown in Figure 4.10, but with relatively more smearing especially at the surface, probably due to fewer sources in this region. The center is well resolved to a depth of 2 km. It is concluded that the inverse procedure can infer heterogeneity with scale lengths of 1 km within the well-resolved central regions of the CCSF.

4.4 Inversion Results

The final data set inverted consisted of approximately 9600 arrivals, including about 2700 S-wave. The P- and S-wave residuals for the final model, presented in Figure 4.11, range between ±0.15 s with means very close to zero and standard deviations of about 0.03 s. The errors follow a Gaussian distribution, justifying the choice of the least squares approach for the inversion. The final model exhibits a root mean square residual of 30 ms, an improvement of 59% after four iterations beyond the starting model. The resulting P-wave (δQ_p^{-1}) and S-wave (δQ_s^{-1}) attenuation structures are presented in Figures 4.12 and 4.13. Horizontal slices at four depths through the 3-D volume are presented for each case. The cross sections display a 5 x 5 km^2 area centered at the CCSF. Colors and intensities are as described earlier.

The P-wave differential attenuation structure (Figure 4.12) shows significant

Figure 4.11 P- and S-wave residuals of the final differential attenuation model. Residuals range between ±0.15 s with means very close to zero and standard deviations of about 0.03 s. The error distribution generally follow a Gaussian distribution.

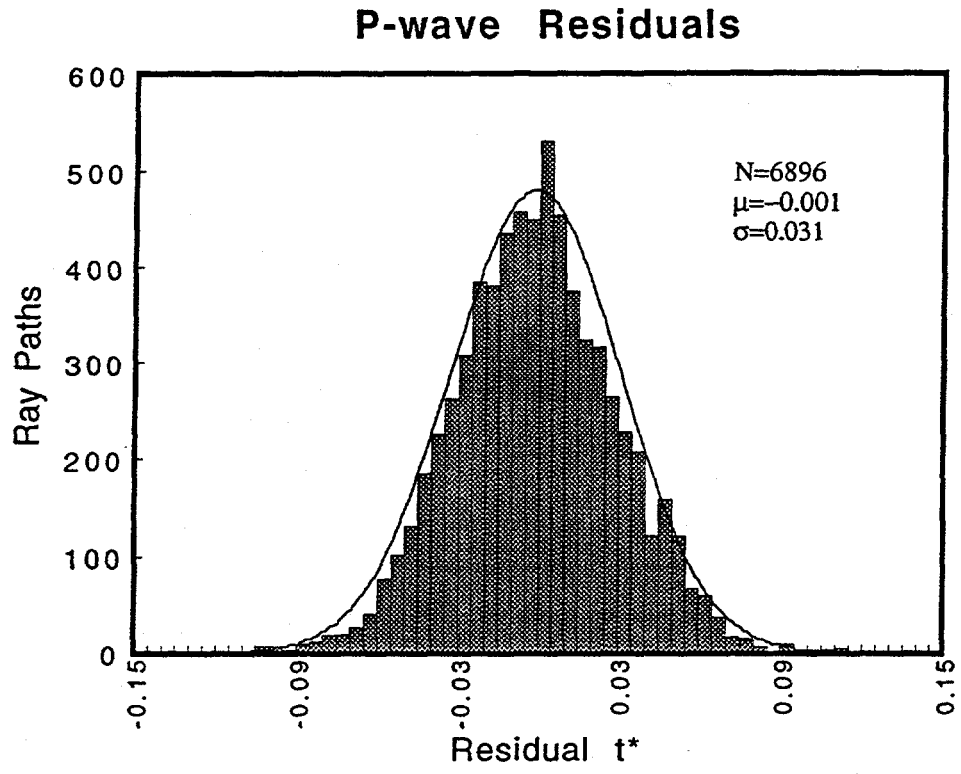
P-wave Residuals
N=6896
μ=-0.001
σ=0.031
Ray Paths
600
500
400
300
200
100
0
-0.15
-0.09
-0.03
0.03
0.09
0.15
Residual t*

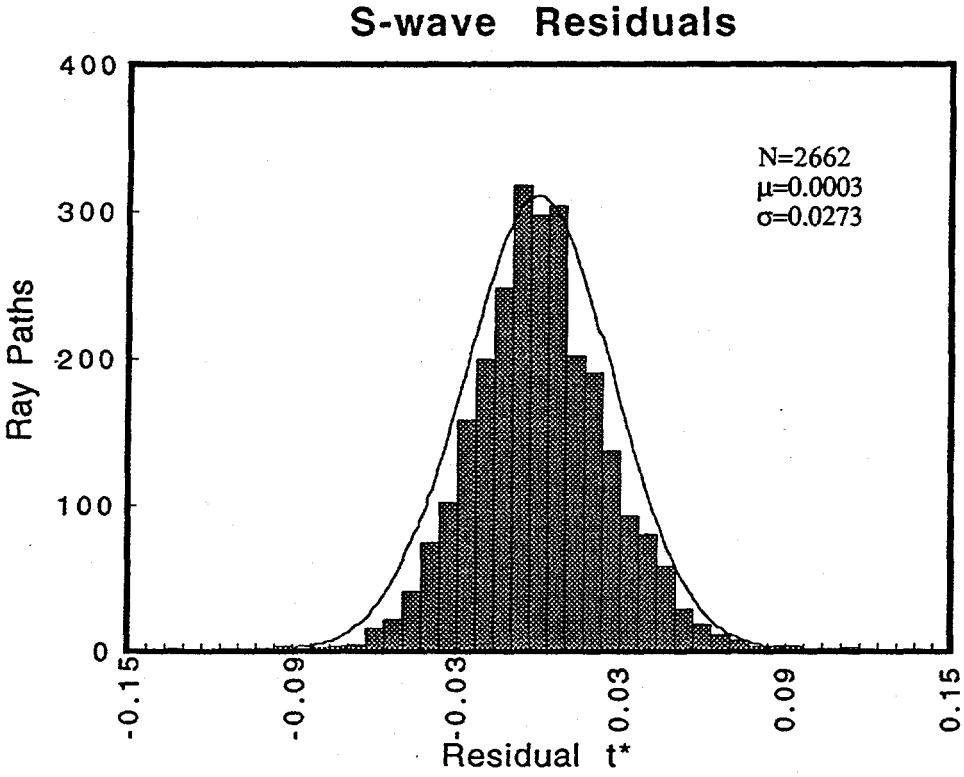
S-wave Residuals
N=2662
μ=0.0003
σ=0.0273
Ray Paths
400
300
200
100
0
-0.15
-0.09
-0.03
0.03
0.09
0.15
Residual t*

Figure 4.11

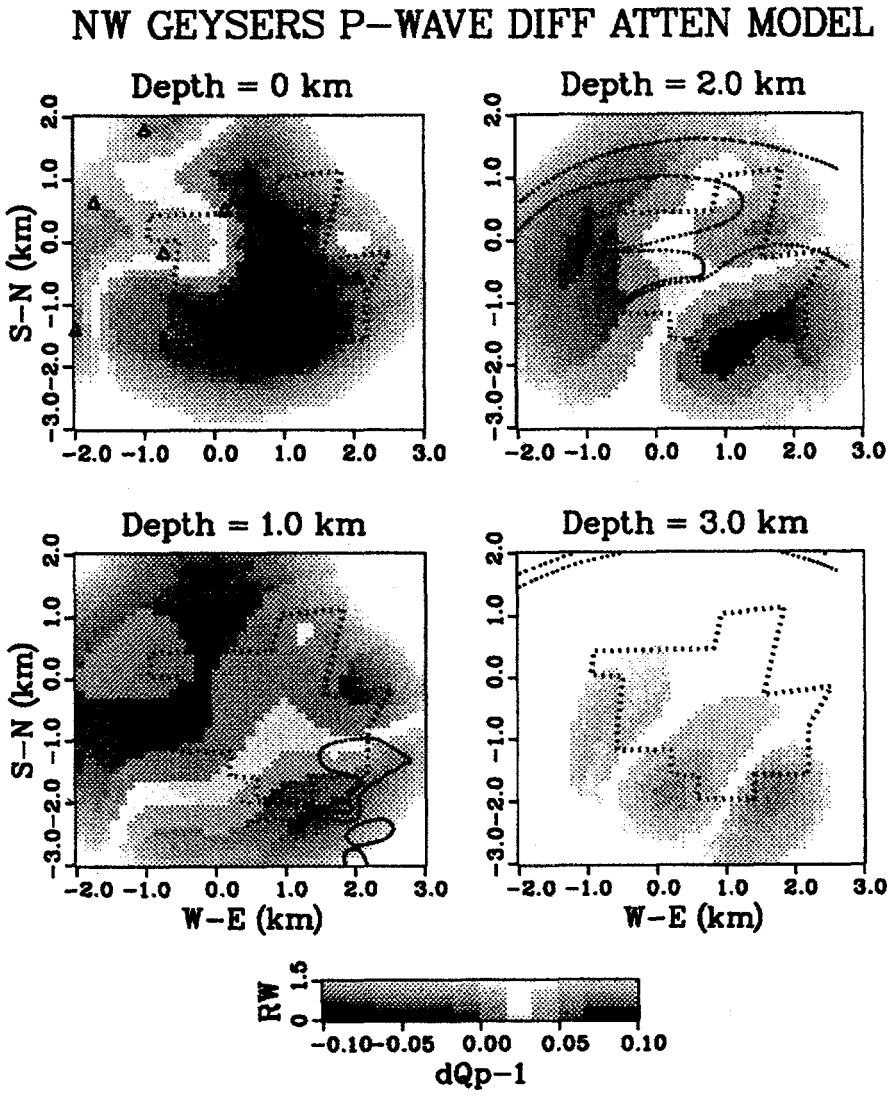

Figure 4.12 Horizontal cross section of the 3-D P-wave differential attenuation model (δQ_p^{-1}) taken at four depths. Contour lines of the top of the steam zone are also shown. Colors indicate variations in differential attenuation with red showing regions of high attenuation and blue for relatively low attenuating regions. Intensity denotes model resolution as defined in the synthetic test section. CCSF outline is shown for reference. Triangles mark station locations.

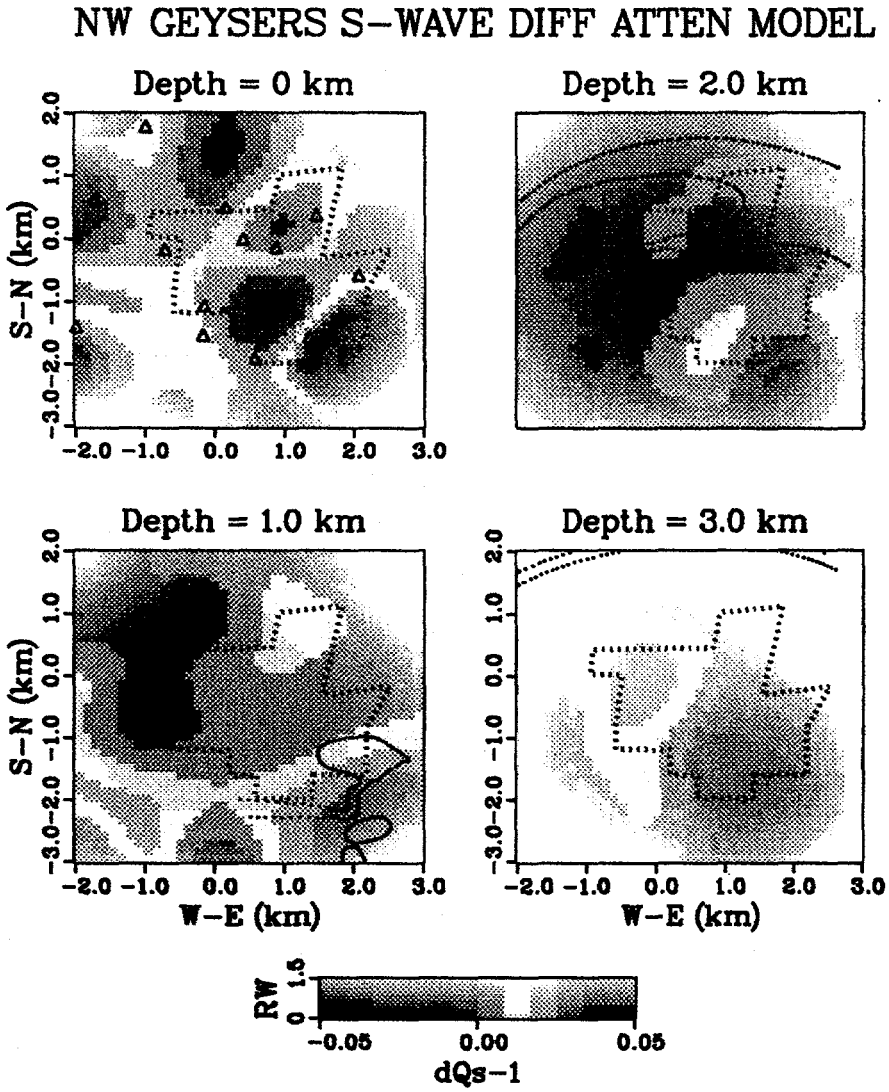

Figure 4.13 Horizontal cross section of the 3-D S-wave differential attenuation model (δQ_S^{-1}) taken at four depths. See Figure 4.12 caption.

near-surface variations. A prominent high δQ_p^{-1} anomaly with values of up to 0.1, centered around Squaw Creek (see Figure 4.1), covers the western edge of the field. This anomaly also coincides with low topographic elevation compared to the rest of the region. Lower δQ_p^{-1} with values of up to -0.1 characterize the southern part of the CCSF at the surface. Finally, an extensive high attenuation region, with values exceeding 0.1, is seen at the southern edge of the field at a depth of 1 km depth. At 2 km depth, this high δQ_p^{-1} region extends northward and covers most of the central part of the field. The main anomaly continues northwestward at 3 km depth. Its deeper extent is uncertain because of poor resolution.

The S-wave differential attenuation (Fig 4.13) structure also exhibits significant lateral variability. The near-surface is characterized by widespread high attenuation, with δQ_p^{-1} values of about 0.05, except for an isolated low attenuation anomaly, located at the southeastern edge of CCSF. High attenuation is present at the southeastern edge of the field at 1 km depth and extends to the central and northern portion of the field but with lower amplitudes (δQ_s^{-1} is less than 0.02). Diffuse high attenuation regions are present at the southern half of CCSF at 2 km and possibly continue with depth.

δQ_s^{-1} amplitudes are generally less than those of the δQ_p^{-1}. Several reasons could explain this observation. The fewer S-wave ray paths contributed less to the prediction of δQ_s^{-1} model parameters. Another possibility is that the S-wave window may be contaminated by the higher frequency P-wave coda thereby increasing the slope of the spectral ratio. This interpretation, put forward by Ponko and Sanders (1994), could be verified by increasing the time window in the seismogram and then looking at the change in the resulting structure. However, the fact that the results did not change appreciably for a longer time window, as discussed earlier, means that the P-wave coda does not significantly contaminate the S-wave window. This contention is further supported by the large, often impulsive S-wave arrivals in the seismogram whose amplitudes are typically several orders of magnitudes larger than the preceding P-wave

coda. Another explanation that could be put forward is that the S-waves are actually suffering less relative attenuation compared to the P-waves. The last hypothesis is preferred because, as will be discussed later, the difference in attenuation characteristics of the P- and the S-waves have some physical basis for the geothermal reservoir.

4.5 Discussion

The main features in the final inversion are: 1) Near surface high S-wave attenuation; 2) High P-wave attenuation in the Squaw Creek area west of CCSF; 3) Near surface low P-wave attenuation at the southern and southeastern sections of CCSF; and 4) High P-wave and S-wave attenuation at the southern regions of the field starting at 1 km and spreading northwestward at depth. In this region, $Q_p^{-1} > Q_s^{-1}$.

The near surface high Q_s^{-1} and Q_p^{-1} (in some areas) comes as no surprise because the rocks at shallow depths tend to be more weathered and fractured than deeper rocks. The subsurface geology (Figure 4.1) consists mainly of interbedded metagraywacke, metasiltstone and argillite partially overlain by relatively thin layers of Franciscan melange and greenstone units (Sternfeld, 1989). The melange unit is offset by shears and shallow-dipping thrust faults that were subsequently displaced by high-angle normal and strike-slip faults (Nielson et al., 1991). The high attenuation is most prominent in the confluence of Wildhorse and Squaw Creeks west of the CCSF. The high Q^{-1} anomaly, especially around the Squaw Creek area (which has the lowest average elevation and is the main drainage out of the target region), probably indicates liquid-saturated regions that are confined to the near surface. The high Vp/Vs values also found near-surface attests to these saturated conditions and may suggest regions affected by meteoric recharge (Chapter three; Moos and Zoback, 1983). O'Connell and Johnson (1991) likewise observed peaks in Vp/Vs ratio at shallow depths which they

interpret as the steam condensation zone.

A region of relatively low Q_p^{-1} is evident at the southern and southeastern sections of CCSF. This region coincides with high-velocity anomalies as discussed in chapter three. The observed high velocity and low attenuation structures correspond to mapped sections of Franciscan metagraywacke and greenstone (Nielson et al., 1991). In particular, the prominent high velocity and low Q_p^{-1}, and to a lesser extent low Q_s^{-1}, region southeast of the CCSF is coincident with the only substantial outcropping of the metagraywacke reservoir rocks. Elsewhere, higher attenuation and lower velocities and seem to be related to the Franciscan melanges west of the field at shallow depths.

Higher attenuation properties underlie the southern region at 1 km depth.. This anomaly is more widespread at 2 km depth with some indication of it extending below 3 km depth as model resolution is lost. The anomaly is characterized by higher Q_p^{-1} than Q_s^{-1}. At a depth of 2 km, where the anomaly is most prevalent, Q_p^{-1}/Q_s^{-1} is about 3.5. Low Vp/Vs values also characterize this region (Chapter three). Both the high Q_p^{-1}/Q_s^{-1} and the low Vp/Vs values suggest undersaturation of the reservoir rocks (Winkler and Nur , 1979; Toksöz et al., 1976; Gregory, 1976). Coincidentally, most of the steam entries also occur within this region and there is a good agreement between the shallowest steam entries and the top of the high Q_p^{-1} anomaly. Fig 4.14 presents a composite model of the steam reservoir as inferred from both the Vp/Vs and Q_p^{-1} variations. High Q_p^{-1} and low Vp/Vs thus seem to delineate the steam reservoir. In a related study, Zucca et al. (1994) also found an attenuation increase within the steam reservoir where they inferred a partial liquid saturation of less than 70%. Majer and McEvilly (1979) also reported low Vp/Vs values within the steam producing horizon. This observation is consistent with the vapor-dominated nature of the reservoir. This low Vp/Vs anomaly is interpreted in chapter three to be indicative of high rock temperatures and the presence of gases. Walters et al. (1988) described a high

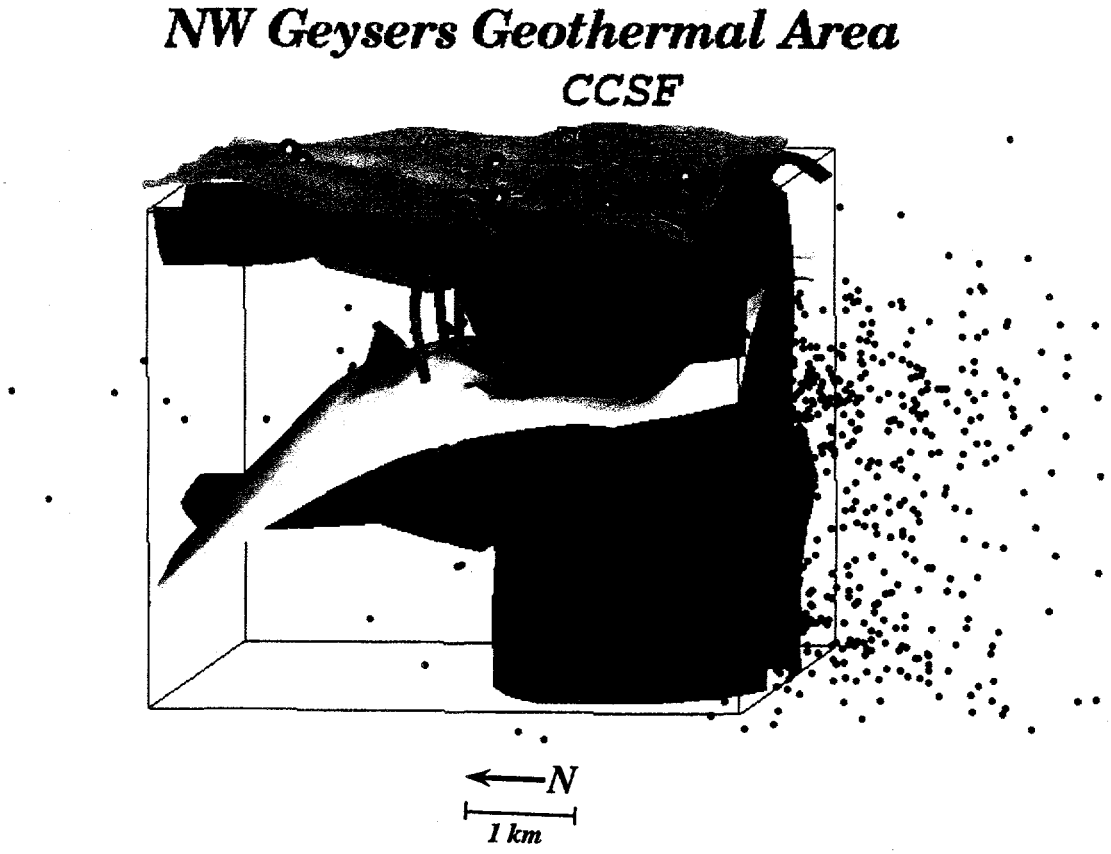

Figure 4.14 Composite model of the Northwest Geysers geothermal region. Plot shows a 3-D cross-section beneath the CCSF (outline at the surface). Orange shows the topography, the pink balls at the surface indicate seismic stations, the green tubes denote the boreholes within the CCSF and the small blue spheres mark microearthquake hypocenters. The red body encompasses regions with low Vp/Vs (<1.65) while the blue body indicates regions with high P-wave attenuation (δQ_p^{-1}>0.1). The grayish surface marks the top of the first steam entries (M. A. Walters, CCPA unpublished maps).

temperature vapor-dominated reservoir (HTR) characterized by high steam enthalpies, gas concentrations and reservoir temperatures compared to the "normal" Geysers reservoir underlying the southern sections of the field at depths of about 2.5 km. This observation is supported by geologic studies of Walters et al. (1988) and Sternfeld (1989) at the Northwest Geysers which describe the thermal alteration of the metagraywacke as hornfelsic starting at about 2.5 km depth. The high attenuation region seems to trend northwest as it gets deeper parallel to the regional structure. The subsurface structure generally dips to the northeast and is deformed by major northwest trending faults related to the San Andreas fault system. The distribution of this high attenuation anomaly, together with the low Vp/Vs, suggests that steam reservoir may continue northwest of the present known production limits at depths of greater than 3 km.

4.6 Conclusions

The differential attenuation structure in the CCSF is apparently closely related to the active geothermal activity at the Northwest Geysers region. High P-wave and S-wave attenuation ($Q_p^{-1} > Q_s^{-1}$) below 1 km depth at the southern regions of the field deepens northwestward following the known steam producing zone. The spatial extent of both the high Q_p^{-1}/Q_s^{-1} and the low Vp/Vs anomalies suggest that the steam reservoir may be present northwest of the known reservoir limits at increasing depths (at least 3 km). Future monitoring may be important in verifying this potential resource. The observed attenuation structure also exhibits some correlation with mapped geologic units. Near-surface low P-wave attenuation anomalies at the southern and southeastern sections of CCSF correspond to mapped sections of Franciscan metagraywacke. Station located near this geologic unit also exhibit high corner frequencies. Near-surface

high attenuation anomalies are associated with Franciscan melange. Near surface high attenuation and high Vp/Vs, especially around the Squaw Creek area west of CCSF, indicate liquid-saturated regions affected by meteoric recharge.

This study demonstrates that the high-resolution microearthquake data can be used effectively in characterizing the reservoir structure in the CCSF through attenuation tomography. Furthermore, when coupled with independently-determined velocity structure, greater confidence can be placed on interpretations of reservoir properties.

Chapter 5

VELOCITY STRUCTURE OF THE LONG VALLEY CALDERA FROM THE INVERSION OF LOCAL EARTHQUAKE P- AND S-WAVE TRAVEL TIMES

5.1 Introduction

Advances in three-dimensional travel time tomography in recent years have made it practicable to image complex geological structures on a regional scale, given reasonably well-distributed seismicity and seismographs. The method has been applied in active, well-instrumented areas such as The Geysers (Eberhart-Phillips and Oppenheimer, 1984; O'Connell and Johnson, 1991), Long Valley (Kissling, 1988), and Loma Prieta (Foxall, 1992) yielding smooth velocity models with resolutions of a few kilometers. Michelini and McEvilly (1991) were successful in constructing both P- and S-wave velocity models for Parkfield. With both P- and S-wave models, the Vp/Vs distribution is available, a parameter which contains information on the mechanical properties of rocks and fluids at depth. The method is applied in this study of the crustal structure beneath Long Valley caldera.

5.2 Background

Long Valley caldera (LVC) is a Quaternary volcanic structure located on the western margin of the Basin and Range province at the base of the Sierra Nevada frontal fault escarpment. The caldera was formed as a result of a voluminous ash eruption 760,000 years ago that created the Bishop tuff. Since that time the caldera has been the

site of numerous episodes of volcanism, the most recent being approximately 600 years ago. The detailed geology and history of the region are given by Bailey et al. (1976) and Bailey (1989). The simplified geology of LVC shown in Figure 5.1 is adopted from Bailey et al. (1976). Indications of renewed magma movement followed a series of large magnitude earthquakes in 1980 with subsequent surface uplift and inflation-consistent deformation. The associated heightened awareness of possible imminent volcanic eruption prompted numerous investigations into the current processes occurring within the caldera. The topic receiving most attention has been the search for the presumed magma chamber beneath the Resurgent Dome.

A number of geophysical studies argue for the existence of a magma body at shallow to midcrustal depths beneath LVC (reviews are presented by Hill et al. (1985a), Rundle et al. (1986), Goldstein (1988), and Goldstein and Stein (1988)). Refraction surveys showed possible seismic reflectors at depths of 7 to 8 km beneath the western margin of the Resurgent Dome, and these were interpreted by Hill (1976) and Hill et al. (1985b) as the top of a magma chamber. Luetgert and Mooney (1985) and Zucca et al. (1987) found deeper reflectors and proposed that these were reflections off the bottom of the magma chamber. Dawson et al. (1990) used teleseismic P-wave residuals to determine a three-dimensional (3-D) velocity structure, finding a low-velocity body between 7 and 20 km beneath the Resurgent Dome, a feature they interpret as a magma body of approximately 20% partial melt. In a more recent study, Steck (1991) found a low-velocity sill-like body beneath the western half of the caldera between 7 and 11 km depth which he postulates as the remnant magma chamber. Sanders (1984) mapped S-wave shadowing and defined a possible magma body between 5 and 8 km beneath the central part of the caldera, with the top possibly as shallow as 4 km.

Other studies have found no indications of anomalous regions beneath the caldera. In particular, a detailed tomographic study by Kissling (1988) found no

Figure 5.1 Simplified geologic map of Long Valley region adopted from Bailey et al. (1976). The caldera boundary is represented by the dotted outline. RD, Resurgent Dome; MM, Mammoth Mountain; CD, Casa Diablo; HCF, Hilton Creek fault; RVF, Round Valley fault; VT, Volcanic Tableland.

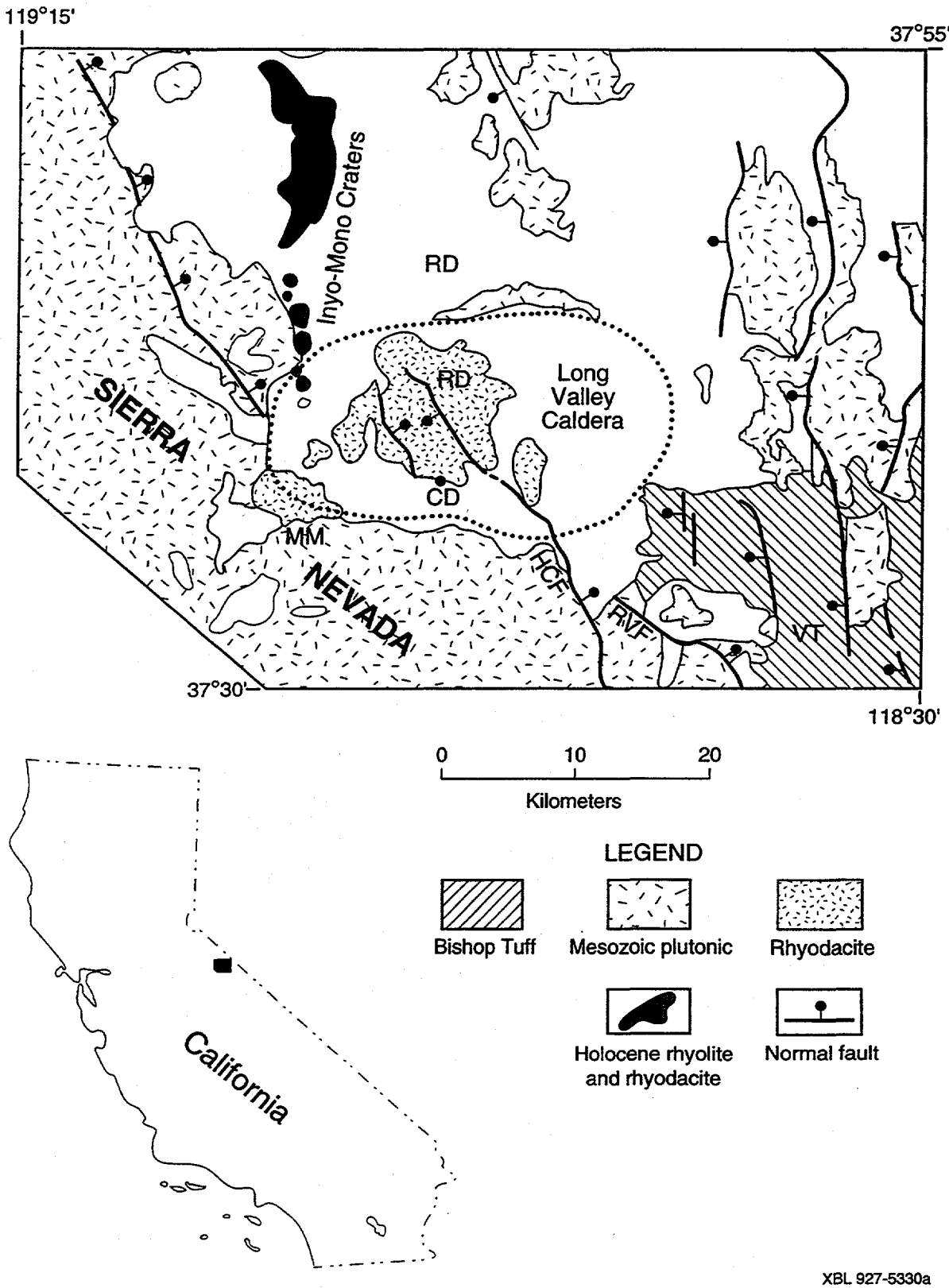
119°15'
37°55'
Inyo-Mono Craters
RD
RD
Long
Valley
Caldera
SIERRA
CD
MM
NEVADA
HCF
RMF
WT
37°30'
118°30'
0
10
20
Kilometers
LEGEND
Bishop Tuff
Mesozoic plutonic
Rhyodacite
Holocene rhyolite
and rhyodacite
Normal fault
California
XBL 927-5330a

Figure 5.1

evidence for a low-velocity region which would indicate the presence of a magma body beneath LVC. Hauksson (1988) suggested that the observed S-wave shadowing could be explained by radiation pattern effects. Black et al. (1991), employing a new migration algorithm, concluded that the events previously interpreted as reflections from a magma chamber were most probably reflections from the faults of the caldera ring fracture system.

In an attempt to resolve these conflicting results on the presence of a shallow magma chamber under LVC, a special high-resolution tomographic study was initiated to image the region beneath the caldera using the technique of joint inversion of microearthquake P- and S-wave travel times for velocity structure and hypocenters. In a joint U.S. Geological Survey (USGS) and Lawrence Berkeley Laboratory (LBL) effort, the dense microearthquake network at Long Valley was supplemented with new stations. A fan array of eight three-component borehole (80-160 m depths) receivers was installed on the northwestern rim of the caldera with digital telemetry at high resolution (16 bits gain-ranged, 480 samples per second per channel) to a local event-recording PC-based data acquisition system. The purpose of the fan array was to provide added ray path coverage in and below the Resurgent Dome, in the region of the proposed magma chamber, from microearthquake sources in the South Moat, in the Sierran Block south of the caldera, and in Chalfant Valley to the southeast. The resulting arrival time data were combined with those from the USGS and University of Nevada, Reno (UNR) seismographic networks to image the crustal structure within the caldera.

5.3 Data

The data for this analysis consist of direct P- and S-wave arrival times for local

earthquakes recorded by the composite network from June 1989 through August 1990. During the period of operation, about 2100 local earthquakes were recorded, most of which occurred near Mammoth Mountain, in the South Moat zone and in Chalfant Valley. A set of 280 high-quality events with a minimum of 10 P-wave arrivals were selected for the simultaneous inversion of hypocenters and velocity structure. The selected events, characterized by impulsive first arrivals and distinct S-wave phases, were well-distributed within the region of interest to provide uniformly dense ray coverage within the caldera.

Travel times from the refraction surveys (Hill et al., 1985b) provided constraints on the near-surface velocity structure. S-wave arrivals were timed only on the horizontal components of the available three-component stations, which include six portable seismographs deployed by UNR around the South Moat area between March and May 1990. The final data set consists of approximately 6900 arrival times, including about 700 S-wave arrivals. Figure 5.2 shows the station distribution and the epicenters of the 280 earthquakes used in the inversion.

5.4 Method

The joint problem for 3-D velocity distribution and hypocenter locations is solved with the progressive inversion scheme proposed by Thurber (1983). A series of linearized systems of equations relating travel time residual and adjustments in origin time, hypocentral coordinates, and velocity parameters is solved repeatedly using damped least squares. Parameter separation (Pavlis and Booker, 1980) is used to decouple hypocenter locations and velocity adjustments. A detailed discussion of the formulation used here is given by Michelini and McEvilly (1991). To limit the CPU time required in travel time computation, the approximate ray tracer developed by Um

Figure 5.2 Map showing the station distribution and the epicenters of the 280 earthquakes (small dots) used in the inversion. Triangles denote the network stations. Squares denote the three-component stations. The caldera outline is shown for reference.

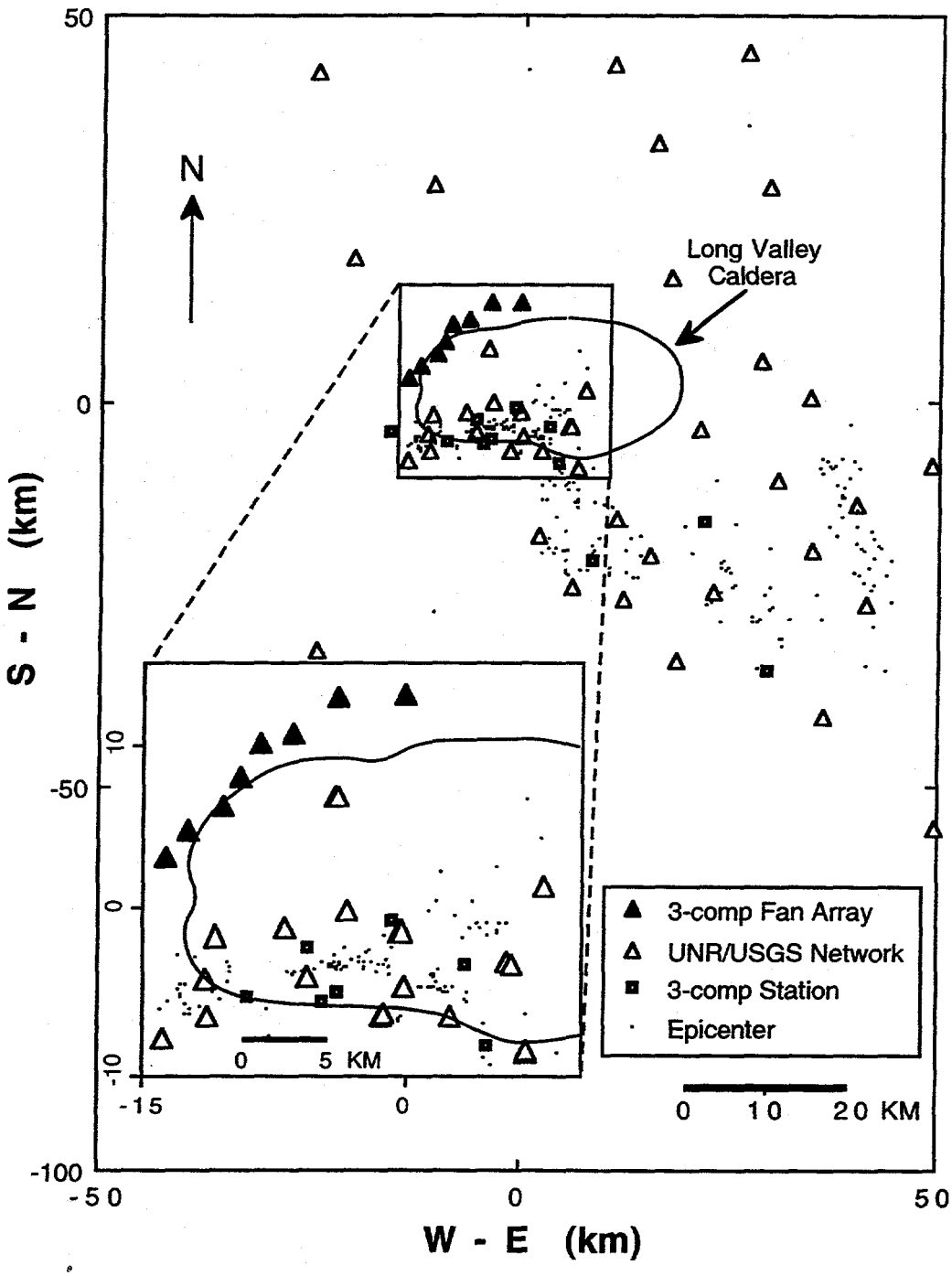
N
Long Valley
Caldera
50
0
-50
-100
-50
0
50
S - N (km)
W - E (km)
10
0
-10
-15
0
0 5 KM
0 10 20 KM
3-comp Fan Array
UNR/USGS Network
3-comp Station
Epicenter

Figure 5.2

and Thurber (1987) was used. Using a pseudo-bending method, the ray tracer produced errors less than 0.7% when compared to a more computationally intensive exact ray tracer. The region was divided into a 3-D rectangular grid with velocities assigned to each grid point. The starting P-wave velocity model is derived from the one-dimensional velocity model used routinely by the USGS to locate hypocenters in the LVC region (Figure 5.3). A Vp/Vs ratio of 1.73 is assumed for the corresponding S-wave model. The velocity model is parametrized in terms of cubic splines, yielding a smooth velocity model continuous everywhere up to the second spatial derivative. Starting hypocenter locations are fixed arbitrarily near the center of the caldera.

Tests with synthetic data were used to explore the resolving power of the data set and also to determine the best parameterization to be adopted in the actual velocity inversion for the entire Long Valley region. These tests are described in the following section.

5.5 Tests with Synthetic Data

Uncertainty and non-uniqueness are unavoidable problems in geophysical inverse problems. Finite model parameterization degrades short-wavelength image fidelity, while minimum allowable seismic ray density imposes a lower limit on node spacing. Overparametrization yields poorly sampled voxels and low resolution, as demonstrated by Toomey and Foulger (1989), who explored the trade-off between image fidelity and resolution using different parameterizations. Uneven ray coverage (due to limited source-receiver distribution) leads to a mixture of overdetermined and underdetermined "sub-problems", and some a priori information is required for solution. Furthermore, errors introduced by nonlinearity, arrival time uncertainties, model parameterization, and ray tracing smear the final velocity model and contribute to

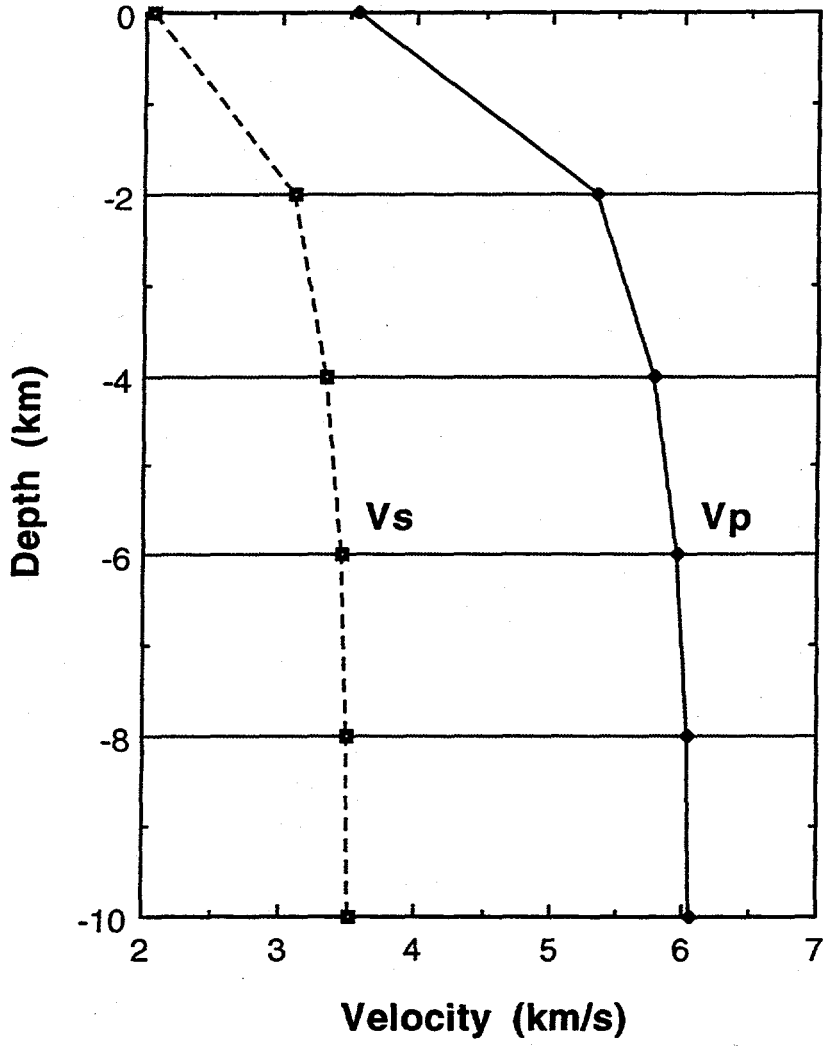

Figure 5.3 One-dimensional velocity structure for LVC used as "background" model for tests with synthetic data.

hypocenter mislocations. No straightforward estimate of the consequent uncertainties is available. Some studies (e.g., Spakman and Nolet, 1988; Michelini and McEvilly, 1991) employed synthetic data to estimate the errors and resolution of the inversion. In the following section, image fidelity in the LVC inversion is assessed using synthetic arrival time data and initial models with different node spacing.

The test model is derived from the starting 1-D velocity model used in the actual inversion (Figure 5.3) with high- and low-velocity anomalies (15 to 20% contrasts) superimposed on several nodes. The grid used to generate synthetic travel times contains 294 nodes spaced at 2.5 km (x7 nodes) horizontally and 2 km (x6 nodes) vertically. Depths are referenced to a datum plane 2 km above sea level, the average elevation of the region. Figure 5.4 presents the P-wave test model in a series of horizontal slices at several depths beneath LVC. The cross sections display a 15x15 km^2 area centered at the Resurgent Dome. Colors indicate velocities with blue and red indicating high and low values, respectively. The velocity distribution contains parallel ridges 3.5 km long of high and low velocity in the west central LVC at a depth of 4 km and several isolated high- and low-velocity anomalies at greater depth near the Resurgent Dome. This "heterogeneity" was introduced to evaluate the capability of the data set to resolve anomalies with varying scale lengths. A subset of 214 earthquakes and six refraction shots to 30 km distance provides a total of 5750 arrival times. The same source-receiver geometry was employed as for the real inversion problem.

Three parameterizations were adopted for the inversion tests: (1) a coarse grid with a node spacing along the x, y, and z directions of 10 km (x7 nodes), 10 km (x7 nodes), and 2 km (x6 nodes), respectively; (2) a medium grid with a node spacing of 5 km (x7 nodes), 5 km (x7 nodes), and 2 km (x6 nodes); and (3) a fine grid with a node spacing of 3 km (x7 nodes), 3 km (x7 nodes), and 2 km (x6 nodes). All three parameterizations have larger grid spacing than the generating model to simulate the effect of undersampling. The resulting models were evaluated on the degree to which

the different parameterizations reproduce the original synthetic structure and compare the rms residual and the model resolution of the three cases.

The model resolution matrix **R**, defined in $\mathbf{m} = \mathbf{R}\ddot{\mathbf{m}}$ shows how close a model estimate (**m**) is to a true model ($\ddot{\mathbf{m}}$). Ideally, the "true model" represents the real Earth structure in the absence of error and described by the model parameterization. Each element of the model estimate (**m**) is a weighted average of the data and a priori assumptions. The rows of **R** are the averaging kernels for each model parameter which describe how well neighboring model parameters are independently predicted (Menke, 1989). If **R** is the identity matrix, then each model parameter is uniquely determined. Since **R** is an (*mxm*) square matrix, where *m* is the number of model parameters, difficulties arise in displaying **R** even for modest *m* because of its large size. A more meaningful and compact form of presenting **R** uses the resolving-width function (RW_i) of the *i*th model parameter, as defined by Menke (1989), Toomey and Foulger (1989), and Michelini and McEvilly (1991)

$$\mathbf{RW}_i = \|\mathbf{r}_j\| \sum_j^m w(i,j)\mathbf{R}_{ij}^2 \qquad (1)$$

where R_{ij} is an element of **R**, *w(i,j)* is a weighting function equal to the distance between the *i*th and *j*th parameter, *m* is the number of model parameters, and $\|\mathbf{r}_j\|$ is the L^2 norm of the *j*th averaging kernel. A well-resolved model parameter has low RW_i, while a large value indicates a poorly resolved parameter with broad resolving-kernel shape. In addition to visual evidence for image recovery, the results are assessed by comparing the spatial variations of RW_i for the three parameterizations.

Velocity structures obtained for the different parameterizations are shown in Figures 5.4b, 5.4c and 5.4d. Three cross sections at depths of 4, 6, and 8 km are presented for each case. Colors denote seismic velocity with contour interval of 0.2 km/s. The resolution (indicated by RW_i) is depicted by the degree of color intensity,

Figure 5.4 Horizontal cross sections of the test P-wave velocity structure taken at several depths. The maps are centered on the Resurgent Dome at 37°40'N, 118°54'W. Datum plane is at 2 km above sea level. Colors denote velocity variations while intensity indicates model resolution as defined by the resolving width function RW_i. Contour interval is 0.2 km/s. (A) Plots of the starting velocity model used to generate the synthetic travel times. (B) Plots of the calculated P-wave synthetic velocity model for node spacing of 10 km horizontally and 2 km vertically (coarse grid). (C) Plots of the calculated P-wave synthetic velocity model for node spacing of 5 km horizontally and 2 km vertically (medium grid) (D) Plots of the calculated P-wave synthetic velocity model for node spacing of 3 km horizontally and 2 km vertically (fine grid).

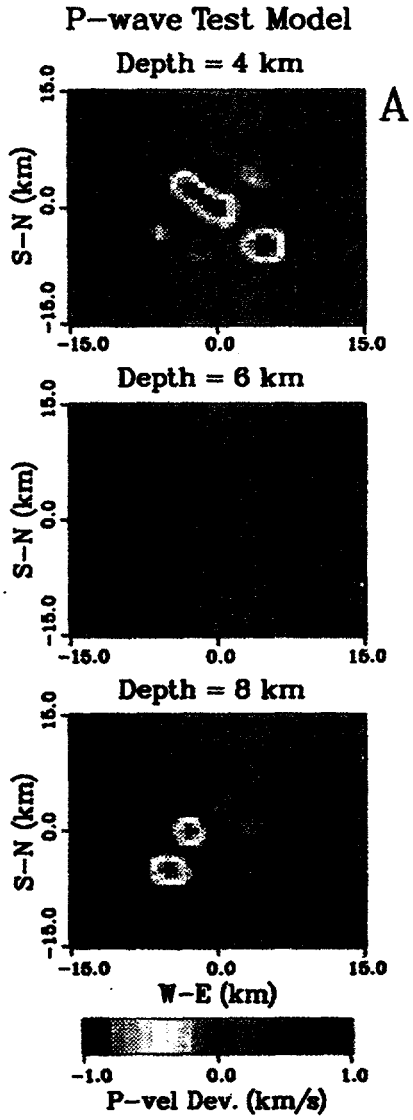
P–wave Test Model
Depth = 4 km
A
S–N (km)
15.0
0.0
-15.0
-15.0
0.0
15.0
Depth = 6 km
Depth = 8 km
W–E (km)
-1.0
0.0
1.0
P–vel Dev. (km/s)

Figure 5.4a

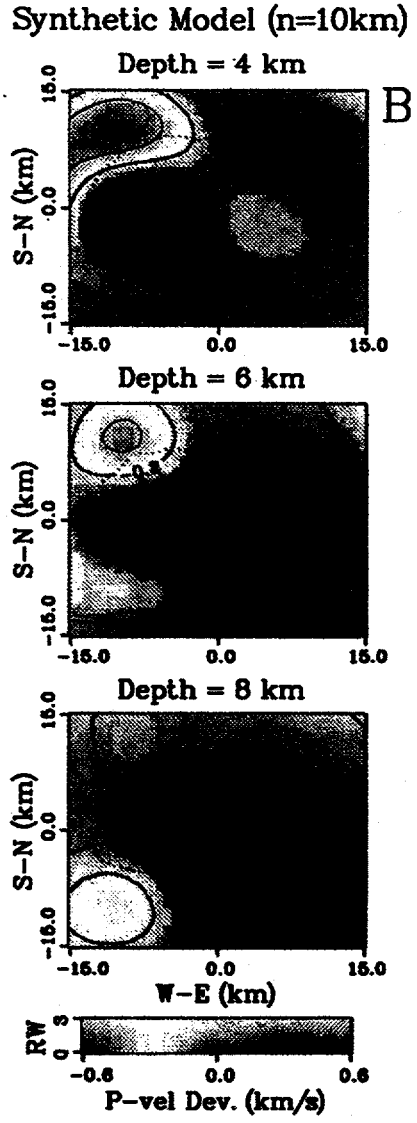
Synthetic Model (n=10km)
Depth = 4 km
B
Depth = 6 km
Depth = 8 km
S-N (km)
15.0
0.0
-15.0
W-E (km)
RW
-0.6
0.0
0.6
P-vel Dev. (km/s)

Figure 5.4b

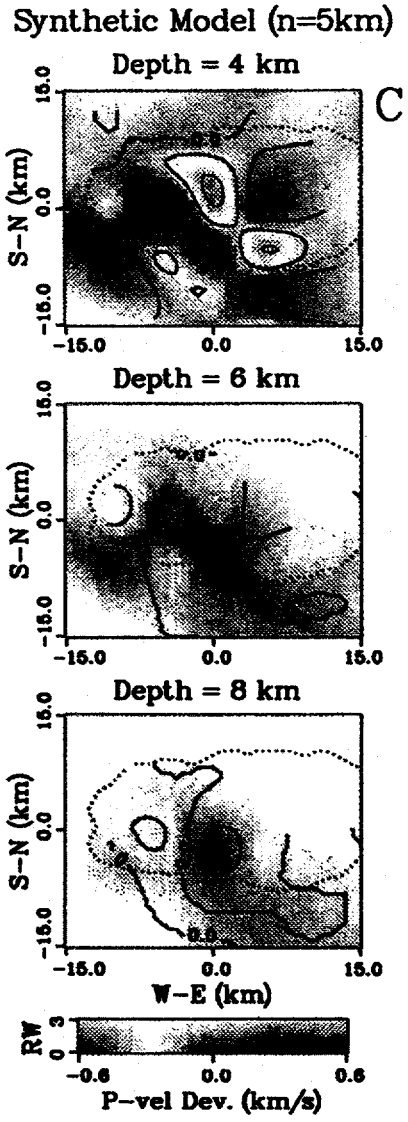
Synthetic Model (n=5km)
Depth = 4 km
C
S-N (km)
15.0
0.0
-15.0
Depth = 6 km
Depth = 8 km
W-E (km)
RW
-0.6
0.0
0.6
P-vel Dev. (km/s)

Figure 5.4c

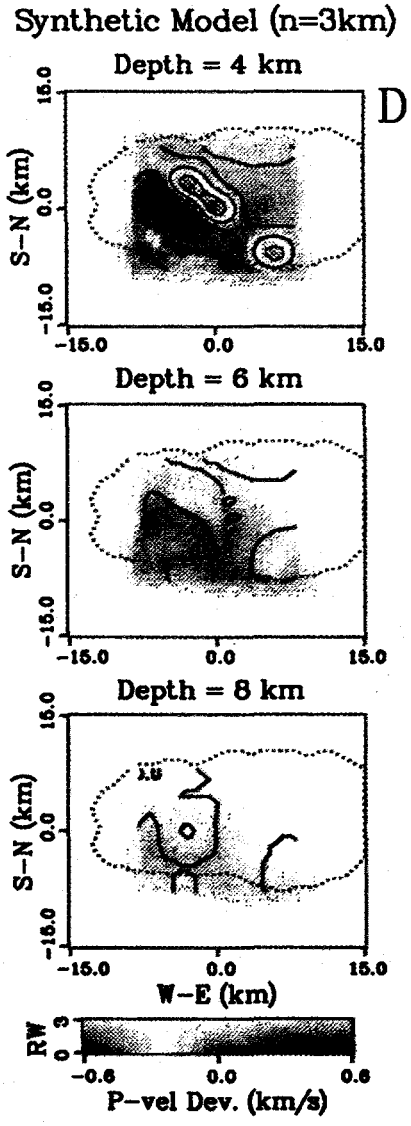
Synthetic Model (n=3km)
Depth = 4 km
D
Depth = 6 km
Depth = 8 km
S-N (km)
15.0
0.0
-15.0
W-E (km)
RW
-0.6
0.6
P-vel Dev. (km/s)

Figure 5.4d

e.g., low color intensity indicates low resolution (large RW_i).

The P-wave velocity structure in Figure 5.4b, obtained using the coarse grid (node spacing of 10 km), shows little resemblance to the test model. The ridge features at 4-km depth show up as a diffuse high-velocity anomaly shifted at least 5 km to west of its actual location. The features at 8-km depth similarly are represented as a broad high-velocity zone beneath the east central caldera. There is little indication of the low-velocity anomalies. Other features seen with scale lengths around 10 km appear to be totally unrelated to the initial test model.

Both fine and medium grids recover more details of the test model. The medium grid (node spacing of 5 km) inversion test, shown in Figure 5.4c, recovers more of the anomalies in the P-wave structure. The anomaly ridges at 4-km depth are beginning to take shape. Distorted images of the anomalous high- and low-velocity features at 8-km depth are seen, and they apparently are influencing results at the 6-km level. Velocity anomalies, with ±5% variations unrelated to the initial model are present in regions of low resolution in the southwest and northeast quarters of LVC.

The most prominent features recovered with the fine grid (node spacing of 3 km) are the parallel ridges of high and low velocity in the west central LVC at 4-km depth (Figure 5.4d). Good resolution is obtained only in the western half of LVC. The two isolated high-velocity bodies northeast of these ridges are seen as a single diffuse anomaly. The anomalies at 8-km depth are not recovered, although there is evidence for their influence at 6-km depth.

It is clear that the fine and the medium grids yield the best results in well-resolved regions which are adequately sampled by seismic rays. However, because of poorly sampled nodes the fine grid has relatively large regions of low resolution compared to both the medium and the course grids. While the coarse grid provides the best resolution, owing to the fact that a fairly large number of rays are sampled and contribute to the prediction of each of the velocity parameters, it presents the poorest

recovery of the original model. For this data set then, the medium grid represents the optimum node spacing for relatively good resolution over the region of interest, while still preserving some small-scale features. The medium grid was adopted for the inversion of the real arrival time data.

These tests with synthetic data have shown that the caldera region is well-resolved to a depth of 8 km and velocity fluctuations less than 6% are insignificant. Furthermore, it is concluded that the inverse problem as posed can define heterogeneity with scale lengths of 2.5 km within well-resolved regions, sufficient to test the various magma chamber hypotheses.

5.6 Final Inversion Model and Interpretation

The final model, based on 280 well-distributed local earthquakes, exhibits an rms arrival time residual of 71 ms, an improvement of 42% after two iterations. The resulting Vp and Vs models are shown in Figures 5.5 and 5.6, with the resolving-width function (RW_i) superimposed as color intensity to indicate regions of low resolution. The Vp model is well-resolved to a depth of 8 km within the caldera. Vs is not well-resolved in the eastern part of the caldera where there are no three-component stations, but elsewhere Vs is well-resolved to a depth of 8 km. The important target region beneath the Resurgent Dome and the West Moat, where the proposed magma bodies lie, is well-imaged for both Vp and Vs.

5.6.1 Vp Structure

The most striking feature in the velocity structure is the lateral velocity variation in the upper 2 km, presumably due to the postcaldera fill contrast with the surrounding

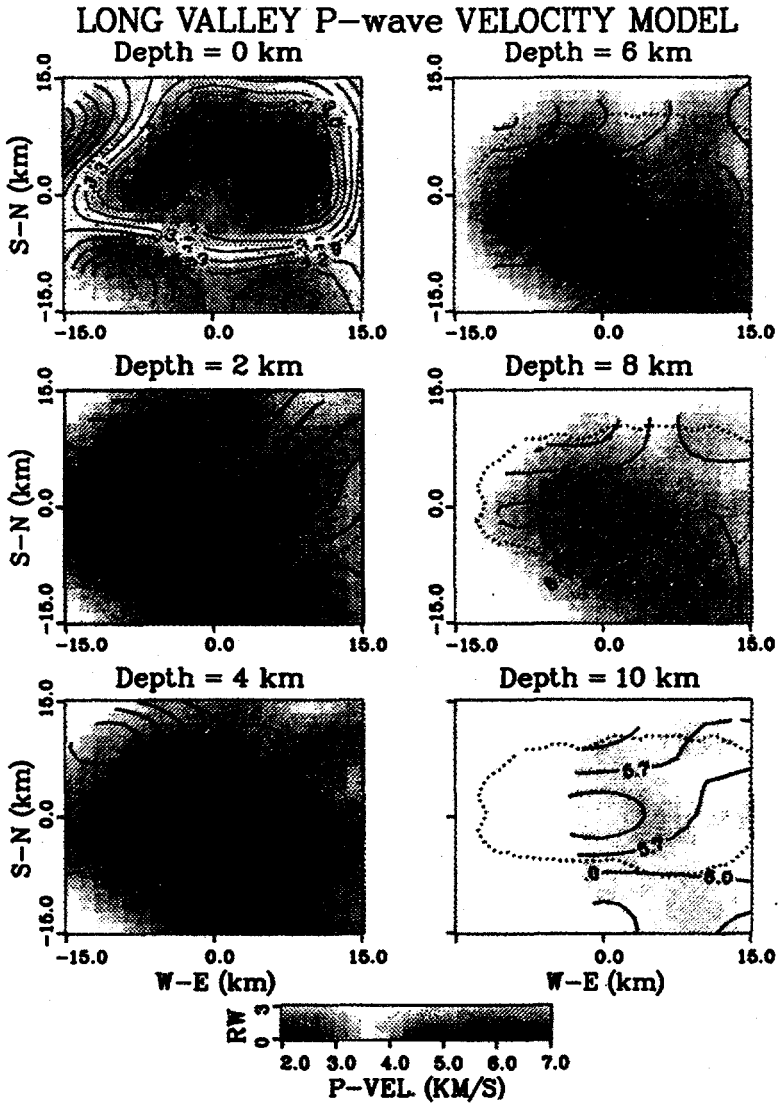

Figure 5.5 Plots of the final P-wave velocity model. Colors denote velocities, while intensity indicates model resolution as given by the resolving width function RW_i. Contour interval is 0.3 km/s. Datum plane is at 2 km above sea level.

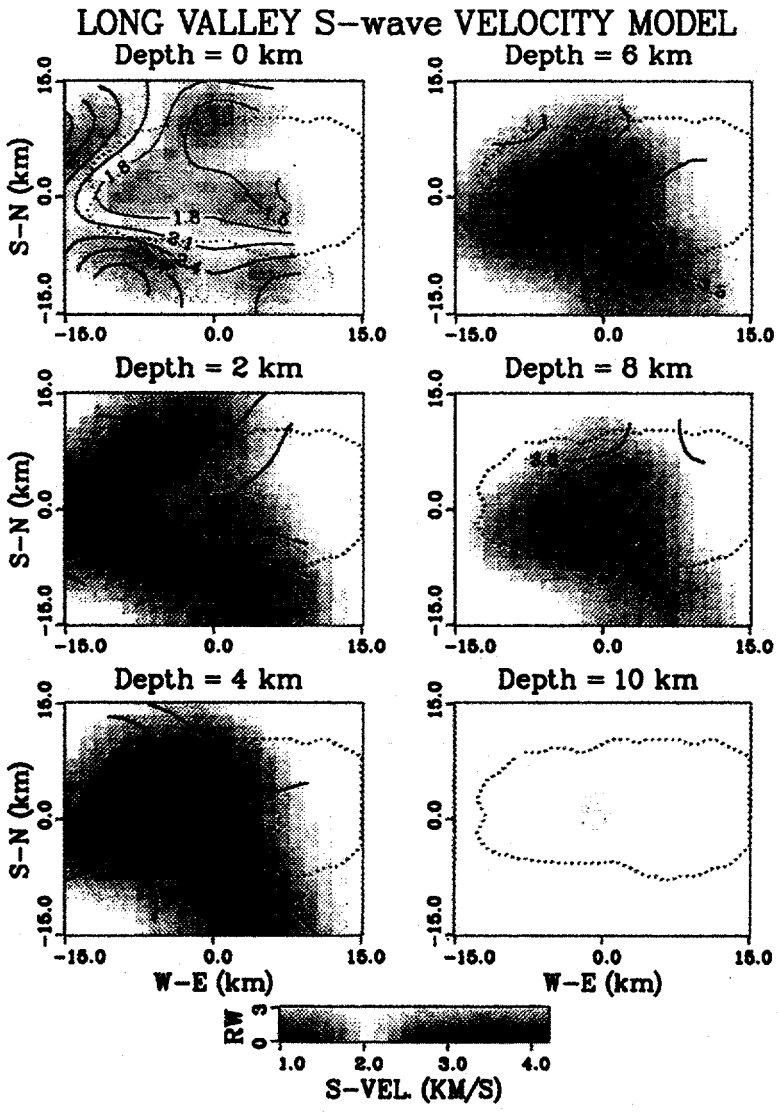

Figure 5.6 Plots of the final S-wave velocity model. Colors denote velocities, while intensity indicates model resolution as given by the resolving width function RW_i. Contour interval is 0.3 km/s. Datum plane is at 2 km above sea level.

rocks. Vp ranges from about 2.5 km/s in the postcaldera fill to above 4 km/s in the surrounding terranes with steep velocity gradients at the caldera ring faults. At a depth of 2 km the caldera is still evident as an oval structure within which Vp increases westward from 5 km/s at the eastern boundary to 6 km/s at the west moat. The velocity structure becomes more uniform below a depth of 2 km. Although the velocities beneath the caldera are somewhat lower than those in the surrounding regions, there seems to be no evidence of distinct small-scale low-velocity zones to 8 km at the inversion resolution of about 2.5 km. A diffuse low-velocity region is seen east and southeast of the Resurgent Dome from depths of 2 to 6 km, bounded to the southwest by a trend roughly in line with the projection of the Hilton Creek and Round Valley faults into the caldera (refer to Figure 5.1). At a depth of 8 km, a low-velocity region appears beneath the southwest part of the caldera.

5.6.2 Vs and Vp/Vs Structures

The Vs structure (Figure 5.6) generally shows those variations seen for Vp. Resolution is lower due to the much reduced ray coverage for S-waves. The Vp/Vs structure in Figure 5.7 displays intriguing features. Most striking is the relatively high Vp/Vs (greater than 1.8) within the caldera near Casa Diablo, separating regions of low Vp/Vs (less than 1.6) to the northwest and southeast. These two zones of low Vp/Vs appear to merge at depths of 4 to 6 km into a broad low, lying beneath the southwestern caldera and bounded on the east by the projection of the Hilton Creek fault.

5.6.3 Lithological Interpretation of Velocities

The Vp model is consistent with the upper crustal structure determined by Hill et al. (1985b). The caldera fill, discernible to a depth of 2 km, generally thickens

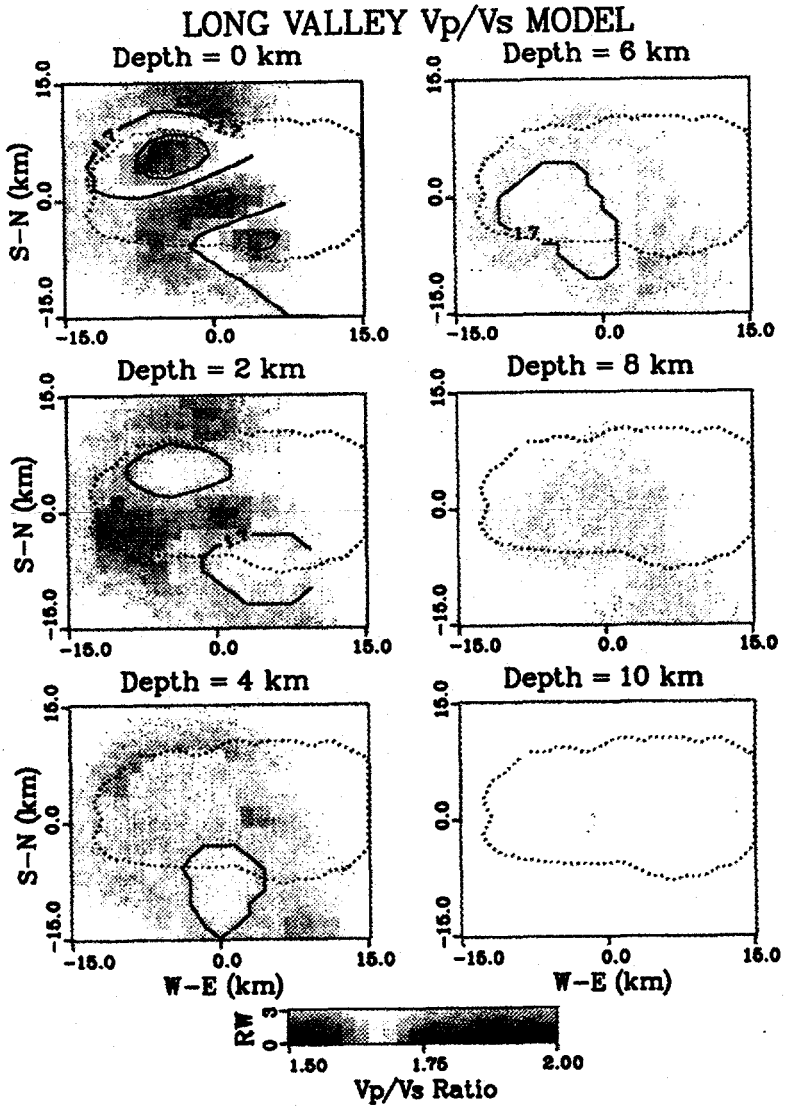

Figure 5.7 Plots of the final Vp/Vs structure. Colors denote Vp/Vs values, while intensity indicates model resolution as given by the resolving width function RW_i. Contour interval is 0.1. Datum plane is at 2 km above sea level.

northward and eastward, from about 1 km thickness beneath the west moat to about 2 km thickness beneath the east moat. The welded Bishop tuff comprises roughly the lower half of the fill. The Resurgent Dome is evident as a thinning of the postcaldera fill at the central part of the caldera. The Inyo volcanic chain and Mammoth Mountain, northwest and southwest of the caldera, respectively, are characterized by lower velocities, probably associated with pumice and fractured rhyolite flows. Lower velocities extend southeast of the caldera into the Volcanic Tableland which consists of relatively low-density Bishop tuff.

The velocities found in the upper 2 km correspond well to the rock units of the caldera fill and their associated P- and S-wave velocities as summarized by Bailey et al. (1976) and Hill et al. (1985b): (1) a surficial layer of poorly-consolidated sedimentary fill, and basalt and rhyolite lava flows with thickness of 100-300 m and velocities less than 2 km/s (Vp) and 1.0 km/s (Vs); (2) postcaldera volcanics consisting of tuffs and rhyolite lava flows, and partly-welded Bishop tuff with thickness of 200-400 m and velocities between 2.0 and 4.0 km/s (Vp) and 1.0 and 2.2 km/s (Vs); and (3) welded Bishop tuff with thickness of roughly 1 km and velocities between 4.0 and 4.5 km/s (Vp) and 2.3 and 2.6 km/s (Vs). Velocity-lithology relations in the caldera will depend heavily on the specific geothermal environment. The presence of fractures and hydrothermal alteration within the caldera fill will complicate lithological distinctions. For example, velocities for the welded Bishop tuff within the caldera are comparable to the velocities of the granitic and metasedimentary rocks in the upper 2 km of the crystalline basement.

The caldera and the surrounding highlands are underlain by crystalline basement of Mesozoic granite, Paleozoic metasedimentary and metavolcanic rocks (Bailey et al., 1976), with velocities starting at the upper levels around 5 km/s (Vp) and 3 km/s (Vs). Model P- and S-wave velocities of at least 6 and 3.5 km/s are seen at a depth of 6 to 8 km. Location of the higher velocities at the western caldera margin suggests that the

main caldera ring fault there extends roughly 3 km inward from the topographic boundary as confirmed by drilling in the west moat near Inyo domes (Suemnicht, 1987). This feature suggests that the west moat subsidence may have been accomplished in a series of normal faults.

5.6.4 Implications of the Vp/Vs Structure

Fractures, pore pressure, porosity, fluid saturation, and partial melt affect seismic velocities. Variations in the observed Vp/Vs ratio, along with the P- and S-wave velocities, indicate changes in the mechanical properties of the rocks in situ. Moos and Zoback (1983) found that the presence of fully saturated fractures decreases both P- and S-wave velocities, and increases Vp/Vs. Christensen (1984) demonstrated that Vp/Vs values increase with pore pressure at constant confining pressure. In a theoretical study, Mavko (1980) showed that partial melting increases the Vp/Vs ratio. The P-wave velocity of porous rocks has been shown theoretically and experimentally to be more sensitive to fluid saturation changes than the S-wave velocity (Castagna et al., 1985; O'Connell and Budiansky, 1974, 1977). The effect of fluids in joints is to increase the specific stiffness to compressional waves while not inhibiting the relative shear displacement across the joint. As a result, higher saturation increases the effective Vp/Vs while undersaturation (dry or gas-filled fractures) depresses the effective Vp/Vs ratio (Toksöz et al., 1976; Gregory, 1976).

Following O'Connell and Budiansky (1974), the degree of fluid saturation is estimated to first order from the observed Vp/Vs ratio obtained from the inversion. Using a self-consistent approximation, the equations relating seismic velocities and saturation for the case of randomly-oriented elliptical cracks partially saturated with fluid and gas phases are:

$$\frac{\overline{Vp/Vs}}{Vp/Vs} = \left(\frac{(1-\overline{\upsilon})(1-2\upsilon)}{(1-2\overline{\upsilon})(1-\upsilon)} \right)^{\frac{1}{2}} \tag{2}$$

$$\varepsilon = \frac{45(\upsilon - \overline{\upsilon})(2-\upsilon)}{16(1-\overline{\upsilon}^2)\left[(1-\xi)(1+3\upsilon)(2-\overline{\upsilon}) - 2(1-2\upsilon)\right]} \tag{3}$$

where

$\overline{Vp/Vs}$ observed Vp/Vs ratio;

Vp/Vs intact rock Vp/Vs ratio;

$\overline{\upsilon}$ observed Poisson's ratio;

υ intact rock Poisson's ratio;

ξ fluid saturation;

ε crack density, defined as $\varepsilon = (2N/\pi)\langle A^2/P \rangle$, where N is the number of cracks per unit volume; A and P are the area and the perimeter of the crack, respectively.

A Vp/Vs ratio of 1.73 was assumed for the dry uncracked rock. The crack density ε may be obtained from estimating the number of cracks traces per unit area and the mean trace length in cores or thin sections. In the absence of a reliable measurement of the crack density, bounds can only be placed on the estimated saturation values. These bounds are based on all elastic moduli approaching zero with increasing crack density. Examination of several well logs taken from several boreholes around the Resurgent Dome region indicates numerous cracks of various sizes and orientations, attesting to the highly fractured conditions of the rocks beneath LVC at shallow depths. In addition, large cracks reduce the elastic moduli more than a great number of small cracks with the same total crack area (O'Connell and Budiansky, 1974). Using these equations, an upper bound in saturation value of 0.53 and 0.41 at shallow depths beneath the South Moat and the West Moat, respectively is estimated. The isolated high Vp/Vs anomaly near Casa Diablo has saturation greater than 0.73. For the low Vp/Vs

beneath the western part of the caldera at a depth of 4 km, the saturation is less than 0.63. How these results extrapolate to macrofractures is not well known, as complications due to fracture distribution and orientation could not be neglected.

The relatively low saturation beneath the western caldera may suggest the presence of undersaturated fractures with a relatively high gas content, perhaps a combination of steam and noncondensible gases, which may indicate a hot water upflow zone. This feature and its depth extent is consistent with current geothermal models in which the upflow zone is located beneath the west moat. The eastward extent of this flow is probably limited by a fault striking northwest-southeast, possibly the Hilton Creek fault. Curiously, no anomaly is seen beneath the Resurgent Dome. Sorey et al. (1991), integrating drill hole, chemical, geological, and geophysical data, propose that the roots of the present-day geothermal system, including the source reservoir and associated upflow zone, lie within the basement rocks beneath the western part of the caldera and that the heat source is most likely derived from the same heat source that drove the volcanic and phreatic eruptions along the Mono-Inyo volcanic chain. This is further supported by a magnetotelluric survey across Long Valley (Wannamaker et al., 1991; Sorey et al., 1991) which shows a region of low resistivity 5 km beneath the west moat and may represent a zone of hydrothermal fluids released from magma crystallization.

High values of Vp/Vs ratio may be indicative of saturated fractures. At The Geysers, Calif. geothermal region, O'Connell and Johnson (1991) found high Vp/Vs in the zone of maximum steam production, where fracture density is presumed to be maximum. The Vp/Vs high near Casa Diablo may indicate fully saturated fractures possibly due to the injection of geothermal fluids within the area.

5.7 Summary and Conclusions

The P- and S-wave velocities obtained in this study provide reasonably well constrained values in the central caldera to a depth of 8 km. Diffuse low-velocity regions are seen within and beneath the caldera. Absence of a significant S-wave velocity anomaly and the presence of normal or low values of Vp/Vs at the location of the proposed magma body beneath the Resurgent Dome argue against the presence of a sizable and distinct magma body at shallow to midcrustal depths beneath Long Valley caldera. These results are in agreement with the conclusion of Kissing (1988) on the lack of evidence for a pervasive low-velocity body at shallow crustal depths. The generally low velocities within the caldera are most likely related to hydrothermal alteration and extensive fracturing, rather than to the presence of a magma chamber.

Our results, however, do not rule out the presence of discrete dike or sill intrusions of melt with dimensions below the spatial resolution of this study and that do not block the propagation of high-frequency S-waves. Likewise, the possibility of a diffuse partial melt cannot be eliminated entirely, which is permitted at a fractional volume allowed by the Vp/Vs values. The effects of partial melt on seismic wave velocities are poorly known, so that it is difficult to estimate a permitted melt fraction from our data. The theoretical work of Mavko (1980) would indicate that the Vp/Vs ratio of 1.6-1.7 seen at 4 to 8 km beneath the caldera constrains the melt fraction to a few percent at most, if the melt is largely in a film configuration.

The extensive Vp/Vs low at shallow depths beneath the West Moat and its deep extent supports the current geothermal model for Long Valley caldera in which the hot water upflow zone is located beneath the west moat. The Vp/Vs high near Casa Diablo suggests fully saturated fractures, possibly due to activities associated with geothermal power generation in the area which exploits a substantial lateral flow of hot water from the west, ponded by the local fault system.

This exercise shows that the microearthquake data set from the available station distribution (including the special fan array and the three-component data) constitutes a fairly well-conditioned inverse problem, capable of resolving isolated discrete velocity anomalies with dimensions 2-3 km to a depth of about 8 km. The presence of a well-defined magma chamber between 4 and 8 km depth is not supported in this tomographic study, although the presence of magma in a pervasive set of fractures is allowed if the total melt fraction remains small enough to permit the Vp/Vs ratio of 1.6-1.7 at 8 km depth.

Chapter 6

REVIEW OF CONCLUSIONS

The main purpose of this study was to explore the utility of microearthquake data sets in characterizing geothermal reservoirs. There were two broad areas of investigation: the problem of describing the reservoir volume with the seismic-wave energy released in microearthquakes by estimating the seismic velocity and differential attenuation using tomographic reconstruction methods; and the analysis of the spatial and temporal patterns of seismicity as they reveal geothermal processes occurring in the reservoir. The two studies have obvious overlap, and both require high quality data from high-resolution networks with multi-component stations. Two state-of-the-art networks furnished data for this investigation. The Northwest Geysers microearthquake data set used in the study was acquired by a 16-station three-component seismic network in place at the Coldwater Creek Steam Field (CCSF). At the Long Valley Caldera study, a fan array of eight three-component borehole receivers was installed on the northwestern rim of the caldera to complement the existing U.S. Geological Survey and the University of Nevada at Reno seismic networks. The purpose of the fan array was to provide added ray path coverage in and below the Resurgent Dome, in the region of the proposed magma chamber, from microearthquake sources to the southeast. This configuration also allowed imaging of the active geothermal system beneath the western moat of the caldera.

Results of this study establish the significance of microearthquake data in geothermal reservoir definition. At the Northwest Geysers, observed velocity and attenuation variations exhibit correlations with the known geology of the field. High-velocity anomalies are associated with mapped sections of Franciscan metagraywacke and greenstone. Low-velocity anomalies correspond to Franciscan melange units and

poorly-consolidated basalt flows. Near-surface low P-wave attenuation anomalies at the southern and southeastern sections of CCSF also correlate with Franciscan metagraywacke and greenstone units while high attenuation anomalies correspond to the Franciscan melange. Stations located within the metagraywacke exposures tend to transmit higher frequencies than those located in melange units. Near-surface high attenuation and high Vp/Vs, especially around the Squaw Creek area west of the CCSF, appear to be related to liquid-saturated regions of meteoric recharge.

The velocity and differential attenuation structures correlate with the known steam producing zone. High P-wave and S-wave attenuation anomalies ($Q_p^{-1} > Q_s^{-1}$) below 1 km depth at the southern region of the field spread northwestward with depth following the fall of the steam zone in that direction. Low Vp/Vs also correlates with the spatial extent of the steam reservoir between depths of 1 and 3 km. Both the high P-wave attenuation and the low Vp/Vs anomaly appear to reflect undersaturation of the reservoir rocks. The spatial extent of both the high Q_p^{-1}/Q_s^{-1} and the low Vp/Vs anomalies seem to indicate the presence of steam northwest of the known geothermal limits at increasing depths (at least 3 km) which may indicate a potential extension of the geothermal resource, and further studies could better define the extent the steam reservoir northward, although seismicity appears to decrease in the region, perhaps degrading potential tomographic resolution.

At the Long Valley Caldera, the absence of a significant S-wave velocity anomaly and the presence of low to normal Vp/Vs preclude the existence of a distinct magma body at shallow crustal depths. The study does not rule out the presence of small dike intrusions with dimensions below the spatial resolution of this study, or the possibility of a diffuse partial melt of as much as a few percent melt. The extensive low Vp/Vs beneath the West Moat is likely related to hydrothermal alteration and extensive fracturing related to the active geothermal system beneath the western part of the caldera. The Vp/Vs high near Casa Diablo suggests fully saturated fractures, possibly related to

geothermal power generation in the area which exploits a substantial lateral flow of hot water from the west.

The study on improved spatial and temporal patterns of microearthquakes provides strong evidence for injection-induced seismicity at The Northwest Geysers. A cluster of microearthquakes at the bottom of an active injection well extends several hundred meters below it, and the spatial distribution of hypocenters seems to define a vertical planar structure oriented north-south. The seismicity rate responds to changes in the injection history, with the highest activity recorded during peaks in the injection rate. Increase in pore pressure leading to decrease in effective normal stress is the likely mechanism for inducing seismicity. Injection seismicity is superimposed on a more diffuse pattern of shallow seismicity that is probably related to steam withdrawal. Microearthquakes are concentrated within the main steam producing zone and are virtually absent where the field is not yet exploited. The hypocenters deepen to the north, consistent with the deepening steam reservoir in that direction. The likely mechanisms for production-induced seismicity include volumetric contraction, fracture deflation, thermal contraction and stick-slip enhancement, in response to either a reduction in pore pressure or an increase in friction due to silica precipitation.

The analysis of high-resolution microearthquake data represents a promising tool for geothermal reservoir delineation and for monitoring changes in reservoir properties with time. The extent of velocity and attenuation anomalies probably reflect the size and extent of a potential geothermal resource. Slowly occurring processes could be monitored with, e.g., yearly data inversions. Changes detected in the temporal and spatial distribution of microearthquakes may indicate reservoir volume changes associated with fluid withdrawal and injection. High resolution microearthquake locations hold promise for inferring fluid flow paths, especially in tracking injection fluids. Finally, the overall distribution of seismicity appears to map the region that is affected hydraulically by both fluid withdrawal and injection.

This study has demonstrated that seismic monitoring, with proper sampling in space and time, may be useful as an active reservoir monitoring tool. Refinements of the methods presented here and the addition of future case histories could make seismic methods an essential tool in geothermal reservoir definition and management.

REFERENCES

Aki, K. and Lee, W. H. K. (1976) Determination of three-dimensional velocity anomalies under a seismic array using first P arrival times from local earthquakes, I, A homogeneous initial model, *J. Geophys. Res.*, **81**, 4381-4399.

Allis, R. G. (1982) Mechanism of induced seismicity at The Geysers geothermal reservoir, California. *Geophys. Res. Let.* **9**, 629-632.

Anderson, D. L., Ben-Menahem, A. and Archambeau, C. B. (1965) Attenuation of seismic energy in the upper mantle, *J. Geophys. Res.*, **70**, 1441-1448.

Backus, G. E. and Gilbert, F. (1967) Numerical application of a formalism for geophysical inverse problems, *Geophys. J. Roy. Astron. Soc.*, **13**, 247-276.

Bailey, R. A., Dalrymple, G. B. and Lanphere, M. A. (1976) Volcanism, structure, and geochronology of Long Valley caldera, Mono County, California, *J. Geophys. Res.*, **81**, 725-744.

Bailey, R. A. (1989) Geologic map of Long Valley caldera, Mono-Inyo volcanic chain, and vicinity, *U.S. Geol. Surv. Misc. Invest. Map I-1933.*.

Barker, B. J., Gulati, M.S., Bryan, M.A., Riedel, K. L. (1992) Geyser reservoir performance. *Geother. Res. Council Special Report No. 17*, 167-177.

Batini, F., Console, R. and Luongo, G. (1985) Seismological study in Larderello-Travale geothermal area. *Geothermics*, **14**, 255-272.

Black, R. A., Deemer, S. J. and Smithson, S. B. (1991) Seismic reflection studies in Long Valley caldera, California, *J. Geophys. Res.*, **96**, 4289-4300.

Blake, M. C. and Jones, D. L. (1974) Origin of Franciscan melanges in Northern California. *Society of Economic Paleontologists and Mineralogists Special Pub. 19*, 345-357.

Brune, J. N. (1970) Tectonic stress and the spectra of seismic shear waves from earthquakes. *J. Geophys. Res.* **75**, 4997-5009.

Carmichael, R. S. (1982) *Handbook of Physical Properties of Rocks Vol. II.* CRC Press, Boca Raton, Florida.

Castagna, J. P., Batzle, M. L. and Eastwood, R. L. (1985) Relationships between compressional-wave and shear-wave velocities in clastic silicate rocks, *Geophysics,* **50**, 571-581.

Chatterjee, S. N., Pitt, A. M. and Iyer, H. M. (1985) Vp/Vs ratios in the Yellowstone National Park region, Wyoming. *J. Volcanol. Geotherm. Res.*, **26**, 213-230.

Christensen, N. I. (1986) Influence of pore pressure on oceanic crustal seismic velocities, *J. Geodynam.*, **5**, 45-49.

Christensen, N. I. (1984) Pore pressure and the oceanic crustal seismic structure, *Geophys. J. R. Astron. Soc.,* **79**, 411-423.

Christensen, N. I. and Wepfer, W. W. (1989) Laboratory techniques for determining seismic velocities and attenuations, with applications to the continental lithosphere, *Geol. Soc. Am. Memoir*, **172**, 91-102.

Clawson, S. R., Smith, R. B. and Benz, H. M. (1989) P-wave attenuation of the Yellowstone Caldera from three-dimensional inversion of spectral decay using explosion source seismic data. *J. Geophys. Res.*, **94**, 7205-7222.

Cranswick, E., Wetmiller, R. and Boatwright, J. (1985) High-frequency observations and source parameters of microearthquakes recorded at hard rock sites. *Bull. Seismol. Soc. Am.* **75**, 1535-1576.

Crosson, R. S. (1976) Crustal structure modelingof earthquake data, I, Simultaneous least squares estimation of hypocenter and velocity parameters, *J. Geophys. Res..*, **81**, 3036-3046.

Dawson, P. B., Evans, J. R. and Iyer, H. M. (1990) Teleseismic tomography of the compressional wave velocity structure beneath the Long Valley region, California, *J. Geophys. Res.*, **95**, 11,021-11,050.

Denlinger, R. P. and Bufe, C. G. (1982) Reservoir conditions related to induced seismicity at The Geysers steam reservoir, Northern California. *Bull. Seismol. Soc. Am.* **72**, 1317-1327.

Denlinger, R. P. (1980) Seismicity induced by steam production at The Geysers steam field in northern California, *Eos Trans. AGU,* **61**, 1051.

Diment, W. H. (1980) Geology and geophysics of geothermal areas. *A sourcebook on the production of electricity from geothermal energy*, Kestin, J., Pippo, R. D., Khalifa, H. E. and Ryley, D. W. (eds.), US Gov't Printing Office.

Duffield, W. A., Sass, J. H. and Sorey, M. L. (1994) Tapping the Earth's natural heat. *USGS Circular 1125.*

Eberhart-Phillips, D. (1986) Three-dimensional velocity structure in Northern California Coast Ranges from the inversion of local earthquakes. *Bull. Seismol. Soc. Am.* **76** , 1025-1052.

Eberhart-Phillips, D. and Oppenheimer, D. H. (1984) Induced seismicity in The Geysers geothermal area, California. *J. Geophys. Res.* **89**, 1191-1207.

Evans, J. R. and Zucca, J. J. (1988) Active high-resolution seismic tomography of compressional wave velocity and attenuation structure at Medicine Lake volcano, northern California Cascade Range. *J. Geophys. Res.* **93**, 15,016-15,036.

Evans, J. R. and Zucca, J. J. (1992) Active high-resolution compressional wave attenuation tomography at Newberry volcano, Central Cascade Range. *J. Geophys. Res.* **97**, 11,047-11,055.

Foxall, W. (1992) *Heterogeneous slip and rupture models of the San Andreas fault*

zone based upon three-dimensional earthquake tomography, Ph.D. Thesis, Dept. of Geol. and Geophys., Univ. of Calif., Berkeley.

Frankel, A. (1982) The effects of attenuation and site response on the spectra of microearthquakes in the northeastern Caribbean. *Bull. Seismol. Soc. Am.* **72,** 1379-1402.

Frankel, A. and Clayton, R. W. (1984) A finite difference simulation of wave propagation in two-dimensional random media. *Bull. Seismol. Soc. Am.* **74,** 2167-2186.

Frankel, A. and Clayton, R. W. (1986) Finite difference simulations of seismic scattering: Implications for the propagation of short-period seismic waves and models of crustal heterogeneity. *J. Geophys. Res.*, **91**, 6465-6489.

Frankel, A. and Wennerberg, L. (1989) Microearthquake spectra from the Anza, California, seismic network: Site response and source scaling. *Bull. Seismol. Soc. Am.* **76**, 2167-2186.

Goldstein, N. E. (1988) Pre-drilling data review and synthesis for the Long Valley caldera, California, *Eos Trans. AGU,* **69**, 43-45.

Goldstein, N. E., and Stein, R. S. (1988) What's new at Long Valley, *J. Geophys. Res.,* **93**, 13,187-13,190.

Grant, M. A., Donaldson, I. G. and Bixley, P. F. (1982) *Geothermal Reservoir Engineering*, Academic Press, New York, New York.

Gregory, A. R. (1976) Fluid saturation effects on dynamic elastic properties of sedimentary rocks. *Geophysics*, **41**, 895-921.

Hamilton, R. M. and Muffler, L. J. P. (1972) Microearthquakes at The Geysers geothermal area, California, *J. Geophys. Res.*, **77**, 2081-2086.

Hanks, T. C. (1982) f_{max}. *Bull. Seismol. Soc. Am.* **72**, 1869-1879.

Haukkson, E. (1988) Absence of evidence for a shallow magma chamber beneath Long Valley caldera, California, in downhole and surface seismograms, *J. Geophys. Res.*, **93**, 13,251-13,264.

Healy, J. H., Rubey, W. W., Griggs, D. T. and Raleigh, C. B. (1968) The Denver earthquakes. *Science*, **161**, 1301-1310.

Hebein, J. J. (1983) Exploration, drilling, and development operations in the Bottle Rock area of The Geysers steam field, with new geologic insights and models defining reservoir parameters. *Proc. 9th Workshop on Geothermal Reservoir Engineering*, Stanford University, California, 135-144.

Hebein, J. J. (1986) Conceptual schematic geologic cross-sections of The Geysers steam field. *Proc. 11th Workshop on Geothermal Reservoir Engineering*, Stanford University, California, 251-257.

Hill, D. P. (1976) Structure of Long Valley caldera from seismic refraction experiments, *J. Geophys. Res.*, **81**, 745-753.

Hill, D. P., Bailey, R. A. and Ryall, A. S. (1985a) Active tectonic and magmatic processes beneath Long Valley caldera, eastern California: An overview, *J. Geophys. Res.*, **90**, 11,111-11,120.

Hill, D. P., Kissling, E., Luetgert, J. H. and Kradolfer, U. (1985b) Constraints on the upper crustal structure of the Long Valley-Mono craters volcanic complex, eastern California, from seismic refraction measurements, *J. Geophys. Res.*, **90**, 11135-11150.

Hirn, A. and Ferucci, F. (1985) P and S arrival time anomalies at a dense array: Marker of the Travale field, *Geothermics*, **14**, 713-722, 1985.

Hubbert, M. K. and Rubey, W. W. (1959) Role of fluid pressure in mechanics of overthrust faulting, *Geol. Soc. Am. Bull.*, **70**, 115-116.

Hulen, J. B. and Walters, M. A. (1993) The Geysers felsite and associated geothermal systems, alteration, mineralization and hydrocarbon occurrences.

Guidebook series, Soc. of Economic Geol., **16**, 141-152.

Johnston, D. H. and Toksöz, M. N. and Timur, A. (1979) Attenuation of seismic waves in dry and saturated rocks: II Mechanisms, *Geophysics*, **44**, 691-711.

Johnston, D. H. and Toksöz, M. N. (1980) Ultrasonic P- and S-wave attenuation in dry and saturated rocks under pressure. *J. Geophys. Res.*, **85**, 925-936.

Julian, B. R., Prisk, A., Foulger, G. R. and Evans, J. R. (1993) Three-dimensional images of geothermal systems: Local earthquake P-wave velocity tomography at the Hengill and Krafla geothermal areas, Iceland, and The Geysers, California. *Trans. Geother. Resour. Counc.* **17**, 113-121.

Kampfmann, W. and Berckhemer, H. (1985) High temperature experimentson the elastic and anelastic behavior of magmatic rocks, *Phys. Earth Planet. Int.*, **40**, 223-247.

Kissling, E. (1988) Geotomography with local earthquake data, *Rev. Geophys.*, **26**, 659-698.

Kisslinger, C. (1976) A review of theories of mechanisms of induced seismicity. *Engineering Geology* , **10**, 85-98.

Lees, J. M. and Lindey, G. T. (1994) Three-dimensional attenuation tomography at Loma Prieta: Inversion of t* for Q. *J. Geophys. Res.* **99**, 6843-6863.

Lin, W. and Wang, C. Y. (1980) P-wave velocity in rocks at high pressure and temperature and the constitution of the central California crust. *Geophys. J. R. Astron. Soc.* **61**, 379-400.

Ludwin, R. S. and Bufe, C. G. (1980) Continued seismic monitoring of The Geysers, California geothermal field. *USGS Open File Report 80-1060.*

Luetgert, J. H., and Mooney, W. D. (1985) Crustal refraction profile of Long Valley caldera, California, from the January 1983 Mammoth Lakes earthquake swarm, *Bull. Seismol. Soc. Am.*, **75**, 211-221.

Majer, E. L. and McEvilly, T. V. (1979) Seismological investigations of The Geysers geothermal field. *Geophysics* **44**, 246-269.

Mavko, G. M. (1980) Velocity and attenuation in partially molten rocks, *J. Geophys. Res.*, **85**, 5173-5189.

Mavko, G. M. and Nur, A. (1979) Wave attenuation in partially-saturated rocks, *Geophysics* **44**, 161-178.

McGarr, A. (1976) Seismic moments and volume changes, *J. Geophys. Res.*, **81**, 1487-1494.

McLaughlin, R. J. (1981) Tectonic setting of pre-Tertiary rocks and its relation to geothermal resources in The Geysers-Clear Lake area, Research in The Geysers-Clear Lake Geothermal area, northern California. *USGS Professional Paper 1141.*

McNitt, J. R. (1968) Geology of the Keyserville quadrangle. *Map sheet 9, Calif. Div. Mines and Geol.*

McNitt, J. R., Henneberger, R. C., Koenig, J. B. and Robertson-Tait, A. (1989) Stratigraphic and structural controls of the occurrence of steam at The Geysers. *Trans. Geother. Resour. Counc.* **13**, 461-465.

Meissner, R. and Theilen, F. (1986) Experimental studies on the absorption of seismic waves. *Absorption of seismic waves*. Burkhardt, H., Paffenholz, J. and Schutt, R. (eds.), *Federal Ministry of Research and Technology Report 03E 2046 A*, Hamburg, 5-56.

Menke, W. (1989) *Geophysical Data Analysis: Discrete Inverse Theory*. Academic Press, San Diego, California.

Michelini, A. and McEvilly, T. V. (1991) Seismological studies at Parkfield: I. Simultaneous inversion for velocity structure and hypocenters using cubic b-splines parameterization. *Bull. Seismol. Soc. Am.* **81**, 524-552.

Mizutani, H. and Kanamori, H. (1964) Variation of elastic wave velocity and attenuation property near the melting temperature, *J. Phys. Earth*, **12**, 43-49.

Moos, D. and Zoback, M. D. (1983) In situ studies of velocity in fractured crystalline rocks. *J. Geophys. Res.* **88**, 2345-2358.

Muffler, L. J. P. (1976) Tectonic and hydrologic controlof the nature and distribution of geothermal resources. *Proc. 2nd UN Symposium on the development and use of geothermal resources*, San Francisco, California.

Murase, T. and McBirney, A. R. (1973) Properties of some common igneous rocks and their melts at high temperatures, *Geol. Soc. Am. Bull.*, **84**, 3563-3592.

Nielson, D. L. (1989) Stress in geothermal systems. *Trans. Geother. Resour. Counc.* **13**, 271-275.

Nielson, D. L., Walters, M. A. and Hulen, J. B. (1991) Fracturing in The Geysers, Sonoma County, California. *Trans. Geother. Resour. Counc.* **15**, 27-33.

Nur, A. and Simmons, G. (1969) The effect of saturation on velocity in low porosity rocks, *Earth Planet. Sci.*, **7**, 183-193.

O'Connell, D. R. and Johnson, L. R. (1991) Progressive inversion for hypocenters and P-wave and S-wave velocity structure: Application to The Geysers, California, geothermal field. *J. Geophys. Res.* **96**, 6223-6236.

O'Connell, R. J., and Budiansky, B. (1974) Seismic velocities in dry and saturated cracked solids, *J. Geophys. Res.*, **79**, 5412-5426.

O'Connell, R. J. and Budiansky, B. (1977) Viscoelastic properties of fluid-saturated cracked solids. *J. Geophys. Res.* **82**, 5719-5735.

Pavlis, G. L. and Booker, J. R. (1980) The mixed discrete-continuous inverse

problem: Application to the simultaneous determination of earthquake hypocenters and velocity structure. *J. Geophys. Res.* **85**, 4801-4810.

Ponko, S. C. and Sanders, C. O. (1994) Inversion for P- and S-wave attenuation structure, Long Valley caldera, California. *J. Geophys. Res.* **99**, 2619-2635.

Press, W. H., Flannery, B. P., Teukolsky, S. A. and Vetterling, W. T. (1989) *Numerical Recipes, the art of scientific computing.* Cambridge University Press, New York, 544-546.

Roecker, S. W. (1982) Velocity structure of the Pamir-HinduKush region: possible evidence of subducted crust, *J. Geophys. Res.*, **87**, 945-959.

Romero, A. E., Gritto, R., Daley, T. and Rector, J. (1995) Analysis of VSP Data from the DOE Exploratory Well (LVF 51-20) at Long Valley Caldera, Eastern California, submitted to *J. Geophys. Res.*

Romero, A. E., Kirkpatrick, A., Majer, E. L. and Peterson, J. E., Jr. (1994) Seismic monitoring at The Geysers geothermal field, *Trans. Geother. Resour. Counc.*, **18**, 331-338.

Romero, A. E., McEvilly, T. V., Majer, E. L. and Michelini, A. (1993) Velocity structure of the Long Valley caldera from the inversion of local earthquake P and S travel times, *J. Geophys. Res.*, **98**, 19,869-19,879.

Romero, A. E., McEvilly, T. V., Majer, E. L. and Vasco, D. (1995) Characterization of the Northwest Geysers geothermal region, California, submitted to *Bull. Seismol. Soc. Am.*

Romero, A. E., McEvilly, T. V. and Majer, E. L. (1995) Three-dimensional P- and S-wave attenuation tomography at the Northwest Geysers California.*Geotherm.*, in press.

Rundle, J. B., Carrigan, C. R., Hardee, H. C. and Luth, W. C. (1986) Deep drilling to the magmatic environment in Long Valley caldera, *Eos Trans. AGU,* **67**, 490-491.

Rybach, L. (1981) Geothermal systems, conductive heat flow, geothermal anomalies. *Geothermal systems: Principles and Case histories*, Rybach, L. and Muffler, L. J. P. (eds.) John Wiley & Sons, Chichester, 3-36.

Sanders, C. O. (1993) Local earthquake tomography: attenuation-theory and results. *Seismic tomography: Theory and practice*, Iyer, H. M. and Hirana, K. (eds.). Chapman & Hall, London, 676-694.

Sanders, C. O. (1984) Location and configuration of magma bodies beneath Long Valley, California, determined from anomalous earthquake signals, *J. Geophys. Res.*, **89**, 8287-8302.

Sato, H., Sacks, I. S. and Murase, T. (1989) The use of laboratory velocity data for estimating temperature and partial melt fraction in the low-velocity zone: Comparison with heat flow and electrical conductivity studies, *J. Geophys. Res.*, **94**, 5705-5715.

Scherbaum, F. (1990) Combined inversion for the three-dimensional Q structure and source parameters using microearthquake spectra. *J. Geophys. Res.* **95**, 12,423-12,438.

Scherbaum, F. and Wyss, M. (1990) Distribution of attenuation in the Kaoiki, Hawaii, source volume estimated by inversion of P-wave spectra. *J. Geophys. Res.* **95**, 12,439-12,448.

Schriener, A., Jr. and Suemnicht, G. A. (1980) Subsurface intrusive rocks at The Geysers geothermal area, California. Proceedings of Symposium Miner Deposition Pacific Northwest, Silberman et al. (eds.), *USGS Open File Report 81-355*, 294-303.

Seagall, P. (1989) Earthquakes triggered by fluid extraction. *Geology*, **17** (10), 942-946.

Sherburn, S. (1984) Seismic monitoring during cold water injection experiment, Wairakei geothermal field-preliminary results. *Proc. 6th New Zealand*

Geothermal Workshop, 129-133.

Solomon, S. C. and Toksoz, M. N. (1970) Lateral variation of attenuation of P- and S-waves beneath the United States. *Bull. Seismol. Soc. Am.* **60**, 819-838.

Sorey, M. L., Suemnicht, G. A., Sturchio, N. C. and Nordquist, G. A. (1991) New evidence on the geothermal system in Long Valley, California, from wells, fluid sampling, electrical geophysics, and age determinations of hot-spring deposits, *J. Volcanol. Geotherm. Res.*, **48**, 229-263.

Spakman, W. and Nolet, G. (1988) Imaging algorithms, accuracy and resolution in delay time tomography, in *Mathematical Geophysics,* edited by N. J. Vlaar, G. Nolet, M. J. R. Wortel, and S. A. Cloetingh, D. Reidel, Norwell, Mass, 155-187.

Spenser, C. and Gubbins, D. (1980) Travel time inversion for simultaneous earthquake location and velocity structure determination in laterally-vaying media, *Geophys. J. Roy. Astron. Soc.*, **63**, 95-116.

Stark, M. A. (1990) Imaging injected water in The Geysers reservoir using microearthquake data. *Trans. Geother. Resour. Counc.* **14**, 1697-1704.

Steck, L. (1992) *Array analysis of 3-component teleseismic P and P coda waves for crustal structure at Long Valley Caldera, California,* Ph.D. Thesis, Dept. of Geol. Sci., Univ. of Calif., Santa Barbara.

Sternfeld, J. N. (1989) Lithologic influences on fracture permeability and the distribution of steam in the Northwest Geysers steam field, Sonoma County, California. *Trans. Geother. Resour. Counc.* **13**, 473-479.

Stewart, R. and Peselnick, L. (1977) Velocity of compressional waves in dry Franciscan rocks to 8 kbar and 300°C. *J. Geophys. Res.* **82**, 2027-2039.

Stewart, R. and Peselnick, L. (1978) Systematic behavior of compressional velocity in Franciscan rocks at high pressure and temperature. *J. Geophys. Res.* **83**, 831-839.

Suemnicht, G. A. (1987) Results of deep drilling in the western moat of Long Valley, California, *Eos Trans. AGU,* **68**, 785.

Taylor, S. R., Bonner, B. P. and Zandt, G. (1986) Attenuation and scattering of broad-band P- and S-waves across North America, *J. Geophys. Res.* **91**, 7309-7325.

Thomas, R. P. (1981) Subsurface geology, A reservoir assessment of The Geysers geothermal field. *Calif. Div. Oil Gas Pub. No. TR 37.*

Thompson, R. C. (1992) Structural stratigraphy and intrusive rocks at The Geysers geothermal field. *Geother. Res. Council Special Report No. 17,* 59-63.

Thurber, C. H. (1983) Earthquake locations and three- dimensional crustal structure in the Coyote Lake area, Central California. *J. Geophys. Res.* **88**, 8226-8236.

Toksöz, M. N., Cheng, C. H. and Timur, A. (1976) Velocities of seismic waves in porous rocks, *Geophysics.* **41**, 621-645.

Toomey, D. R., and Foulger, G. R. (1989) Tomographic inversion of local earthquake data from the Hengill-Grensdalur Central Volcano Complex, Iceland, *J. Geophys. Res.,* **94**, 17,497-17,510.

Truesdell, A., Walters, M. A., Kennedy, M. and Lippmann, M. (1993) An integrated model for the origin of The Geysers geothermal field. *Trans. Geother. Resour. Counc.* **17**, 273-280.

Um, J. and Thurber, C. H. (1987) A fast algorithm for two-point seismic ray tracing. *Bull. Seismol. Soc. Am.* **77**, 972-986.

Walck, M. C. (1988) Three-dimensional Vp/Vs variations for the Cosos region, California. *J. Geophys. Res.* **93**, 2047-2052.

Wallace, R. H., Kraemer, T. F., Taylor, R. E., and Wesselman, J. B. (1979)

Assessment of geopressured-geothermal resources in the northern Gulf of Mexico basin. *Assessment of geothermal resources of the United States-1978*, Muffler, L. P. J. (ed.) *USGS Circular 790,* 132-155.

Walters, M. A. and Combs, J. (1992) Heat flow in The Geysers-Clear Lake geothermal area of northern California. *Geother. Res. Council Special Report No. 17*, 43-53.

Walters, M. A., Sternfeld, J. N., Haizlip, J. R., Drenick, A. F. and Combs, J. (1988) A vapor-dominated reservoir exceeding 600°F at The Geysers, Sonoma County, California. *Proc. 13th Workshop on Geothermal Reservoir Engineering*, *Tech. Rep. SGP-TR-113*, Stanford University, California, 73-81.

Wannamaker, P. E., Wright, P. M., Zhou, Z., Li, X. and Zhao, J. (1991) Magnetotelluric transect of Long valley caldera: Resistivity cross-section, structural implications, and the limits of a 2-D analysis, *Geophysics,* **56**, 926-940.

White, D. E. (1967) Some Principles of geyser activity mainly from Steamboat Springs, Nevada. *Am. J. Science,* **265,** 641-684.

White, J. E. (1975) Computed seismic speeds and attenuation in rocks with partial gas saturation, *Geophysics,* **66**, 75-97.

Williams, C. F., Galanis, S. P., Moses, T. H. and Grubb, F. V. (1993) Heat flow studies in the Northwest Geysers geothermal field, California. *Trans. Geother. Resour. Counc.* **17**, 281-288.

Winkler, K. and Nur, A. (1979) Pore fluids and seismic attenuation in rocks. *Geophys. Res. Lett.*, **6**, 1-4.

Zoback, M. D., Zoback, M. L., Mount, V. S., Suppe, J., Eaton, J. P., Healy, J. H., Oppenheimer, D. H., Reasenberg, P. A., Jones, L. M., Raleigh, C. B., Wong, I. G., Scotti, O. and Wentworth, C. M. (1987) New evidence on the state of stress of the San Andreas fault system. *Science*, **238**, 1105-1111.

Zucca, J. J., Hutchings, L. J. and Kasameyer, P. W. (1994) Seismic velocity and attenuation structure of The Geysers geothermal field, California. *Geothermics*, **23**, 111-126.

Zucca, J. J., Kasameyer, P. W. and Mills, J. M., Jr. (1987) Observation of a reflection from the base of a magma chamber in Long Valley Caldera, California, *Bull. Seismol. Soc. Am.*, **77**, 1674-1687.